Interstellar dust
in dwarf galaxies

Israel Rodríguez Hermelo

Departamento de Física Teórica y del Cosmos

Universidad de Granada

Programa Oficial de Posgrado en Física y Matemáticas

November 2012

Editor: Editorial de la Universidad de Granada
Autor: Israel Rodríguez Hermelo
D.L.: GR 871-2013
ISBN: 978-84-9028-463-6

Summary

Instead of being a passive ”observer”, interstellar dust plays a vital role in the evolution of galaxies. Due to its high opacity for the UV/optical photons, interstellar dust is effective in attenuating, via absorption and scattering, the UV/optical SED of galaxies. Besides, interstellar dust provides ~30% of the total Galactic luminosity via their IR emission. In this thesis we have studied the interstellar dust of dwarf starbursting galaxies from both the perspectives of the extinction and the self-emission.

We have chose these kind of objects because we are interested in understanding how the dust behaves in environments that are very strongly influenced by intense star formation processes and by the action of stellar winds coming from the massive stars. Starbursting dwarf galaxies exhibiting holes and shells are ideal objects to study this as, in general, they have an small number of star forming regions dominating the emission. Therefore, a clear separation between the emission coming from the star-forming regions and the diffuse disk can be performed.

In the first part of this thesis we studied the dust extinction in the dwarf starbursting galaxy NGC 4214. The UV/optical emission of NGC 4214 is dominated by two star forming complexes located at its centre. These regions where mapped with the HST-WFC3 covering a broad range of the spectrum, from the near ultraviolet to the near infrared, including three different Hydrogen recombination lines.

We made use of the Hβ, Hα and Pβ Hydrogen recombination lines to compute the extinction in the central star forming complexes of NGC 4214. Our aim was to obtain a high resolution picture of the distribution of the dust extinction associated with these complexes and to compare it to the distribution of the dust emission. Furthermore, the extinction maps allowed us to derived extinction-corrected maps of the ionized line emission maps. The extinction was calculated assuming a foreground dust screen model. We tested two different extinctions laws described by the values of $R_V = 3.10$ and 5.45. The extinction law of $R_V = 3.10$, which is widely used in the literature, describes the dust properties

found in the diffuse ISM, whereas the extinction law of $R_V = 5.45$ is more appropriated for dust in molecular clouds. The choice of $R_V = 5.45$ was based on the results found by Úbeda et al. (2007).

Three extinction maps for each value of R_V were derived based on the $P\beta/H\alpha$, $P\beta/H\beta$, and $H\alpha/H\beta$ line ratios. If the assumed geometry (foreground screen) and the dust properties ($R_V = 3.10$ or $R_V = 5.45$) are correct, then all three line ratios should give exactly the same result. Deviations from this situation allow us to draw conclusions about the real dust geometry and properties. In general, the different extinction maps show very similar structures of the dust extinction which furthermore agree qualitatively with those of the dust emission at 8 μm which is the only dust emission map with a comparable spatial resolution. However, the exact value of the extinction at a position is different depending on the line-ratio considered.

In order to quantitatively compare the extinction maps obtained with different line-ratios, we compared these maps on a pixel-to-pixel basis. Our study was restricted to those regions where the photo-ionisation is the dominant process in the ionisation of the gas. We found good correlations between the different extinction maps, but this correlation was not always linear and in some cases had a large scatter. Specifically, we found that the photo-ionised regions where we measured the highest values of the extinction present clear deviations from the linearity. In general, the extinction maps derived with the line-ratio $P\beta/H\alpha$ present higher values than the maps derived with $P\beta/H\beta$, and latter show higher values than the map derived with $H\alpha/H\beta$. These trends are less pronounced but still present for the extinction law of $R_V = 5.45$.

We interpret the fact that the values of the extinction derived from different lines agree better for $R_V = 5.45$ as an indication that this values is more appropriate for the dust properties in NGC 4214. We discussed different geometrical scenarios that could explain our findings. The fact that the extinction derived from $P\beta/H\beta$ is lower than the extinction from $P\beta/H\alpha$ for several regions can be understood if scattering has an important effect in bringing back photons to our line of sight. Scattering is more important for the shorter-wavelength $H\beta$-line than for $H\alpha$ and thus produces a lower value for $P\beta/H\beta$ than for $P\beta/H\alpha$. Scattering is becoming relevant if the dust is close to the emitting gas. A simple mixing of dust and gas is not sufficient to reproduce the high values of the extinction found in the star forming regions of NGC 4214. Finally, the fact that the extinction derived from $H\alpha/H\beta$ is lower than the extinction from $P\beta/H\alpha$ is an indication for a clumpy distribution of the dust. All these indications lead to a final picture in which the dust causing the extinction is mainly distributed in a dense, clumpy structure close to the emitting region, which physically would correspond to dust within a fragmented PDR.

In the second part of this thesis we analysed the interstellar dust of NGC 4214 and NGC 4449 from the perspective of its re-emission at infrared and submillimetre wavelengths. The goals were to test whether models with Galactic dust properties could describe the dust SED of these dwarf galaxies, to test the relevance of the geometrical distribution of dust and stars on the dust SED and to carry out a detailed energy balance of the dust heating and emission in a realistic geometry.

Due to their proximity we were able to derive the dust SED separately for the emission from the major massive star forming regions and for the diffuse dust. For the first time this analysis was done from the perspective of a self-consistent radiation transfer calculation constrained by the observed SEDs of spatially separated components on resolved maps. In making predictions for the UV/optical-FIR/submm SEDs of these components this analysis quantitatively takes into account the level and colour of UV/optical radiation fields incident on both pc-sized dusty structures in the star forming complexes and on dust grains distributed on kpc scales in the diffuse ISM, illuminated by a combination of UV light escaping from the SF regions and the ambient optical radiation fields, as constrained by UV/optical photometry of the galaxy.

The overall analysis was done using the Popescu et al. (2011) model based on full radiative transfer calculations of the propagation of starlight in disk galaxies adopting a realistic geometry for the distribution of stars and dust. For the description of the dust emission from HII region and their associated PDRs we used the model of Groves et al. (2008). This model describes the luminosity evolution of a star cluster of mass $M_{\rm cl}$, and incorporates the expansion of the HII regions and PDRs due to the mechanical energy input of stars and SNe. The dust emission from the HII region and the surrounding PDR is calculated from radiation transfer.

The large amount of ancillary data and results from previous studies allowed us to constrain a major part of the input parameters of the models. We achieved a good agreement between data and models, both for the diffuse dust emission and the dust in HII+PDR regions for both galaxies. We achieved satisfactory fits for the star forming regions with the exception of the IRAC 8 μm data points. Possible reasons for this discrepancy are that the model assumptions (PAH abundance and destruction) are not completely adequate for the case of NGC 4214 and NGC 4449 or that these galaxies have an unusually high emission at 8 μm for their metallicities and radiation field, which in the case of NGC 4214 is supported by other studies (Engelbracht et al. 2008).

For both galaxies, we could fit the diffuse dust SED satisfactorily, and we derived global gas-to-dust mass ratios compatible with their expected values from their metallicities. However, we inferred that the UV emission was severely (by a factor of 2-4) underpredicted with respect to the observed, deattenuated diffuse UV flux. We discussed different explanations for this discrepancy (escape of UV emission, geometrical effects, a very extended dust disk and different dust properties). The most plausible one is that a large fraction of the UV radiation that escapes from HII+PDR regions leaves the galaxy unattenuated and is thus not participating in the heating of the diffuse dust, most likely due to a porous ISM.

Resumen

En lugar de ser un observador pasivo, el polvo interestelar juega un papel vital en la evolución de las galaxias. Debido a su alta opacidad para los fotones ultravioletas y ópticos, el polvo interestelar atenúa el campo de radiación ultravioelta y óptico de las galaxias, a través de procesos de absorción y scattering. Además, el polvo interestelar es responsable del $\sim$30% de la emisión total de las galaxias debido a su propia emisión a longitudes de onda infrarojas. En esta tesis hemos estudiado el polvo interestelar de galaxias enanas con brotes de formación estelar tanto desde la perspectiva de la extinción como de la emisión

Hemos elegido este tipo de objetos porque estamos interesados en entender como se comporta el polvo en entornos fuertemente influenciados por intensos brotes de formación estelar y por la acción de vientos estelares provenientes de las estrellas masivas. Las galaxias enanas con brotes de formación estelar son objetos ideales para nuestro estudio debido a que, en general, poseen un pequeño número de regiones de formación estelar dominando su emisión. Así pues es posible separar la emisión originada en dichas regiones de formación estelar de la emisión originada en el disco de polvo difuso.

En la primera parte de esta tesis estudiamos la extinctión del polvo en la galaxia enana NGC 4214. La emisión ultravioleta y óptica de NGC 4214 está dominada por dos complejos de formación estelar localizados en su centro. stas regiones fueron observadas con el HST-WFC3 cubriendo un ancho rango espectral, desde el ultravioleta cercano hasta el infrarojo cercano, incluyendo tres líneas de recombinación del Hidrógeno.

En concreto, para calcular la extinción en dichas regiones hemos usado las líneas de recombinación Hβ, Hα y Pβ. Nuestro objetivo es obtener un mapa de alta resolución de la distribución de la extinción debida al polvo asociado con estos complejos, asi como comparar dicha extinción con la emisión debida al polvo. Además, los mapas de extinción nos permiten obtener mapas corregidos de las líneas de emisión. La extinción fue calculada asumiendo que el polvo se distribuye en una pantalla uniforme situada entre el gas y nosotros. Hemos probado dos leyes de extinción diferentes caracterizadas por valores R_V = 3.10 and 5.45.

El primer valor, ampliamente utilizado en la literatura, describe bien las propiedades del polvo que se encuentra en la componente difusa del medio interestelar; mientras que el segundo valor es más apropiado para el polvo asociado con nubes moleculares. La elección de $R_V = 5.45$ está basada en los resultados de Úbeda et al. (2007).

Tres mapas de extinción para cada valor de R_V fueron calculados en base a los cocientes $P\beta/H\alpha$, $P\beta/H\beta$ y $H\alpha/H\beta$. Si la geometría y las propiedades que hemos asumido para el polvo son correctas, entonces de los tres mapas se deberían obtener los mismos valores para la extinción. Desviaciones de este comportamiento nos permiten obtener conclusiones sobre la geometría y las propiedades reales del polvo en NGC 4214.En general, los tres mapas de extinción muestran estructuras similares de la extinción y además, dichas estructuras, coinciden con la estructura que muestra el mapa de emisión a 8 μm, el cual es el único mapa de emisión del polvo que tiene una resolución comparable. Sin embargo, el valor exacto de la extinción en cada punto es diferente dependiendo del cociente utilizado.

A fin de realizar una comparación cuantitativa de los diferentes mapas obtenidos con diferentes cocientes, hemos comparado dichos mapas en una base píxel a píxel. Nuestro estudio se restringe a aquellas regiones donde la fotoionización es el proceso dominante en la ionización del gas. Hemos encontrado una buena correlación entre los diferentes mapas, pero esta correlación no es siempre lineal y en algunos casos muestra mucha dispersión. En concreto, hemos hallado que las regiones fotoionizadas que presentan altos valores de la extinción, son las que muestran claras desviaciones de la linealidad. En general, los mapas de extinción derivados con el cociente $P\beta/H\alpha$ presentan valores más altos que los mapas derivados $P\beta/H\beta$, y éste último presenta valores mayores que el mapa derivado con $H\alpha/H\beta$. Estas tendencias son menos pronunciadas, aunque todavía existen, para el caso de la ley de extinción de $R_V = 5.45$.

Interpretamos el hecho de que los valores de la extinción derivados con diferentes lineas presentan un mejor acuerdo para $R_V = 5.45$ como una indicación de que este valor es más apropiado para las propiedas del polvo de NGC 4214. Discutimos diferentes escenarios geométricos que pueden explicar nuestros hallazgos. El hecho de que en algunas de las regiones la extinción derivada con $P\beta/H\beta$ es más baja que la derivada con $P\beta/H\alpha$ puede ser debido a que el scattering tiene un efecto importante en desviar fotones hacia nuestra linea de visión. El scattering es más importante para longitudes de onda cortas, como $H\beta$, que para fotones de longitudes de onda más largas como $H\alpha$, y por ello produce un valor más bajo para Pβ/Hβ que para Pβ/Hα. El scattering se vuelve importante si el polvo está cerca del gas ionizado. Un modelo simple de gas y polvo mezclados no es capaz de explicar las altas extinciones medidas en NGC 4214. El hecho de que la extinción derivada de Hα/Hβ sea menor que la derivada de Pβ/Hα indica que la distribución de polvo ha de ser grumosa. Todas estas indicaciones nos llevan a la conclusión de que el polvo que causa la extinción está distribuido en una densa y grumosa estructura cercana al gas ionizado, lo cual fisicamente se correspondería con polvo presente en una región de fotodisociación fragmentada.

En la segunda parte de esta tesis hemos analizado el polvo interestelar de NGC 4214 y NGC 4449 desde la perspectiva de su re-emisión a longitudes de onda infrarojas y sub-milimétricas. Nuestros objetivos son comprobar si los modelos de polvo con propiedades Galácticas pueden describir la emisión del polvo en galaxias enanas; comprobar la importancia de la distribución geométrica del polvo y las estrellas en dichas galaxias; y por último, llevar a cabo un estudio detallado del balance energético del calentamiento y la emisión del polvo en una geometría realista.

Debido a su proximidad hemos podido estudiar por separado la emisión proveniente de las principales regiones de formación estelar y la emisión del polvo difuso. Por primera vez para galaxias enanas este análisis se ha llevado a cabo teniendo en cuenta la ecuación de transporte radiativo. Nuestro análisis tiene en cuenta la intensidad y el color de la radiación ultravioleta y óptica que incide tanto sobre los complejos de formación estelar como sobre el polvo distribuido en el medio interestelar difuso, el cual es una combinación de luz ultravioleta que escapa de las regiones de formación estelar y del campo de radiación difuso que determinamos a través de fotometría ultravioleta y óptica en nuestras galaxias.

El análisis ha sido realizado utilizando el modelo de Popescu et al. (2011), el cual aplica la ecuación de transporte radiativo a la luz que se propaga a través del disco galáctico a una distribución geométrica realista de estrellas y polvo. Para el estudio de la regiones HII y sus PDRs hemos usado el modelo de Groves et al. (2008). Este modelo describe la evolución de la luminosidad de un cúmulo estelar de masa $M_{\rm cl}$, e incorpora la expansión de la región HII y de la región de fotodisociación debido a la energía mecánica inyectada por las estrellas y las explosiones de supernovas. La emisión del polvo de la región HII y de la región de fotodisociación es calculada en base a la ecuación de transporte radiativo.

La gran cantidad de observaciones disponibles así como los resultados obtenidos en estudios anteriores nos permiten restringir gran parte de los parámetros de entrada de los modelos. En las dos galaxias encontramos un buen acuerdo entre observaciones y modelos, tanto para el polvo difuso como para las regiones de formación estelar, con la unica excepción de las observaciones con IRAC 8 μm. Posibles razones de esta discrepancia pueden ser que o bien las propiedades de los hidrocarburos policíclicos aromáticos (responsables de la emisión a 8 μm) asumidas por los modelos no son apropiadas para el caso de NGC 4214 y NGC 4449, o bien que estas galaxias poseen una emisión inusual a 8 μm, lo cual en el caso de NGC 4214 estaría apoyado por otros estudios (Engelbracht et al. 2008).

Para ambas galaxias hemos podido ajustar la emisión del polvo disfuso satisfactoriamente y hemos derivado una relación entre la masa del gas y la masa del polvo compatible con lo que esperaríamos en función de sus metalicidades. Sin embargo, inferimos que la emisión ultravioleta y óptica de las estrellas está severamente subestimada con respecto a las observaciones. Hemos discutido diferentes explicaciones para esta discrepancia (escape de radiación ultravioleta, efectos geométricos, un disco de polvo muy extendido y diferentes propiedades de polvo). La más probable es que una gran fracción de la radiación ultravioleta abandona la galaxia sin participar en el calentamiento del polvo, probablemente debido a la porosidad del medio interestelar

Contents

CHAPTER 1

The Interstellar Medium

> *"Surely, there is a hole in the heavens!"*
>
> – Sir William Herschel (1785)

Looking at the sky in a dark night, the Milky Way shows dark lanes (see Figure 1.1). In some parts, these lanes are so deeply obscured that no star is visible. The absence of stars in these regions was first pointed out in the year 1785 by Sir William Herschel, who considered them as "holes in the heavens", produced by gravitational fragmentation of our galaxy.

We know now that Herschel was wrong, the absence of stars is only apparent. Stars are there, but they are hidden behind interstellar dust, which has the property to extinct the stellar light. In the Milky Way, and in any galaxy, the space between stars is not empty. Besides the electromagnetic radiation and the cosmic rays emitted by the stars, the interstellar space is filled with matter in both gaseous (interstellar gas) and solid (interstellar dust) states.

In galaxies similar to ours, the interstellar matter, generally known as Interstellar Medium (ISM), only represents the 15% of the total mass of visible matter. From this 15%, the 99% of the ISM is formed by interstellar gas, leaving only the remaining 1% as solid matter.

In the present work we try to understand how the 1% of the 15% of the mass of visible matter of galaxies behaves. Despite the small fraction of the mass that it represents, as we will see throughout this work, interstellar dust is essential to understand the global emission from galaxies.

Figure 1.1: Long exposure photograph of the Milky Way (Castle Valley, Utah)

1.1 Components of the ISM

The ISM of all galaxies is full of electromagnetic radiation, known as interstellar radiation field (ISFR), which includes the photons emitted by the stars and the photons produced by secondary processes in the ISM itself[1]. The physical properties of the ISM are in part determined by this ISRF.

In a typical gas cloud with the same chemical composition as the Sun, 70% of its mass is in form of hydrogen, the 28% is in form of Helium, and the remaining 2% is in form of heavier elements or ”metals”. Depending mainly on the intensity and the spectrum of the ISFR, the interstellar gas can exist in ionized, neutral or molecular state. Due to the fact that hydrogen

---

[1] Strictly speaking, the ISFR also includes an extragalactic component consisting of radiation coming from other galaxies and of the cosmic background blackbody radiation at 2.7 K (Lequeux 2005). However, at the wavelength of the the cosmic background photons (~0.3-300 mm) the ISM is very transparent, and therefore, the impact of these photons on the ISM is very limited. Regarding to the radiation field coming from other galaxies, since this is frequently much fainter than the galactic radiation field, it can be neglected in most of the extent of the galaxy. The only exceptions are the more external parts of the galaxy, as the halo or the border of the disk, where the galactic and the extragalactic radiation field begin to merge. In the present work, we will refer to the ISFR as the radiation field emitted within the galaxies and we will neglect the extragalactic radiation field, which is out of the scope of our study.

is the most abundant element, the division between ionised, neutral and molecular phases of the ISM is based on the predominant state of this particular element[1].

The ISM is made up of a number of components, which can be described by their hydrogen gas densities, their temperatures, and their state of ionisation (Hollenbach and Tielens 1999).

In the regions where the hydrogen has been photoionised by ultraviolet (UV) photons from hot stars, frequently referred to as **HII regions**, the gas is heated by photoelectrons up to temperatures of about 10 000 K. These regions have sizes of a few pc and their lifetimes are essentially those of the ionizing stars (3-10 Myr). Besides the constant input of energy from the photons, stars are also a source of mechanical energy through particles ejected in stellar winds and, occasionally, in supernova (SN) explosions. This injection of mechanical energy into the surrounding gas produces the expansion of the HII region. These regions present a wide variety of densities, with values that range from 0.3 to 10^4 cm^{-3}.

The part of the ISM where the neutral hydrogen (HI) is the dominant species shows a wide range of temperatures and densities, from T $\approx$ 5 000 K and n $\approx$ 0.6 cm^{-3} typical of the **warm neutral medium**, to T $\approx$ 100 K and n $\approx$ 30 cm^{-3} found in the **cold neutral medium**.

When the density of a gas cloud is large enough to effectively shield its interior parts of the ISFR, hydrogen atoms are able to form molecules. These **molecular clouds**, with densities ranging from 10^3 to 10^6 cm^{-3} and temperatures lower than 50 K, are frequently self-gravitating. It is in this phase of the ISM where the star forming processes take place.

We should note that the boundaries between the different components of the ISM are not well defined. A good example of this fact are the star forming regions. In these regions, once the new stars are born, the surrounding gas is rapidly ionised in the vicinity of the stars. On the other hand, the interior of the densest parts of the parental molecular cloud remain shielded from the energetic photons emitted by the young stars, and therefore, the hydrogen remains in molecular state. By contrast, the most external parts of the molecular clouds are effectively penetrated by the non ionising UV radiation from the stars, leading to the photo-dissociation of the H_2, and thereby creating a interphase of HI between the HII and the H_2. These interphases, where the heating is dominated by non ionising UV photons, are known as **photo-dissociation regions** (PDRs).

---

[1] It is important to note that different elements have different ionization potentials and therefore, in the same ISFR, it is possible to find these elements in different states than the hydrogen. For example, the ionization potential of Helium is E_0^{HeI} = 24.59 eV, almost twice than that of the hydrogen (E_0^{HI} = 13.6 eV). For this reason, it is possible to find neutral Helium in regions where the hydrogen is ionized but the opposite it is not true.

Figure 1.2: Image of the spiral galaxy NGC 2403 from a composition of space and ground-based image data from the Hubble Legacy Archive and the 8.2 m Subaru Telescope at the summit of Mauna Kea (Hawaii). In the composition, the HII regions are marked by the reddish glow of atomic hydrogen gas. Credits: Robert Gendler.

1.2 Photo-ionisation of HII regions

The presence of ionized gas clouds in the Milky Way was first recognized through photographic surveys in regions near hot stars. Only the B and O stars [1], produce photons with wavelengths $\leq 912\,\text{Å}$ capable to ionize the hydrogen. For these reason, although the hydrogen also can be ionized through other processes such collisions with cosmic rays and shocks, the ionized gas in galaxies is predominantly associated with regions of formation of new stars. The gas clouds ionized by O and B stars are known as HII regions (see Fig. 1.2).

The HII regions are characterized by high temperatures ($T \sim 10^4$ K) and relatively low densities ($N \sim 100\,\text{cm}^{-3}$). Since the hydrogen is in an ionized state, HII regions are strong emitters of electromagnetic radiation due to the continuous interaction between charged particles.

Absorption of photons, recombination between ions and free electrons, and collision with

---

[1] B and O type stars are extremely luminous and they live only about 10 Myr on the Main Sequence. B type stars have from 2 to 16 times the mass of the Sun and surface temperatures between 10^4 and 3×10^4 K. O type stars have between 15 and 90 times the mass of the Sun and surface temperatures between 3×10^4 and 5×10^4 K.

other particles are the different processes that can excite an atom and afterwards lead to a radiative cascade of emission-line photons. In this Section, we give a simplified description of these processes that are responsible for the line-emission spectrum of HII regions.

An HII region can be approximated as an ionized sphere surrounding a hot star or a cluster of hot stars. The recombination between free electrons and ionized atoms, and the subsequent electron cascades from the various excited states is one of the main mechanism of emission in the HII regions. The ionization equilibrium at each point in the nebula is determined by the balance between the number of photo-ionizations and recombinations of free electrons with the ions.

We outline in the following the calculation of hydrogen emission lines in HII region based on the detailed description in *"Astrophysics of Gaseous Nebulae and Active Galactic Nuclei"* (Osterbrock 1989). In the simplified case of an HII region formed only by hydrogen, the ionisation equilibrium equation can be written as:

$$N_{\rm HI} \times \int_{\nu_0}^{\infty} \frac{4\,\pi\,J_\nu}{h\,\nu}\, a_{\rm HI}(\nu)\, d\nu = N_e \times N_p \times \alpha_{\rm HI}(T) \qquad (1.1)$$

At the left side of the equation, the number of ionisations is fixed by the the number of atoms in neutral state that can be ionised, $\mathrm{N_{HI}}$, the intensity of the radiation field, J_ν, and the ionisation cross section of the HI, $a_{\rm HI}(\nu)$. Note that the integral is only defined for frequencies above the ionisation threshold $\nu_0 = \mathrm{E_0/h}$. At the right side, the number of recombinations is determined by the number of free electrons and hydrogen ions, Ne and Np, respectively, and by the recombination coefficient, $\alpha_{\rm HI}$(T). This equation can be written in terms of the total (neutral plus ionized) number of hydrogen atoms, $\mathrm{N_H}$, and the fraction of ionization, ξ, as:

$$\int_{\nu_0}^{\infty} \frac{4\,\pi\,J_\nu}{h\,\nu}\, a_{\rm HI}(\nu)\, d\nu = \frac{(1-\xi)^2}{\xi} \times N_{\rm H} \times \alpha_{\rm HI}(T) \qquad (1.2)$$

where we made use of the definitions $\mathrm{N_{HI}} \equiv \xi \times \mathrm{N_H}$, $\mathrm{N_p} \equiv (1-\xi) \times \mathrm{N_H}$ and $\mathrm{N_e} \equiv (1-\xi) \times \mathrm{N_H}$. Due to the low density of the HII regions, after the photo-ionization the electron can travel freely during a long time (of the order of 10^5 yr) without being recombined with an ion. When the electron is finally captured, the newly formed atom can be in an excited level of energy and therefore, the electron will cascade into lower levels of energy until the ground level is reached. In each transition during the cascade, the atom will emit a photon with an energy equal to the energy gap between the two levels (see Fig. 1.3). The mean lifetime of the excited levels are of the order to 10^{-4} to 10^{-8} s, and thus, after recombination, the excited atom will return quickly to the ground state, where it will stay without being photo-ionized during a period of the order from hours to months. Therefore, at the end of the cycle, the electron spends most of the time travelling freely.

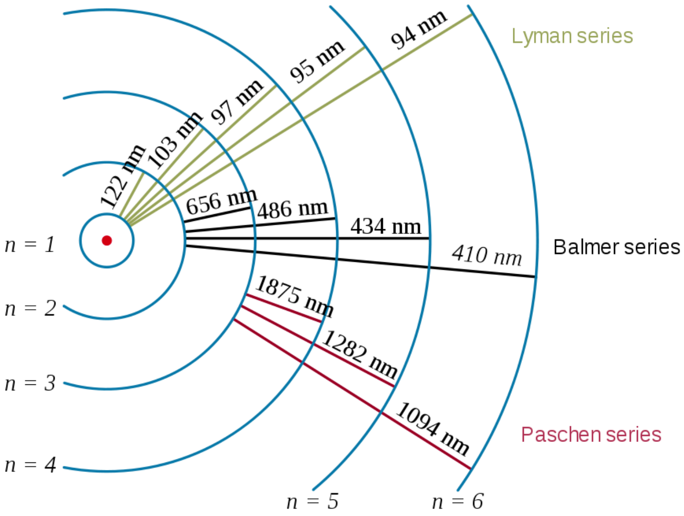

Figure 1.3: Electron transitions and their resulting wavelengths for the hydrogen atom. The probabilities of the transitions are listed in Table 1.1.

The recombination line-spectrum of the hydrogen can be calculated. In the lower density limit, the total number of atoms in a certain level nL will be determined by the number of electrons that are directly recombined to the level nL, the number of electrons that drop in the level nL from higher levels n″L″, and the number of electrons that fall from nL into lower levels n′L′. Thus, the equation of statistical equilibrium for any level nL can be written as:

$$N_p\,N_e\,\alpha_{nL}(T) + \sum_{n'>n}^{\infty}\sum_{L'} N_{n'L'} \times A^{nL}_{n'L'} = N_{nL} \times \sum_{n''=1}^{n-1}\sum_{L''} A^{n''L''}_{nL} \qquad (1.3)$$

The probability of the transition from the level nL to a lower level n′L′, $\mathrm{A}^{\mathrm{nL}}_{\mathrm{n'L'}}$, as well as the probability of the transitions between n″L″ to the level nL, $\mathrm{A}^{\mathrm{n''L''}}_{\mathrm{nL}}$, can be calculated by solving the Schrodinger equation. Besides, in conditions of thermodynamic equilibrium the population, the population of the level of quantum numbers nL, N_{nL}, can be calculated as:

$$N_{nL} = (2L+1)\left(\frac{2\,\pi\,m\,k\,T}{h^2}\right)^{3/2} e^{h\,\nu_0/n^2\,k\,T}\,N_p\,N_e \qquad (1.4)$$

From Equations 1.3 and 1.4 it is possible to calculate the emission coefficient, $\mathrm{j}_{\mathrm{nn'}}$, as:

$$j_{nn'} = \frac{h(\nu - \nu')}{4\pi} \sum_{L=0}^{n-1} \sum_{L'=L\pm1} N_{nL} \times A_{n'L'}^{nL} \tag{1.5}$$

To reduce the complexity of the problem, the recombination-line theory frequently makes use of one of these two approximations:

Case A: In this case it is assumed that the gas is optically thin and therefore, that all the photons emitted by excited atoms can escape from the HII regions without further interactions with other atoms.

Case B: In this case it is assumed that the gas is optically thick for the Lyman-line photons and therefore, that Lyman-line photons are not able to escape from the nebula but they are immediately absorbed nearby in the nebula. In this case, where we can omit all the transitions to the ground level, and thus the sum in Equation 1.3 ends in $n'' = 2$.

Case A is only a good approximation for HII regions of such low density that make them too faint and difficult to observe, and therefore, for most observable nebulae, Case B is more accurate than Case A. In Tab. 1.1 the values of the emission coefficients under Case B conditions for the main recombination lines are shown.

Transition	$n \rightarrow n'$	λ (nm)	$j_{nn'}$
Hδ	$6 \rightarrow 2$	410.18	0.259
Hγ	$5 \rightarrow 2$	434.05	0.468
Hβ	$4 \rightarrow 2$	486.14	1.000
Hα	$3 \rightarrow 2$	656.28	2.859
Pβ	$2 \rightarrow 3$	1281.8	0.163
Pα	$1 \rightarrow 3$	1875.1	0.338

Table 1.1: Transition probabilities of the main recombination lines of the hydrogen atom. The values, which are normalized to the probability of the Hβ transition, correspond to *Case B* conditions and to the typical values of photo-ionised regions $T = 10^4$ K and $N_e = 100\,\mathrm{cm}^{-3}$.

1.3 Interstellar dust

As in the Milky Way, in most galaxies clear patterns of dust extinction are observed in their stellar images directly by visual inspection. Knowing the optical properties of the dust and its spatial distribution with respect to the other components of the ISM and the stars is essential to understand the dust extinction and its re-emission at infrared and submillimetre wavelengths, and therefore, to understand the energetic balance of galaxies, the evolution of the ISM and the star forming process.

However, many aspects of the nature of interstellar dust remain unclear. Dust grains are condensed in the cool atmospheres of evolved stars and they present a wide variety of complex molecules of different shapes and compositions with sizes ranging from nanometres to micrometres. Our knowledge of the composition of interstellar grains is based mainly on their spectroscopic absorption/emission features and observed elemental depletions. The most generally accepted view is that interstellar grains consist of amorphous silicates and some form of carbonaceous materials (Li and Draine 2001).

In the following Sections 1.3.1 and 1.3.2 a brief description of the dust extinction and emission is given.

1.3.1 Dust extinction

In discussing the effects of dust in galaxies, it is important to distinguish between the *attenuation curve* of the galaxy and the *extinction curve* of the dust in that galaxy. The extinction curve of the dust is uniquely related to the physical properties of the dust, whereas the attenuation is the decrease in the luminosity of the stellar light when seen through a dust cloud and it depends in both the spatial distribution of the dust within the galaxy and on the extinction curve of the dust.

The extinction curve of the dust grains depends on how they scatter and absorb the photons. The *extinction efficiency* of a dust grain, $\mathrm{Q_e}$, is the sum of its *absorption efficiency*, $\mathrm{Q_a}$, and its *scattering efficiency*, $\mathrm{Q_s}$. The albedo of a dust grain is defined as the ratio $\mathrm{Q_s/Q_e}$. Apart from the albedo, the dust extinction also depends on the phase function, which correspond to the average cosine of the angle of scattering. Both the albedo, ω_λ, and the phase function, g_λ, are wavelength dependent.

Lillie and Witt (1976) used the observations of the diffuse Galactic light with the Orbiting Astronomical Observatory (OAO-2) to determine ω_λ and g_λ of the dust grains in the spectral range from 150 nm to 420 nm. Morgan et al. (1976) derived ω_λ at 235 nm and 274 nm by fitting a theoretical model to the observations of the diffuse Galactic background light obtained by the TD-I satellite. Mathis (1983) quotes the values of ω_λ and g_λ in a wide spectral range from 300 nm to 1800 nm from a theoretical model of uncoated graphite and silicate particles. Chlewicki and Mayo Greenberg (1984) derive values of ω_λ and g_λ for interstellar grains in the UV based on observations of the extinction.

The results found by these authors show that the albedo has a minimum $\sim$ 220 nm, which indicates that at this wavelength absorption is the main cause of extinction. From this minimum the albedo increases until it reaches in the vicinity of the B-band and then, it decreases towards longer wavelengths. The phase function, g_λ has its maximum at $\sim$ 200 nm. The value at the maximum is close to unity, which indicates that scattering at these wavelengths is mainly forward-directed, and it decreases towards longer wavelengths until reach values close to 0, which would correspond to isotropic scattering (see Figure 1.4).

The wavelength dependence of the albedo produces that the photons with wavelengths in the vicinity of the B band are more effectively scattered than photons of larger wavelengths.

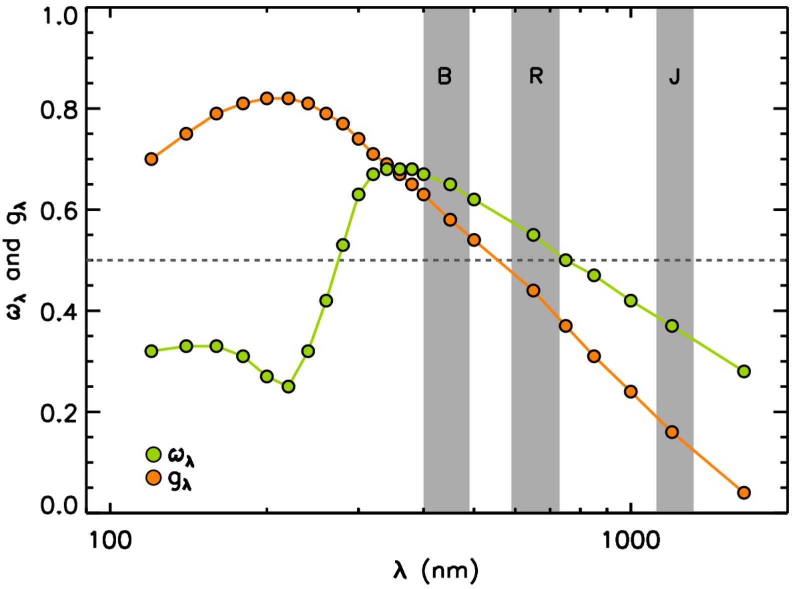

Figure 1.4: Albedo (green-filled circles) and phase function (orange-filled circles) of the dust grains as a function of wavelength. The values plotted correspond to the work of Bruzual A. et al. (1988), who fitted smooth curves to the values derived by Lillie and Witt (1976), Morgan et al. (1976), Mathis (1983), and Chlewicki and Mayo Greenberg (1984). The grey areas corresponds to the B, R and J broad bands.

The albedo and the scattering phase function depends on several parameters as the composition, the shape and the size of the dust grains. Besides, due to the wavelength dependence of the phase function, the emerging flux from a certain region depends on the geometrical distribution of the dust and the source of radiation. For example, if the dust is located behind and/or besides the source of radiation with respect to us, the probability for a blue photon to be scattered into our line of sight is greater than for a red photon. This effect is clearly seen in reflection nebulae, as Figure 1.5 shows.

The extinction over the electromagnetic spectrum along a certain line of sight, frequently referred as the *extinction curve* or *extinction law*, can be obtained by comparing the observed

Figure 1.5: Image of the reflection nebula NGC 6726 by Marco Lorenzi. The characteristic blue colour is produced by selective scattering of blue photons by dust grains.

spectrum of a star in that line of sight with the intrinsic spectrum of such star, which can be approximated by the spectrum of another star of the same spectral type and luminosity class but unaffected by dust extinction.

The difference in extinguished magnitudes between the V broad band and any other wavelength, λ, is known as the *colour excess*:

$$E_{\lambda-V} = A_\lambda - A_V \tag{1.6}$$

Cardelli et al. (1989) derived an average empirical extinction curve for the different phases of the ISM by unifying the results of previous studies. Their extinction curve is parametrised only in terms of $\mathrm{R_V = A_V/E_{B-V}}$, where $\mathrm{E_{B-V}}$ is the colour excess of the B broad band. The extinction curve (see Figure 1.6) shows two aspects that appear to be common to all lines of sight. The first aspect is that the extinction increases approximately linearly with decreasing wavelength, which indicates that dust grains must have sizes comparable to the UV/optical wavelengths. The second aspect is the bump located at $\lambda \sim 220\,\mathrm{nm}$, which as we seen in Figure 1.4, is mainly due to absorption.

In their paper, Cardelli et al. (1989) give the analytical expression of the extinction law in the range from 0.125 to $3.5\,\mu\mathrm{m}$. To obtain an expression, the authors derived for all the optical wavelengths (λ_i) the least-square coefficients a_i and b_i from a linear fit to A_{λ_i}/A_V versus R_V^{-1}. Then, they performed a polynomial fit[1] in terms of $x \equiv 1/\lambda$ to obtain the correspondent functions a(x) and b(x). Their extinction law is finally expressed as:

$$\left\langle \frac{A_\lambda}{A_V} \right\rangle = a(x) + \frac{b(x)}{R_V} \tag{1.7}$$

We want to stress that the extinction law of Cardelli et al. (1989) only depends on R_V. The coefficients a(x) and b(x) are the same at all of the lines of sight. On the other hand, the value of R_V shows important variations in different lines of sight and those variations produce different extinction laws in different lines of sight due to the different composition and size of the dust grains that we find in the different phases of the ISM.

In order to measure the attenuation in a simple case, it is assumed that the dust is distributed in a foreground screen far from the source of radiation. Under these conditions, scattering of photons into our line of sight may be neglected as an approximation and the incident flux on the dust screen, $I_0(\lambda)$, the emergent flux, $I(\lambda)$, and the extinction, A_λ, at a certain wavelength λ, are related by the equation:

$$I(\lambda) = I_0(\lambda)\, 10^{-A_\lambda/2.5} \tag{1.8}$$

where A_λ is expressed in magnitudes[2].

1.3.2 Dust emission

Besides the decrease in the luminosity of the stellar light, dust absorption of photons leads to the heating of the grains. The temperature of the grains is determined by the balance between the energy absorbed from the stellar photons and the energy emitted by the grain. Since most dust grains are macroscopic particles, their emission spectra are determined by their temperature.

---

[1] The extinction law is frequently represented versus $1/\lambda$ instead of λ to highlight its optical/UV part. For this reason, the polynomial fit is performed in terms of the inverse of the wavelength.

[2] Frequently, the dust extinction is expressed in terms of the optical depth τ instead of in terms of magnitudes. In that case, Equation 1.8 is written as $I(\lambda) = I_0(\lambda)\, e^{-\tau_\lambda}$. From these two equations, we obtain the relation $\tau_\lambda = 1.086\, A_\lambda$.

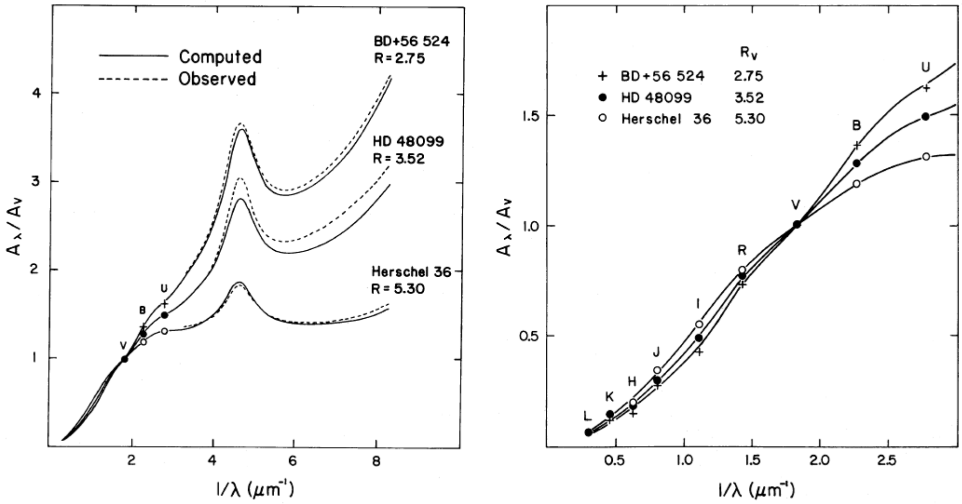

Figure 1.6: Original figures presented by Cardelli et al. (1989) showing the extinction curve in three different lines of sight. The left panel shows the curve from UV to IR wavelengths, and the right panel is a zoom-in from the optical to the IR.

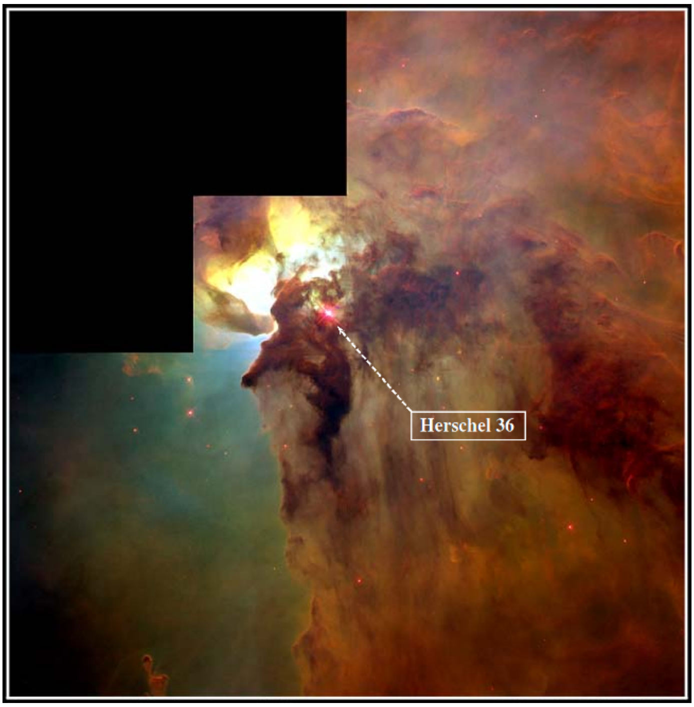

Figure 1.7: HST image of the young star Herschel 36 at the centre of the Lagoon Nebula (M8). For this star, still embedded in the parental cloud, Cardelli et al. (1989) reported an extinction law with R_V = 5.30 (see Figure 1.6).

If we approximate the dust grains by spherical particles of radius a and an absorption efficiency Q_a, the total absorbed energy by the grain, E_{abs}, is expressed as:

$$E_{abs} = 4\pi a^2 \times \int_0^\infty Q_a(\nu)\pi \frac{cu_\nu}{4\pi} d\nu \tag{1.9}$$

where u_ν is the density of the radiation field at the frequency ν. The same grain at a temperature T emits a total energy E_{em}:

$$E_{em} = 4\pi a^2 \times \int_0^\infty Q_a(\nu)\pi B_\nu(T) d\nu \tag{1.10}$$

where $B_\nu(T)$ is the Planck function.

If the grain is in thermal equilibrium with the stellar radiation field, the energy absorbed is equal to the energy emitted, which leads to the equality:

$$\int_0^\infty Q_a(\nu)\frac{cu_\nu}{4\pi} d\nu = \int_0^\infty Q_a(\nu) B_\nu(T) d\nu \tag{1.11}$$

These equations can be used to calculate the grain temperature distribution when the stellar radiation field is known.

Big grains, with their large heating capacities, are well described by thermal equilibrium as described above. Big grains are capable of absorbing UV/optical photons without appreciable variation of their temperature (see the two top panels in Figure 1.8). These grains dominate the dust emission at wavelengths longer than $60\,\mu$m.

However, the thermal equilibrium is not a valid approximation for all the grain species in the ISM. For very small grains (VSGs) and for polycyclic aromatic hydrocarbons (PAHs), which have smaller heating capacities due to their smaller sizes, the absorption of an UV photon leads to strong increase of their temperature followed by a rapid cooling. Then, these grains spend some time at low temperatures until another photon is absorbed (see the two bottom panels in Figure 1.8). This situation, with strong temperature variations, is clearly far from the situation of thermal equilibrium.

1.4 Dust in dwarf starbursting galaxies

Dwarf galaxies are the most numerous population of galaxies in the Universe (Grebel, 2001). With masses in the range of 10^8 to $10^9\,M_\odot$, these galaxies are placed at the lower end of

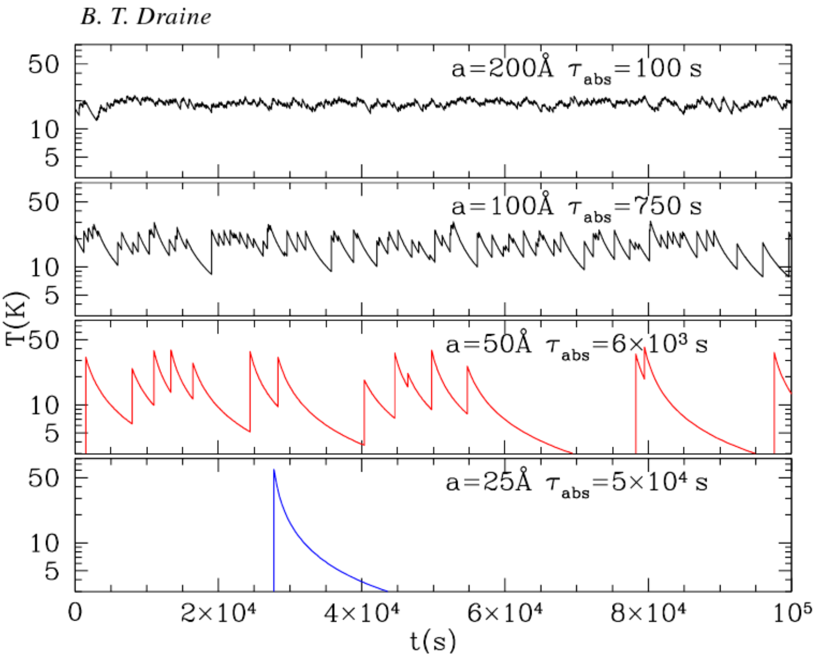

Figure 1.8: Original figure from Draine (2004) showing ”a day in the life of 4 carbonaceous grains”, exposed to the average starlight background. τ_{abs} is the mean time between photon absorptions and a is the radius of the grain.

the galaxy mass distribution. Dwarf galaxies characteristically have low metallicities and consequently low dust abundances.

Starbursts are mostly found in dwarf irregular galaxies, and contribute $\sim 25\%$ of the whole massive SF of the local universe (Heckman 1998). The dust re-emission at infrared wavelengths of the light emitted by the young stars is a key observation for understanding the process of star formation. Dwarf galaxies are relatively simple systems which makes them excellent targets to study the role of the dust in the SF process.

The dust spectral energy distribution (SED) of dwarf galaxies frequently shows differences to those of spiral galaxies. The main differences are:

- The SED of dwarf galaxies shows a relatively low emission at $8\,\mu$m, most likely due to a relatively lower content of polycyclic aromatic hydrocarbons (PAHs) at low metallicities (e.g. Draine et al. 2007, Galliano et al. 2008, Engelbracht et al. 2008). PAH are easily destructed in UV radiation fields. The intense ISRF in dwarf galaxies produced by a high SF and a lack of dust shielding could therefore be responsible for a destruction of PAHs.

- A submm ”excess” has been found in the SED of many, mostly actively star-forming, low-metallicity galaxies (Lisenfeld et al. 2002, Galliano et al. 2003, 2005, Bendo et al. 2006, Galametz et al. 2009, 2011, Israel et al. 2010, Bot et al. 2010, Dale et al. 2012, Planck Collaboration et al. 2011a). Different reasons have been suggested to explain this excess: (1) A large amount of cold (< 10 K) dust (Galliano et al. 2003, 2005, Galametz et al. 2009, 2011). However, extraordinarily large dust masses are needed for this explanation and it is unclear how these large amounts of cold dust can be shielded efficiently from the interstellar radiation field (ISRF). (2) A low value of the dust emissivity spectral index of $\beta = 1$ in the submm. Different dust grains have been suggested that could be responsible for this, from very small grains (Lisenfeld et al. 2002), fractal grains (Reach et al. 1995) to amorphous grains (Meny et al. 2007). (3) Spinning grains (Ferrara and Dettmar 1994; Draine and Lazarian 1998). Bot et al. (2010) showed that this grain type could explain the submm and mm excess in the Large and Small Magellanic Cloud. (4) Emission from dust in the outer regions of the galactic disks or the surrounding intergalactic medium (Popescu et al. 2002). (5) Magnetic nanograins, which can produce magnetic dipole radiation at microwave and submillimeter wavelengths (Draine and Hensley 2012).

It is also noteworthy that one sees a variety of FIR colours for gas rich dwarf galaxies, with examples of warm FIR SEDs (as found from IRAS colours - e.g. Melisse and Israel 1994), or of cold FIR SEDs (as revealed by ISO and Herschel measurements extending longwards of 100μm - e.g. Popescu et al. 2002, Grossi et al. 2010). Such variety may not be too surprising given that the star formation in dwarf galaxies is likely fundamentally bursty in nature. If we interpret the FIR SED in terms of the combination of cooler distributed cirrus dust emission and warm dust emission from grains in SF regions, the latter opaque structures should be most prominent in the early stages of the evolution of a starburst leading to a warm FIR SED. Over time the starburst fades, leaving the cirrus component and a cooler FIR SED. Other factors potentially contributing to the observed variety in FIR colours are differences in the contribution of very small grains (e.g. Galliano et al. 2003, 2005) and the possible presence of extended cold dust outside the main star forming disk of the galaxy (Popescu et al. 2002).

1.5 The dwarf galaxies NGC 4214 and NGC 4449

For our study of the SED of dwarf galaxies we chose the two nearby starbursting dwarf galaxies NGC 4214 and NGC 4449. Both are nearby galaxies, which allow us to separate the dust emission from the SF regions and from the diffuse dust, and both are located well above the Galactic disk, in the constellation of Canes Venatici, which makes the contribution from the dust in the Milky Way negligible. In Table 1.2 relevant information about these two galaxies is given.

Galaxy	NGC 4214	NGC 4449
RA (J2000)	12h15m39.2s	12h28m11.1s
DEC (J2000)	36°19′37.″0	44°05′37.″0
Distance (Mpc)	2.94 ± 0.18 [1]	3.82 ± 0.27 [2]
d_{25}	6.8′ [3]	4.7′ [3]
Inclination	44° [4]	60° [4]
M_{HI} ($M_\odot$)	0.4×10^9 [4]	1.1×10^9 [4]
Metallicity ($Z_\odot$)	0.36 ± 0.05 [5]	0.45 ± 0.07 [6]

Table 1.2: General properties of the dwarf galaxies NGC 4214 and NGC 4449. References: [1] Maíz-Apellániz et al. (2002). [2] Annibali et al. (2008). [3] Taken from the HyperLeda database. [4] Walter et al. (2008). [5] Kobulnicky and Skillman (1996) [6] Average value from Lequeux et al. (1979), Talent (1980), and Martin (1997).

1.5.1 NGC 4214

Located at a distance of D=2.94 Mpc (Maíz-Apellániz et al. 2002), NGC 4214 is a Magellanic starbursting dwarf irregular galaxy (de Vaucouleurs et al. 1991a) which shows a large degree of structure, from HI holes and shells (McIntyre 1998) typical of dwarf galaxies (Walter and Brinks 1999) to clear indications of a spiral pattern and a central bar. The molecular gas traced by the CO(1-0) line shows three well differentiated CO emitting complexes (Walter et al. 2001) related to the main SF complexes. NGC 4214 is a gas rich galaxy: the total mass of atomic gas is $M_{HI} = 4.1 \times 10^8\, M_\odot$ (Walter et al. 2008), and the molecular gas mass is $M_{H_2} = 1.5 \times 10^7\, M_\odot$ (Schruba et al. 2012, obtained with a Galactic conversion factor).

Karachentsev et al. (2004) reported for NGC 4214 a stellar mass of $\sim 1.5 \times 10^9 M_\odot$, similar to the mass found in the Large Magellanic Cloud (LMC). Ultraviolet (UV), optical and near-infrared (NIR) images of NGC 4214 show that the young stellar population is embedded in a smooth disk of old stars (see the large field of Fig.1.9), which can account for a significant fraction (~ 75%) of the total stellar mass (Williams et al., 2011). Despite this high fraction of old stars, NGC 4214 is a galaxy with an intense recent star formation activity, as shown by the two star forming complexes located in its centre and frequently referred in the literature as NGC 4214-NW and NGC 4214-SE. When resolved, the two complexes show individual smaller knots of star formation (see the small field of Fig.1.9). One of the most striking features in these complexes is the large shell structure in the NW region, where most of the gas in front of the central star cluster seems to have been removed by the action of stellar winds and supernovae (SNe) (Maíz-Apellániz et al. 1998; MacKenty et al. 2000). NGC 4214-

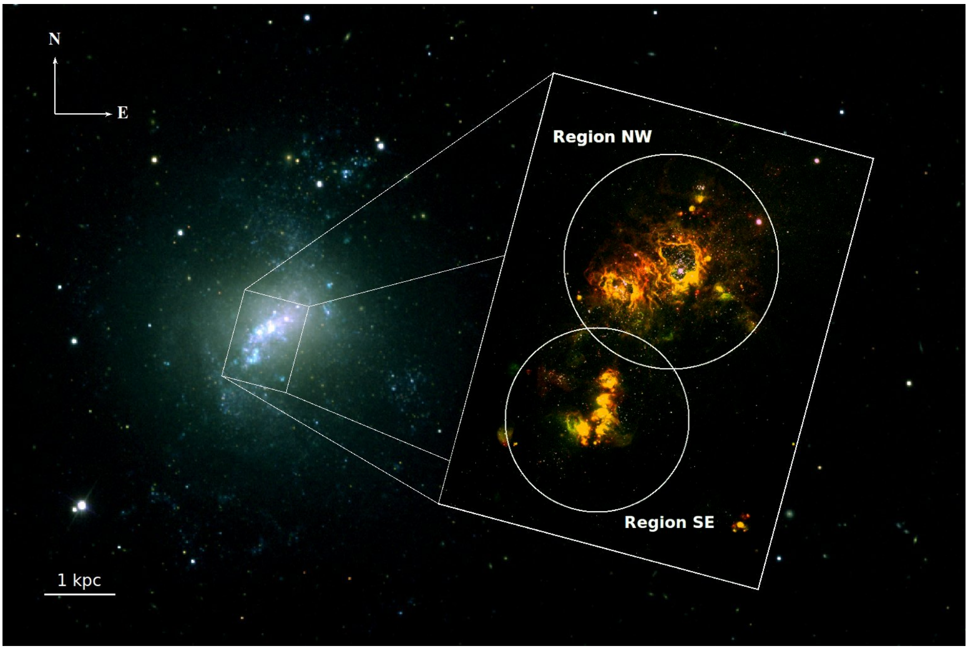

Figure 1.9: Combined SLOAN and HST image of NGC 4214. Large field: Image of NGC 4214 from a RGB combination of SLOAN r, g and u bands. Zoom-in: Image of the centre of NGC 4214 from a RGB combination of HST-WFC3 filters F657N (H_α + cont), F502N ([OIII] + cont) and F336W (cont).

SE is more compact and shows no clear evidence of a decoupling between the star clusters and the gas. The morphological differences for the two complexes were interpreted as an evolutionary trend by MacKenty et al. (2000). Using stellar synthesis models, Úbeda et al. (2007) determined the age, the mass, the radius and the extinction of the star clusters within the NW and SE complexes. They found an age of 5 Myr for the star clusters in the NW region, whereas the age of the star clusters of the SE region ranges from 1.7 to 4.0 Myr.

The metallicities of both SF regions have been measured by Kobulnicky and Skillman (1996), who found values of 12+log(O/H) = 8.17± 0.02 for the NW and 8.27± 0.02 for the SE region. With the Solar abundance 12 + log(O/H) = 8.66 (Asplund et al. 2005), as used in Groves et al. (2008), this gives $Z = 0.32\ Z_\odot$ for NW and $Z = 0.41\ Z_\odot$ for SE.

1.5.2 NGC 4449

Located at a distance of D = 3.82 ± 0.27 Mpc (Annibali et al. 2008), NGC 4449 is one of the most luminous an active nearby Magellanic star bursting dwarf galaxies (see Fig. 1.10).

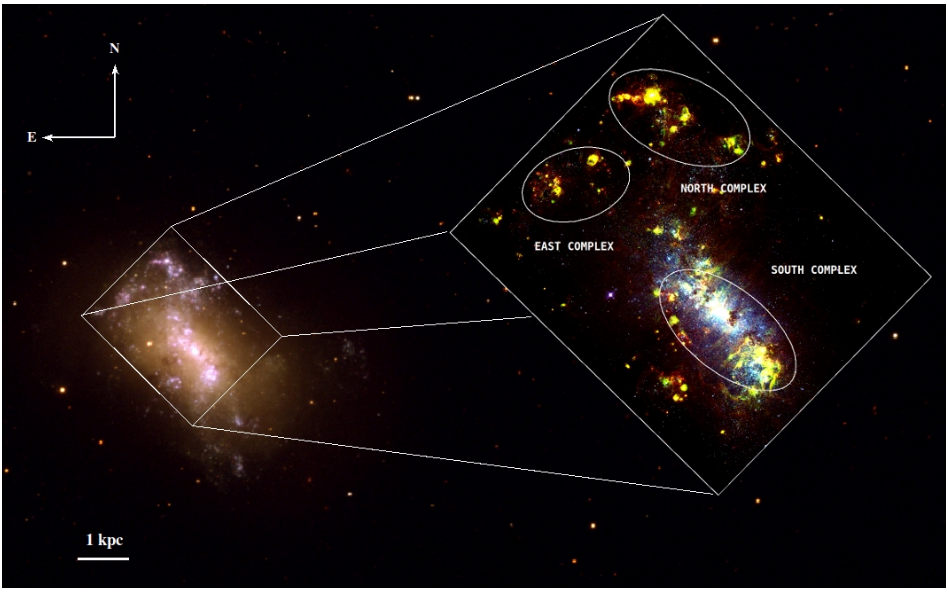

Figure 1.10: Combined SLOAN and HST image of NGC 4449. Large field: Image of NGC 4449 from a RGB combination of SLOAN r, g and u bands. Zoom-in: Image of the centre of NGC 4449 from a RGB combination of HST-ACS filters F658N (H_α + cont), F502N ([OIII] + cont) and F550M (cont).

NGC 4449 has almost certainly undergone an external perturbation, as is evident from HI studies revealing extended streamers wrapping around the galaxy and counter-rotating (inner and outer) gas systems (Hunter et al. 1998, Theis and Kohle 2001, and references therein). In contrast to NGC 4214, the current SF in NGC 4449 is not constrained to the centre but it is occurring throughout the galaxy (Hunter 1997). Thronson et al. (1987) estimated a current SFR = $1.5\,M_\odot\,yr^{-1}$.

Reines et al. (2008) identified 13 thermal radio sources and derived their physical properties using both nebular emission from the HII regions and the stellar continuum. These radio-detected clusters have ages $\lesssim$5 Myr and stellar masses of the order of $10^4\,M_\odot$.

For NGC 4449, abundance estimates were derived in the HII regions by Lequeux et al. (1979) (12 + log(O/H) = 8.38), Talent (1980) (12 + log(O/H) = 8.23), and Martin (1997) (12 + log(O/H) = 8.31). The average value provide $Z = 0.45 \pm 0.07\,Z_\odot$.

1.6 Goals of this thesis

The goal of our study is to understand the properties and the spatial distribution of the interstellar dust in dwarf galaxies from both the perspective of the attenuation of the radiation and the re-emission. High resolution data from SPITZER, HERSCHEL and PLANCK allow us to probe the entire spectral energy distribution (SED) of morphologically separated components of the dust emission from nearby galaxies and allow a more detailed comparison between data and theory.

In the first part of this thesis we carry out the study of the dust in the SF regions of the dwarf starbursting galaxy NGC 4214. Our aim is to check different extinction laws and geometrical scenarios.

In the second part we carry out the study of the dust emission of NGC 4214 and NGC 4449 in order to check whether the SED of these objects can be reproduced with radiation transfer models based on Galactic dust properties. One of the key points of our study is that for the first time, the SED was studied separately for the dust within the HII regions and their associated PDRs and for the diffuse dust.

CHAPTER 2

Dust extinction in NGC 4214

"I say there is no darkness but ignorance."

– William Shakespeare (*Twelfth Night*, 1602)

In Section 1.3.1 we presented the selective extinction produced by the dust absorption and scattering of the stellar photons. In this section, we make use of this selective extinction to calculate extinction maps of the photo-ionised regions of NGC 4214. The study of the extinction allows us to obtain a complementary view of the dust properties and of its geometrical distribution to that obtained from its emission (see Section 4). Another important motivation to calculate maps of the extinction produced by the dust present in NGC 4214 is that the resolution achieved with the HST is about one order of magnitude better than the best dust emission map (which is obtained in the PAHs regime with the photometer IRAC onboard the Spitzer space telescope). This improvement in angular resolution allows us to obtain a small-scale picture of the dust distribution.

As we already mentioned in the previous section, NGC 4214 is a nearby Magellanic star bursting dwarf irregular galaxy (de Vaucouleurs et al. 1991a). Due to its proximity and the low foreground extinction in its line of sight, NGC 4214 is an excellent target to test the dust distribution in massive star forming regions. The star formation activity in NGC 4214 is mainly concentrated in two star forming complexes located at its centre and frequently referred in the literature as NGC 4214-NW and NGC 4214-SE.

Bounding the selective extinction and the photo-ionisation equilibrium, it is possible to obtain a measure of the dust extinction in ionized regions by comparing the observed fluxes of two emission lines of different wavelength. Let us consider two different recombination lines, located at wavelengths λ_1 and λ_2. The relation between their observed and intrinsic fluxes and the extinction can be expressed using Equation 1.8 as:

$$I_{\lambda_1} = I^0_{\lambda_1} \times 10^{-A_{\lambda_1}/2.5} \tag{2.1}$$

$$I_{\lambda_2} = I^0_{\lambda_2} \times 10^{-A_{\lambda_2}/2.5} \tag{2.2}$$

From the ratio of these two equations it is possible to obtain the following expression:

$$A_{\lambda_1} - A_{\lambda_2} = -2.5 \log \left(\frac{I_{\lambda_1}/I_{\lambda_2}}{I^0_{\lambda_1}/I^0_{\lambda_2}} \right) \tag{2.3}$$

In order to convert Equation 2.3 to express the extinction in magnitudes in the V-band, it is possible to use the Cardelli et al. (1989) extinction law to write the difference $A_{\lambda_1} - A_{\lambda_2}$ in terms of A_V as:

$$A_{\lambda_1} - A_{\lambda_2} = \frac{A_V}{C(R_V, \lambda_1, \lambda_2)} \tag{2.4}$$

where the factor of conversion $C(R_V, \lambda_1, \lambda_2)$ depends on the value of R_V in the line of sight and on the wavelengths of the two lines considered. From Equations 2.3 and 2.4, we obtain the following expression:

$$A_V^{\lambda_1/\lambda_2} = -2.5 \times C(R_V, \lambda_1, \lambda_2) \times \log \left(\frac{I_{\lambda_1}/I_{\lambda_2}}{I^0_{\lambda_1}/I^0_{\lambda_2}} \right) \tag{2.5}$$

where we made use of the superscript λ_1/λ_2 to distinguish between different maps obtained with different lines. The corresponding error map, $\Delta A_V^{\lambda_1/\lambda_2}$, can be calculated using the standard error handling formulation:

$$\Delta A_V^{\lambda_1/\lambda_2} = 2.5 \times C(R_V, \lambda_1, \lambda_2) \times \log e \times \sqrt{\left(\frac{\Delta I_{\lambda_1}}{I_{\lambda_1}} \right)^2 + \left(\frac{\Delta I_{\lambda_2}}{I_{\lambda_2}} \right)^2} \tag{2.6}$$

The last equation can be expressed in terms of the relative errors as:

$$\Delta A_V^{\lambda_1/\lambda_2} = 2.5 \times C(R_V, \lambda_1, \lambda_2) \times \log e \times \sqrt{(\delta I_{\lambda_1})^2 + (\delta I_{\lambda_2})^2} \tag{2.7}$$

As we mentioned in Section 1.2, the recombination line spectrum is emitted by atoms that have captured of electrons into excited levels which are now cascading via radiative transitions to the ground level. The number of transitions between two levels will be determined by the probability of such transition occur. Therefore, although we do not know the intrinsic fluxes $I^0_{\lambda_1}$ and $I^0_{\lambda_2}$, their ratio only depend on the different probabilities of the corresponding transitions. In Table 1.1 are listed the transition probabilities of the Hydrogen atom for Case B and the typical values of photo-ionised regions $T = 10^4$ K and $N_e = 100\,\mathrm{cm}^{-3}$. In this chapter we make use of the Equation 2.5, the values of Table 1.1 and the Cardelli et al. (1989) extinction law to obtain extinction maps of the dust extinction calculated by comparing three different Hydrogen recombination lines.

2.1 Data reduction

Wide Field Camera 3 (WFC3) data were obtained for NGC 4214 as part of the WFC Science Oversight Committee (SOC) Early Release Science (ERS) program (program ID11360, P.I. Robert O'Connell). A total of 7 stellar and 7 nebular images were taken using UVIS and IR cameras. Both cameras onboard the HST have a field of view of ~2′ and they cover the central star forming complexes NW and SE, allowing us to separate them into several smaller star forming regions. We obtained calibrated maps in the UV filters F225W, F336W, F373N, F438W, F487N, F502N, F547M, F657N, F673N and F814W and in the IR filters F128N, F110W, F160W and F164N from the HST Data Archive (see the WFC3 website[1]). In Table 2.1 the specifications of these filters are given.

FILTER	Description	Date	Exposure (s)
UVIS-F225W	UV wide	2009-12-23	1665.0
UVIS-F336W	U, Strmgren u	2009-12-23	1683.0
UVIS-F373N	[OII] 3726/3728	2009-12-25	1260.0
UVIS-F438W	WFPC2 B	2009-12-22	1530.0
UVIS-F487N	Hβ	2009-12-23	1760.0
UVIS-F502N	[OIII] 5007	2009-12-24	1470.0
UVIS-F547M	Strmgren y	2009-12-23	1050.0
UVIS-F657N	Hα+[NII]	2009-12-23	1592.0
UVIS-F673N	[SII] 6717/6731	2009-12-25	2940.0
UVIS-F814W	WFPC2 Wide I	2009-12-23	1339.0
IR-F110W	Wide YJ	2009-12-22	1197.7
IR-F128N	Pβ	2009-12-23	1197.7
IR-F160W	WFC3 H	2009-12-22	2397.7
IR-F164N	[Fe II]	2009-12-23	2397.7

Table 2.1: Summary of HST-WFC3 observation of NGC 4214.

---

[1] http://www.stsci.edu/hst/wfc3/

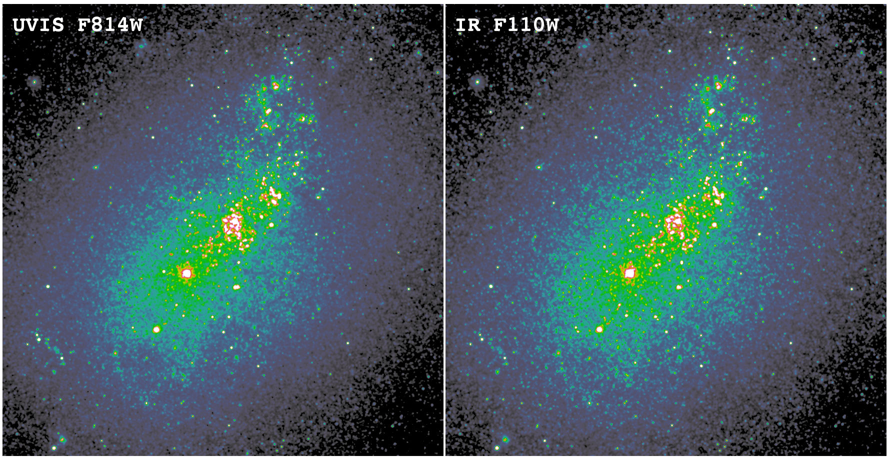

Figure 2.1: Comparison of the UVIS F814W (left) and IR F110W (right) filters. After the reduction performed, both filters are at the same resolution and pixels size and therefore, they can be compared in a pixel-by-pixel basis.

We use the output of the HST data archive pipeline *calwf3*, which applies the standard calibrations to the raw images (flat-fielding, dark subtraction, etc.) as input of the *Multidrizzle* software (Fruchter and Hook 2002) to correct for geometric distortion and to produce the final maps. The output of the *Multidrizzle* is the final geometric distortion corrected and cosmic-ray rejected mosaicked image for each filter.

The field of view (FoV) of the WFC3 only covers an area of ~2′×2′ at the centre of the galaxy. From the stellar luminosity profile shown in the top panel of Figure 4.11, we estimated that the flux density coming from the stellar disk in the outer part of the FoV (R~1′) is more than one order of magnitude larger than the sky value (R~5′). For this reason, we did not perform any sky subtraction with the *Multidrizzle* software.

FILTER	λ_0	Bandwidth	PHOTFLAM
	Å	Å	ergs cm^{-2} Å^{-1}/e^{-}
F438W	4325	618	6.8193979×10^{19}
F487N	4871	60	5.9564300×10^{18}
F547M	5447	650	4.7446573×10^{19}
F657N	6567	121	2.1244385×10^{18}
F110W	11534	4430	1.5232943×10^{20}
F128N	12832	159	4.1030084×10^{19}
F160W	15369	2683	1.9106045×10^{20}

Table 2.2: Specifications of the filters used to study the extinction in the SF regions NW and SE. The calibration factor shown in the fourth column, PHOTFLAM, was used to convert e^{-} into flux density.

In order to be able to compare the data from UVIS and IR cameras in a pixel-by-pixel basis, we followed the next steps:

i) We used the IRAF task *imexam* to measure the FWHM on the output from the *Multidrizzle* software. Then, all the images were smoothed using the IRAF task to a common FWHM of 0.3″, which is slightly larger than the poorer resolution found in the data set.

ii) We used the IRAF task *wregister* to convert the images from UVIS to the pixel size of IR (0.128″).

iii) We used the IRAF task *imalign* to align all of our filters based on a sample of 50 stars visible in all the filters. For all the filters, the error in the alignment was less than 0.06″, i.e., about half of the IR camera pixel size. After the alignment, the images were trimmed to the same FoV.

The observed flux densities include the extinction produced by the dust present in the Milky Way, which we want to exclude from our study. To correct for this, we made use of the values of the foreground galactic extinction in the line of sight of NGC 4214 reported by Schlafly and Finkbeiner (2011) (see Table 2.3). For all of our filters, we applied:

$$F_\lambda = F'_\lambda \times 10^{-A_\lambda/2.5} \tag{2.8}$$

where A_λ is the foreground Galactic extinction at the wavelength of the filter, and F'_λ and F_λ are the observed and the foreground corrected flux densities, respectively.

λ (nm)	350	470	540	640	750	890	1250	1660
A_λ (mag)	0.095	0.079	0.060	0.047	0.037	0.028	0.016	0.010

Table 2.3: Galactic extinction in the line of sight of NGC 4214 from the Schlafly and Finkbeiner (2011) recalibration of the Schlegel et al. (1998) infrared-based dust map.

2.2 Continuum subtraction

Besides the emission from the ionised gas, the narrow filters also contain the underlying emission from the stellar continuum. In order to isolate the gaseous component, we developed the IDL routine *LINEextractor*, which allows the user to perform a standard continuum subtraction based on the comparison of the flux densities measured for a sample of stars in both filters. The main advantage of this routine is the possibility of interactively select the stars used to perform the continuum stellar subtraction.

The input files necessary to run *LINEextractor* are the nebular image, from which we want to remove the continuum, and a pure stellar image. In a first step, *LINEextractor* superposes both images in a pop-up window and allow the user to select with the mousse the stars suitable to be considered to calculate the scale factor necessary to subtract the continuum. When the user clicks on a star, *LINEextractor* shows both 2D and 3D profiles in the surroundings of the star in order to allow the user to check if the star is well isolated (to avoid contamination from the gas emission) and if it presents a gaussian profile (a non-gaussian profile might be an indicator of a non-stellar nature). If the object does not fulfil the requirements, then the user can neglect it and select another star. On the other hand, when the requirements are fulfilled, the routine perform aperture photometry in a circular aperture over the two filters in a radius which is twice the FWHM of the images and stores the measured fluxes.

Once the number of selected stars is satisfactory, *LINEextractor* calculates the scale factor by means of a linear fit of the stored values. The flux density of the line, F_{line}, is then calculated as:

$$F_{line} = F_{narrow} - a \times F_{stellar} \tag{2.9}$$

where $\mathrm{F_{narrow}}$ is the flux density of the narrow filter (line+stellar), $\mathrm{F_{stellar}}$ is the flux density of the stellar filter, and a is the scale factor obtained from the linear fit. At this stage, the routine multiplies $\mathrm{F_{line}}$ ($\mathrm{ergs\,cm^{-2}\,s^{-1}\,\AA^{-1}}$) by the corresponding bandwidth of the filter (in Å, see Table 2.1) to obtain the intensity of the line, $\mathrm{I_{line}}$ ($\mathrm{ergs\,cm^{-2}\,s^{-1}}$).

Finally, the routine shows the line emission image in a window in order to allow the user to select with the mousse some background apertures which are used to compute the noise (σ) of the resulting image. At the end of the process, the output created by *LINEextractor* consists in both the pure nebular image and the correspondent relative error map, which is calculated in a pixel-by-pixel basis as:

$$\delta I^{SN}_{line}(i, j) = \frac{\sigma}{I_{line}(i, j)} \tag{2.10}$$

It is important to note here that continuum subtraction is not a perfect process. Frequently, the line emission image shows stars that were under/over-subtracted. This effect is specially important in those regions where two populations of stars of different ages lie together, as it is the case of the SF regions of NGC 4214. In order to take into account the possible existence of two different underlying star populations, *LINEextractor* allows the user to use a second stellar filter located at the opposite side of the spectrum of the narrow filter. In this case, the subtraction process is identical as described above, with the exception that it runs in parallel for both stellar filters, i.e., *LINEextractor* scales and subtracts the second stellar filter and therefore, it calculates a secondary pure line emission image. This second image is then used to produce a second relative error map based on the differences found between the first, $\mathrm{I}_{\mathrm{line}}$, and the second, $\mathrm{I}'_{\mathrm{line}}$, emission images as it follows:

$$\delta I_{line}^{cont}(i,j) = \frac{\left|I_{line}(i,j) - I'_{line}(i,j)\right|}{I_{line}(i,j)} \tag{2.11}$$

The final error map of I_{line} is calculated as the quadratic sum of the error maps corresponding to the noise and to the continuum subtraction as:

$$\delta I_{line}(i,j) = \sqrt{\delta I_{line}^{cont}(i,j)^2 + \delta I_{line}^{SN}(i,j)^2} \tag{2.12}$$

In Figure 2.2 the operation scheme of *LINEextractor* is shown. The pure emission line maps generated by the routine are shown in Figure 2.3.

The F657N filter contains, besides the Hα emission, the emission from the forbidden lines [N$_{\mathrm{II}}$] λ6548 and [N$_{\mathrm{II}}$] λ6583. In order to subtract the contribution of these two lines, we used the intrinsic ratios of Hα and the Nitrogen lines found in the Orion nebula (Irwin 1968), which are 0.16 and 0.05 for Hα/[N$_{\mathrm{II}}$] λ6548 and Hα/[N$_{\mathrm{II}}$] λ6583, respectively. At the wavelengths of [N$_{\mathrm{II}}$] λ6548 and [N$_{\mathrm{II}}$] λ6583, the transmission of the F657N is 0.8 and 0.7, respectively. Therefore, we estimated that the total contribution of these two lines is 17% of the total intensity measured in the filter.

2.3 Results

We analysed the dust extinction distribution of the SF regions of NGC 4214 using the line emission maps of Hβ, Hα and Pβ calculated with *LINEextractor* (see Figure 2.3).

2.3.1 Extinction maps

From the values of the probabilities of these transitions presented in Table 1.1, it is possible to know the ratio of the intrinsic emission that we would expect if no dust was present:

$$I^0_{H\alpha}/I^0_{H\beta} = 2.859 \tag{2.13}$$

$$I^0_{P\beta}/I^0_{H\alpha} = 0.057 \tag{2.14}$$

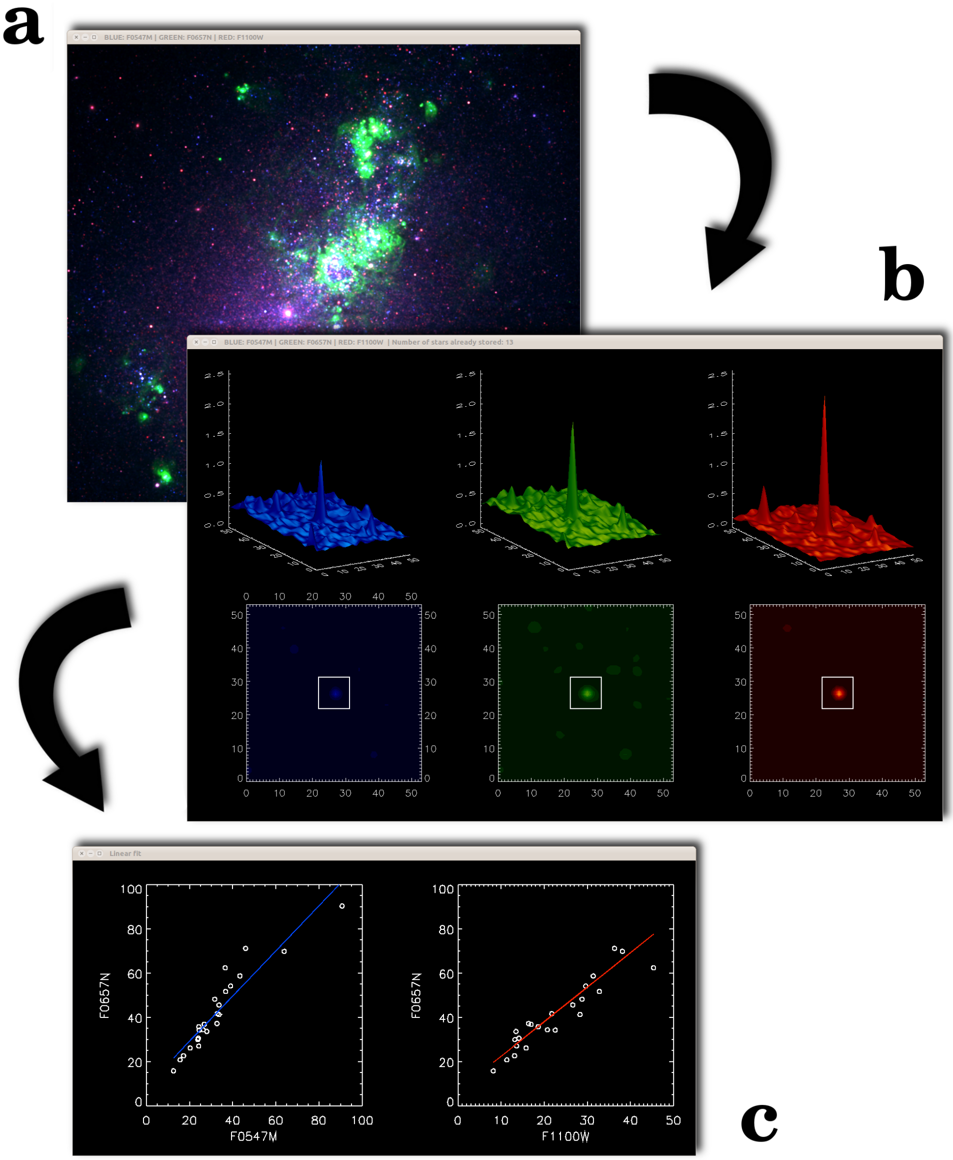

Figure 2.2: Operation scheme of the IDL routine *LINEextractor* used to subtract the underlying stellar continuum from the narrow band filters. **a)** In this example, the stellar filter F547M (in blue) is used as the first continuum of the narrow filter F657N (in green), whereas the stellar filter F110W (in red) is used as the second continuum. **b)** When clicking on a star, *LINEextractor* shows the stellar profiles (3D up and 2D down) of the three filters. In the 3D profiles, the units of the x and y axis are pixels, and for the z axis are 10^{-18} ergs cm^{-2} s^{-1} Å^{-1}. For the 2D profiles, the units of the x and y axis are pixels, and the contours corresponds to 0.1, 0.2, 0.3, 0.4, 0.5, 0.6, 0.7, 0.8 and 0.9 times the flux at the peak. When a star fulfils the requirements, the fluxes in the three bands are stored. **c)** Linear fit used to calculate the scale factor based on the measured fluxes. The units of the axis are 10^{-18} ergs cm^{-2} s^{-1} Å^{-1}.

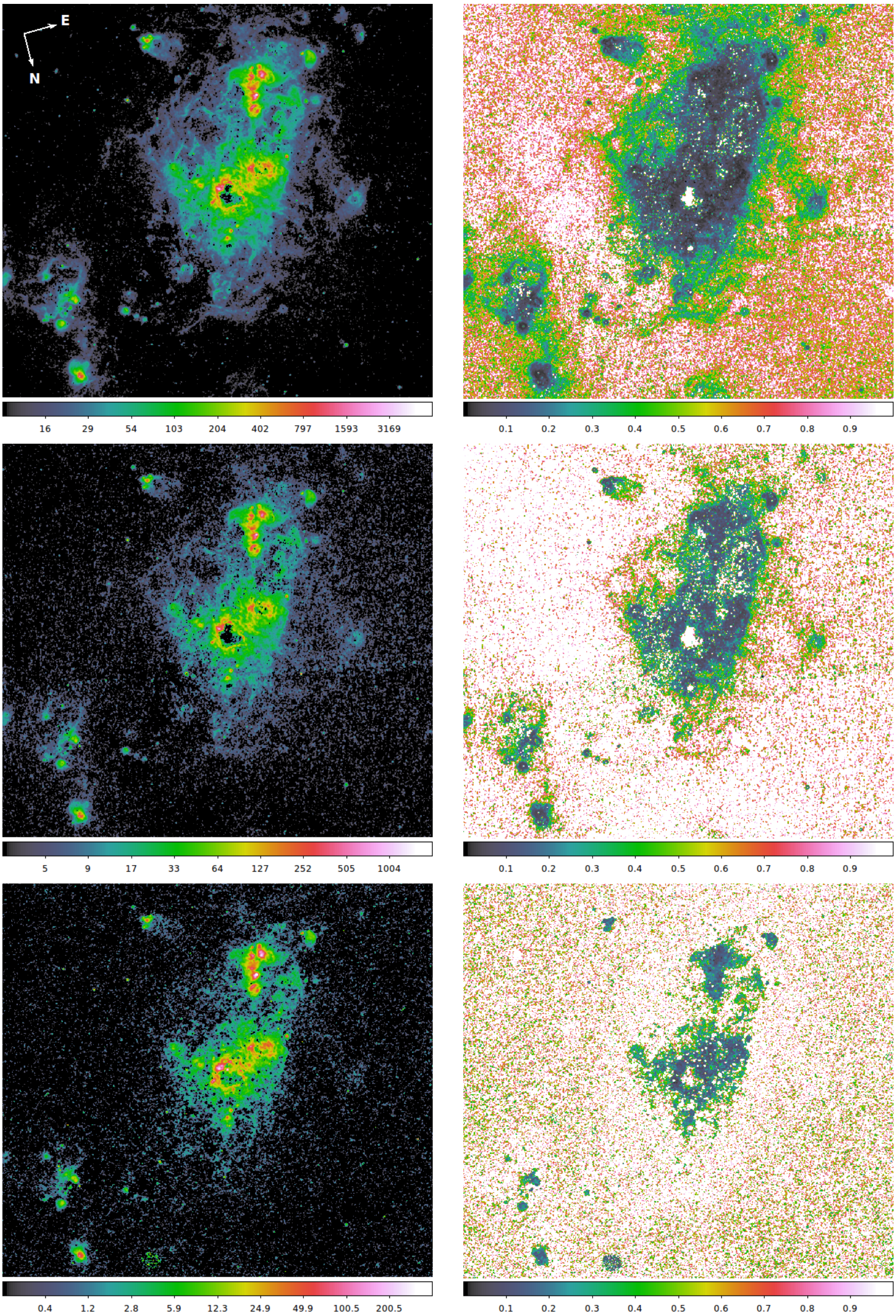

Figure 2.3: Continuum-subtracted (left) and relative error (right) maps of Hα (top), Hβ (middle) and Pβ (bottom) generated using *LINEextractor*. The units of the intensity maps are 10^{-18} ergs cm^{-2} s^{-1}. The area mapped is ~2′×2′, which at the distance of NGC 4214, corresponds to ~1.7×1.7 kpc.

$$I^0_{P\beta}/I^0_{H\beta} = 0.165 \tag{2.15}$$

Regarding the conversion factor $C(R_V, \lambda_1, \lambda_2)$, we need to assume a certain value with R_V. It is a frequent practice to choose the standard curve of $R_V = 3.1$, the value which is appropriate for the dust in the diffuse interstellar medium. However, since this work is focused on the SF regions of NGC 4214, the standard curve might be not accurate if dust in molecular clouds is present in the line of sight. Úbeda et al. (2007) used the IDL package *CHORIZOS* (see Maíz-Apellániz 2004) to fit stellar SEDs models to multicolour photometric data obtained with the WFPC2 onboard the HST. The input parameters of *CHORIZOS* are the age, the metallicity, the color excess E_{B-V} and R_V. With exception of the metallicity, which was fixed to $Z=0.4\,Z_\odot$, Úbeda et al. (2007) determined simultaneously the parameters using a likelihood-maximization technique. Their modelling yielded high values of R_V (5.0 and 5.9 for the NW and SE regions, respectively), which indicates the presence of molecular clouds in the line of sight. We adopted a Cardelli et al. (1989) extinction law of $R_V = 5.45$ (average value of Úbeda et al. 2007) and we also tested the results obtained for the standard law with $R_V = 3.1$. In Table 2.4 the different values of the conversion factor $C(R_V, \lambda_1, \lambda_2)$ corresponding to $R_V = 5.45$ and 3.10 are shown.

$Cv(R_V, \lambda_1, \lambda_2)$	$R_V = 5.45$	$R_V = 3.1$
$Cv(R_V, H\alpha, H\beta)$	-4.114	-2.886
$Cv(R_V, P\beta, H\alpha)$	-1.865	-1.831
$Cv(R_V, P\beta, H\beta)$	-1.283	-1.120

Table 2.4: Conversion factors obtained for the two values of R_V considered in this work. Note that the largest difference between the two extinction laws corresponds to $Cv(R_V, H\alpha, H\beta)$, whereas the smallest difference correspond to $Cv(R_V, P\beta, H\alpha)$. This makes the extinction map calculated with the Pβ and Hα lines the most robust against changes in the value of R_V.

From Equations 2.5 and 2.7, the intrinsic ratios presented in Equations 2.13 and the conversion factors shown in Table 2.4, it is possible to obtain, for $R_V = 5.45$, the following set of equations:

$$A^{H\alpha/H\beta}_{V,5.45} = 10.3 \times \log\left(\frac{I_{H\alpha}/I_{H\beta}}{2.859}\right) \tag{2.16}$$

$$\Delta A^{H\alpha/H\beta}_{V,5.45} = 4.47 \times \sqrt{(\delta I_{H\alpha})^2 + \left(\delta I_{H\beta}\right)^2} \tag{2.17}$$

$$A^{P\beta/H\alpha}_{V,5.45} = 4.66 \times \log\left(\frac{I_{P\beta}/I_{H\alpha}}{0.057}\right) \tag{2.18}$$

$$\Delta A_{V,5.45}^{P\beta/H\alpha} = 2.02 \times \sqrt{\left(\delta I_{P\beta}\right)^2 + (\delta I_{H\alpha})^2} \tag{2.19}$$

$$A_{V,5.45}^{P\beta/H\beta} = 3.21 \times \log\left(\frac{I_{P\beta}/I_{H\beta}}{0.165}\right) \tag{2.20}$$

$$\Delta A_{V,5.45}^{P\beta/H\beta} = 1.39 \times \sqrt{\left(\delta I_{P\beta}\right)^2 + \left(\delta I_{H\beta}\right)^2} \tag{2.21}$$

Note the use of the subscript 5.45 to distinguish between this set of equations and the set corresponding to $R_V = 3.1$, which adopts the form:

$$A_{V,3.1}^{H\alpha/H\beta} = 7.21 \times \log\left(\frac{I_{H\alpha}/I_{H\beta}}{2.859}\right) \tag{2.22}$$

$$\Delta A_{V,3.1}^{H\alpha/H\beta} = 3.13 \times \sqrt{(\delta I_{H\alpha})^2 + \left(\delta I_{H\beta}\right)^2} \tag{2.23}$$

$$A_{V,3.1}^{P\beta/H\alpha} = 4.58 \times \log\left(\frac{I_{P\beta}/I_{H\alpha}}{0.057}\right) \tag{2.24}$$

$$\Delta A_{V,3.1}^{P\beta/H\alpha} = 1.99 \times \sqrt{\left(\delta I_{P\beta}\right)^2 + (\delta I_{H\alpha})^2} \tag{2.25}$$

$$A_{V,3.1}^{P\beta/H\beta} = 2.80 \times \log\left(\frac{I_{P\beta}/I_{H\beta}}{0.165}\right) \tag{2.26}$$

$$\Delta A_{V,3.1}^{P\beta/H\beta} = 1.22 \times \sqrt{\left(\delta I_{P\beta}\right)^2 + \left(\delta I_{H\beta}\right)^2} \tag{2.27}$$

The extinction maps calculated with these equations are shown in Figure 2.4. The values of $\delta(\mathrm{I}_{\mathrm{H}\alpha})$, $\delta(\mathrm{I}_{\mathrm{H}\beta})$ and $\delta(\mathrm{I}_{\mathrm{P}\beta})$ were calculated using Equation 2.12. In the photo-ionised regions considered, the dominant source of error is the continuum subtraction. In order to avoid large extinction errors, we only consider those pixels where the relative error of all the three lines are simultaneously lower than 0.2. With this restriction the maximum error in our extinction maps is 1.26, 0.57, 0.39, 0.88, 0.56 and 0.34 mag for $\Delta\mathrm{A}_{\mathrm{V},5.45}^{\mathrm{H}\alpha/\mathrm{H}\beta}$, $\Delta\mathrm{A}_{\mathrm{V},5.45}^{\mathrm{P}\beta/\mathrm{H}\alpha}$, $\Delta\mathrm{A}_{\mathrm{V},5.45}^{\mathrm{P}\beta/\mathrm{H}\beta}$, $\Delta\mathrm{A}_{\mathrm{V},3.1}^{\mathrm{H}\alpha/\mathrm{H}\beta}$, $\Delta\mathrm{A}_{\mathrm{V},3.1}^{\mathrm{P}\beta/\mathrm{H}\alpha}$ and $\Delta\mathrm{A}_{\mathrm{V},3.1}^{\mathrm{P}\beta/\mathrm{H}\beta}$, respectively.

We need to avoid regions with high stellar absorption, which can be especially important for

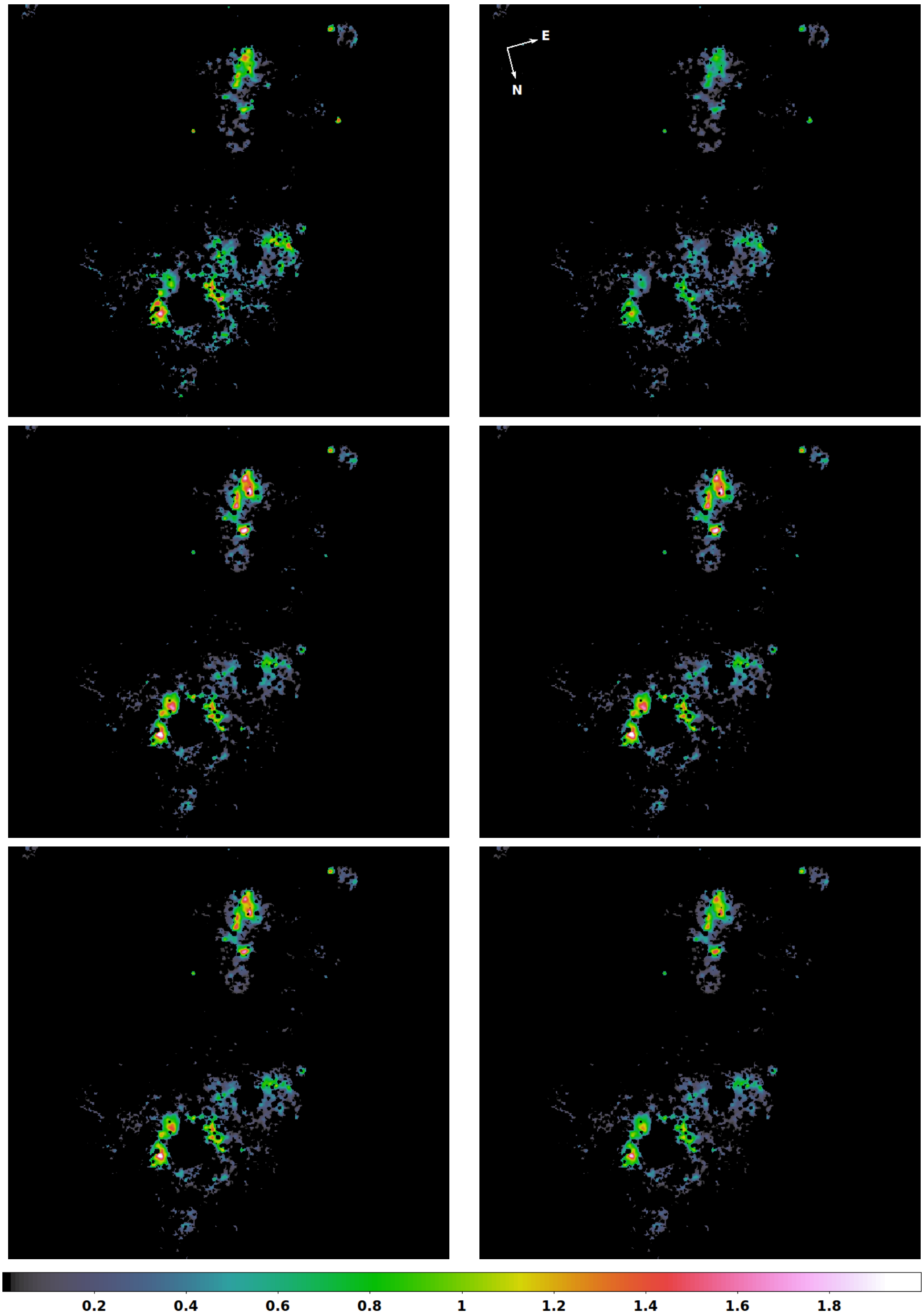

Figure 2.4: $A_V^{H\alpha/H\beta}$ (top), $\mathrm{A_V^{P\beta/H\alpha}}$ (middle) and $\mathrm{A_V^{P\beta/H\beta}}$ (bottom) extinction maps calculated using an extinction law of $\mathrm{R_V} = 5.45$ (left) and $\mathrm{R_V} = 3.10$ (right). The mapped area is $\sim 70'' \times 70''$ ($\sim 1 \times 1$ kpc).

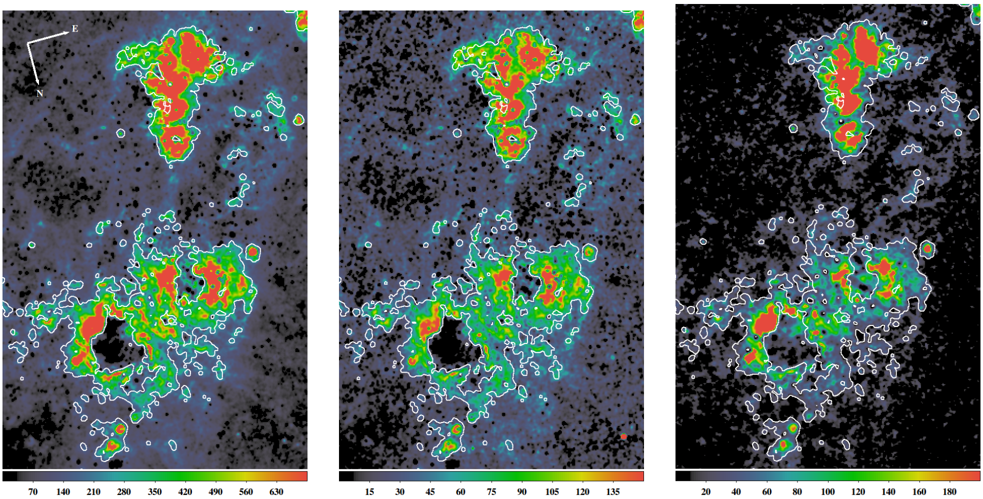

Figure 2.5: Equivalent width (Å) maps of Hα (left), Hβ (middle) and Pβ (right). The contour overlaid corresponds to the error cut applied.

Hβ. In order to do this, we made sure that we only derived the extinction for regions with a high equivalent width, which indicates that the emission from the ionised gas is dominant over stellar emission. Figure 2.5 shows maps of the equivalent width, overlaid with contours of our applied error cut. We see that the region considered for the calculation of the extinction coincides always with values of EW $\gtrsim$ 300, 70 and 40 Å for Hα, Hβ and Pβ, respectively; i.e., regions dominated by emission from ionised gas.

2.3.2 Comparison of the different extinction maps

The six extinction maps presented in Figure 2.4 trace, in general, very similar structures of the dust extinction. However, the exact value of the extinction changes depending on the line-ratio considered. This effect is especially noticeable for the $A_{V}^{H\alpha/H\beta}$ extinction maps, where the extinction is lower than for the other maps. This effect is stronger for the map calculated using R_{V} = 3.10 (see for example, the low values derived in the SE region, where the highest extinction measured with $A_{V,3.10}^{H\alpha/H\beta}$ are a factor ~2 lower than the values measured with $\Delta A_{V,3.10}^{P\beta/H\alpha}$ or $\Delta A_{V,3.10}^{P\beta/H\beta}$), but is also affecting the maps calculated with R_{V} = 5.45.

In order to provide a quantitative analysis of these differences, we carried out a detailed study comparing the extinction derived with different line-ratios on a pixel-by-pixel basis. We restricted our study to the photo-ionised regions shown in Figure 2.6 (see also the Table 2.5, where the apertures used to determine these regions are specified), since it is only in this phase of the ISM where the photo-ionisation equilibrium is achieved. We therefore neglected the study of the diffuse interstellar gas (DIG) surrounding the two main complexes because in this phase of the ISM other processes, like shocks, contribute to the ionization of the gas. In Figures 2.7 to 2.10 we show the plots with the the pixel-by-pixel comparison of $A^{P\beta/H\alpha}$ vs. $A^{H\alpha/H\beta}$ and $A^{P\beta/H\alpha}$ vs. $A^{P\beta/H\beta}$ for both values of $R_V = 3.10$ and 5.45 separately for each photo-ionised region.

The pixel-by-pixel plots show similarities and differences between the extinction derived from the different line-ratios:

- As expected from the generally good agreement between the maps, there is a positive correlation between the different extinction maps.
- For the regions with the lowest values of the extinction (NW3, NW4, NW5 and SE3) the correlation is linear.
- The regions with high values of the extinction (NW1, NW2, SE1 and SE2) show a clear deviation from the linearity.
- In all the cases, these correlations are closer to the linearity for $R_V = 5.45$.
- The correlations including the extinction based on the line-ratio $H\alpha/H\beta$ has a high dispersion.
- In general, we found that $A^{P\beta/H\alpha} > A^{P\beta/H\beta} > A^{H\alpha/H\beta}$.

Regions	RA (J2000)	DEC (J2000)	R_x	R_y	PA (deg)
NW-1	12:15:39.060	+36:19:36.93	1.92393”	1.92393”	165
NW-2	12:15:39.317	+36:19:33.25	1.92393”	1.92393”	165
NW-3	12:15:39.823	+36:19:36.22	1.79567”	3.7196”	185
NW-4	12:15:40.109	+36:19:30.24	1.79567”	1.79567”	165
NW-5	12:15:40.620	+36:19:30.96	3.33482”	1.41088”	170
SE-1	12:15:40.778	+36:19:09.43	1.79567”	1.79567”	165
SE-2	12:15:40.922	+36:19:03.93	2.95003”	3.7196”	165
SE-3	12:15:40.922	+36:19:03.93	2.95003”	3.7196”	165

Table 2.5: Apertures used to determine the photo-ionised regions.

Ideally, if our dust properties and the assumed dust geometry were correct, we would expect perfect agreement between different measurements of the extinction. We found that the agreement is better for the case of $R_V = 5.45$, which could indicate that this extinction curve describes dust properties better. The lack of a complete agreement between the extinction measured through different line-ratios must be due then to the fact that the foreground dust screen is not a perfect description of the actual dust geometry.

Alternative geometrical scenarios were studied by Caplan and Deharveng (1986) and Calzetti

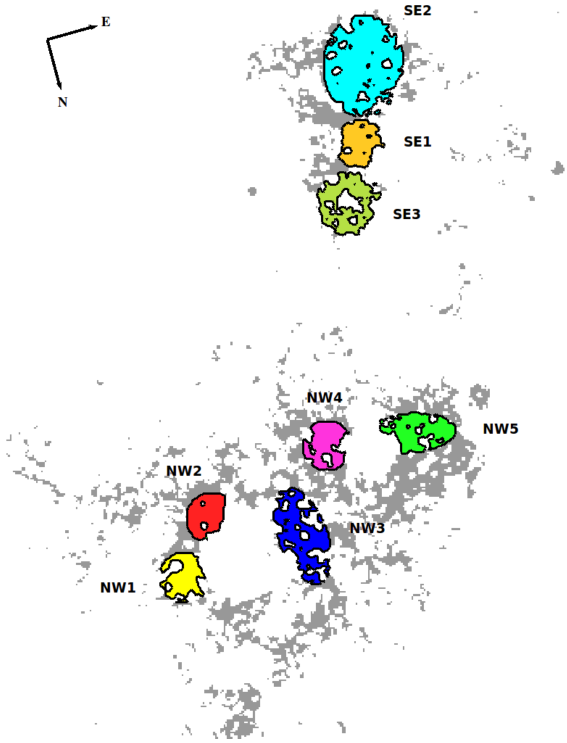

Figure 2.6: Mask used to isolate the photo-ionised regions of NGC 4214. The coloured areas correspond to the intersection between the elliptical apertures presented in Table 2.5 and the error mask (in grey).

et al. (1994) among other authors. The different configurations of dust described in their papers are shown in Figure 2.11. These five simplified models do not represent an exhaustive list of all the possible dust configurations but represent extreme cases that probably bracket most of the real cases. Real galaxies show a complex distribution of dust, from dust mixed with the ionised gas, to dust organised in clumps in the PDR as well as a diffuse dust component that occupies most of the volume of galactic disk. For each of these different dust distributions, the formulation needed to calculate the extinction changes and includes parameters as the number of clumps in the line of sight, the albedo of the dust grain or the scattering phase function.

These five models encompass different configurations that describe different physical situations inside a galaxy. Calzetti et al. (1994) discuss how the different models changes the formulation needed to calculate the extinction. In the following, we give a brief summary of their description:

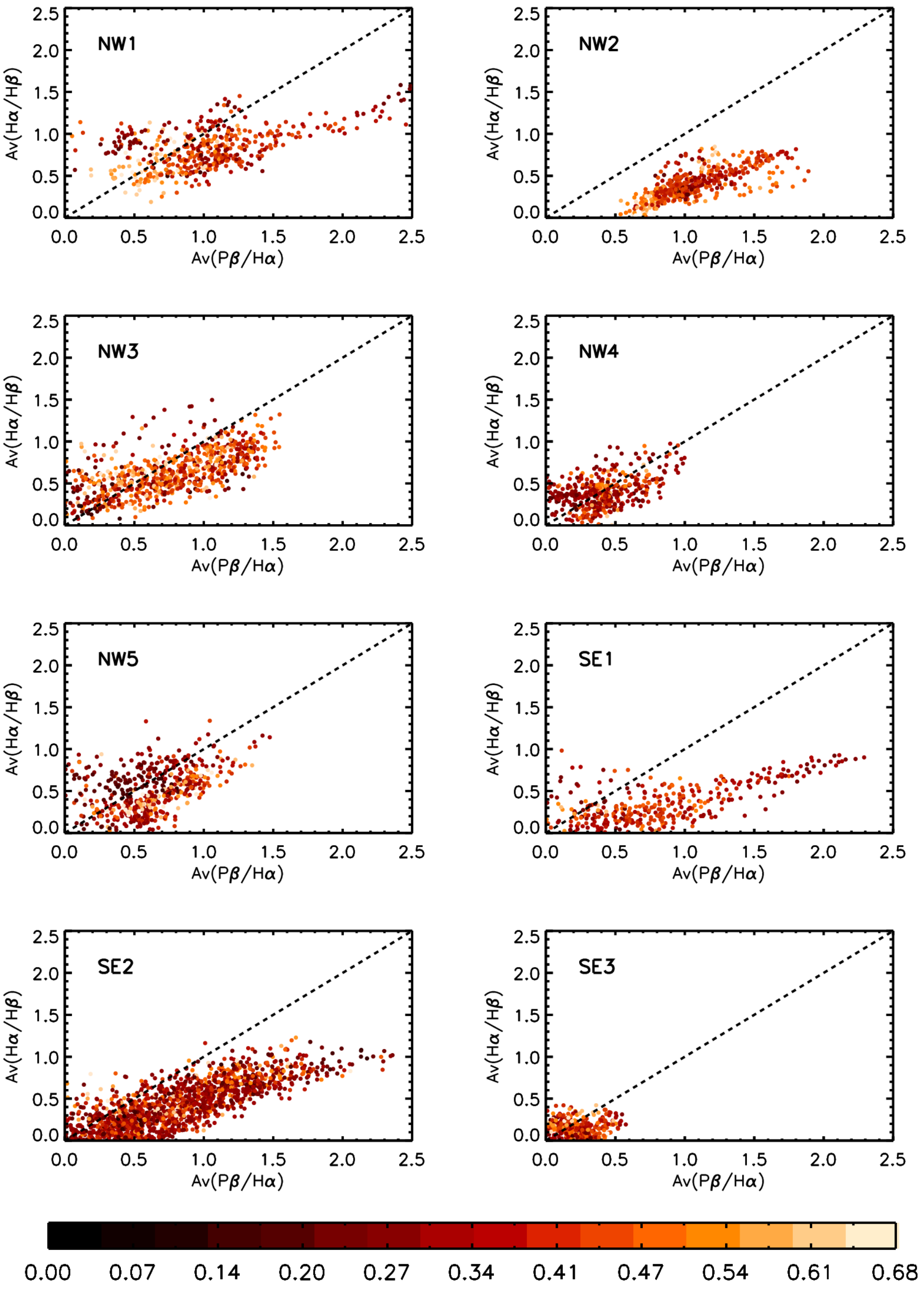

Figure 2.7: Plots pixel-by-pixel of $A^{P\beta/H\alpha}$ vs. $A^{H\alpha/H\beta}$ (in magnitudes) measured for $R_V = 3.10$ in the photo-ionized regions shown in Figure 2.6. The colour bar corresponds to the error (Δmag/pix) of the $A^{H\alpha/H\beta}$ map. The dashed line corresponds to x = y.

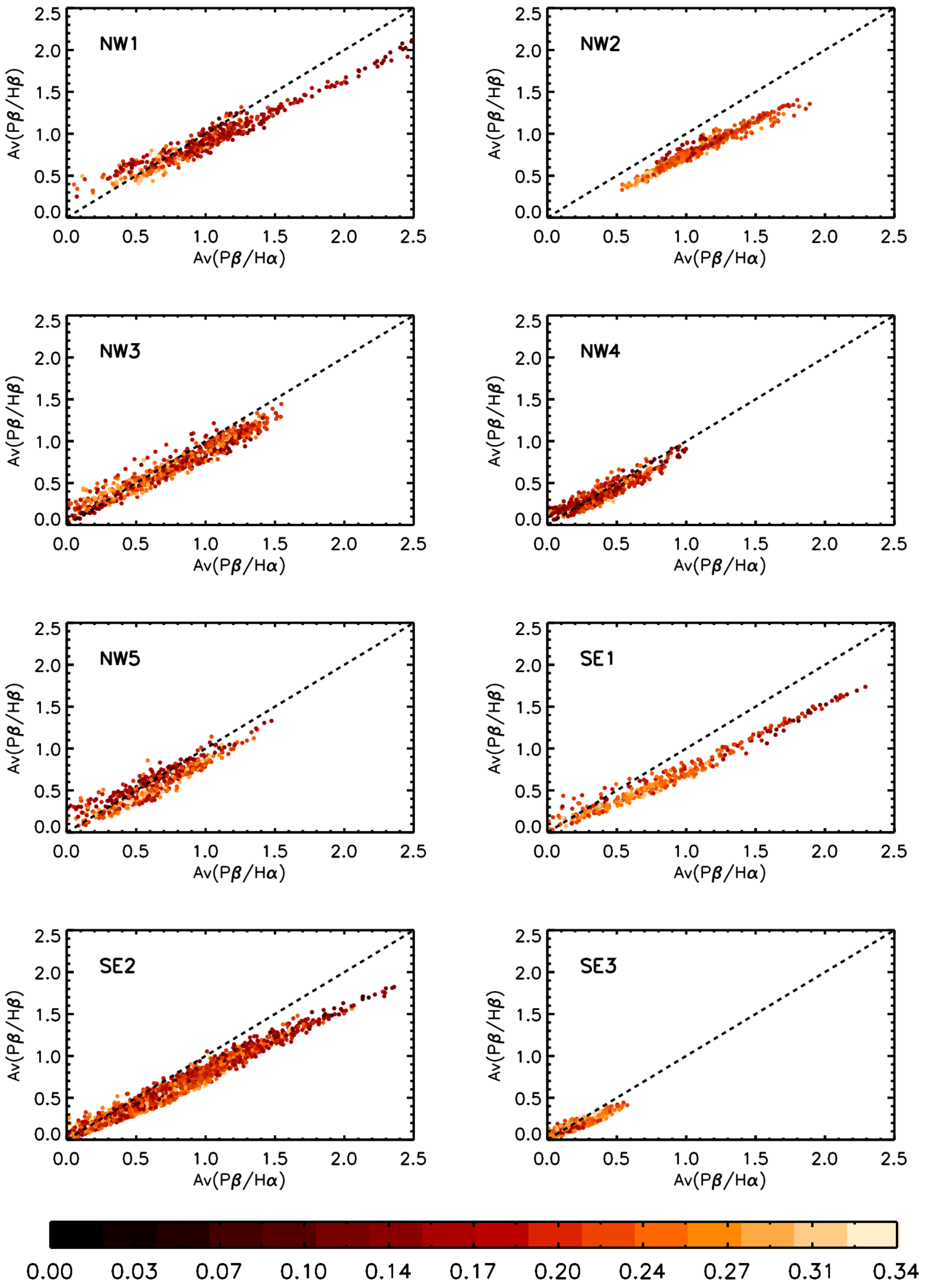

Figure 2.8: Plots pixel-by-pixel of $A^{P\beta/H\alpha}$ vs. $A^{P\beta/H\beta}$ (in magnitudes) measured for $R_V = 3.10$ in the photo-ionized regions shown in Figure 2.6. The colour bar corresponds to the error (Δmag/pix) of the $A^{P\beta/H\beta}$ map. The dashed line corresponds to x = y.

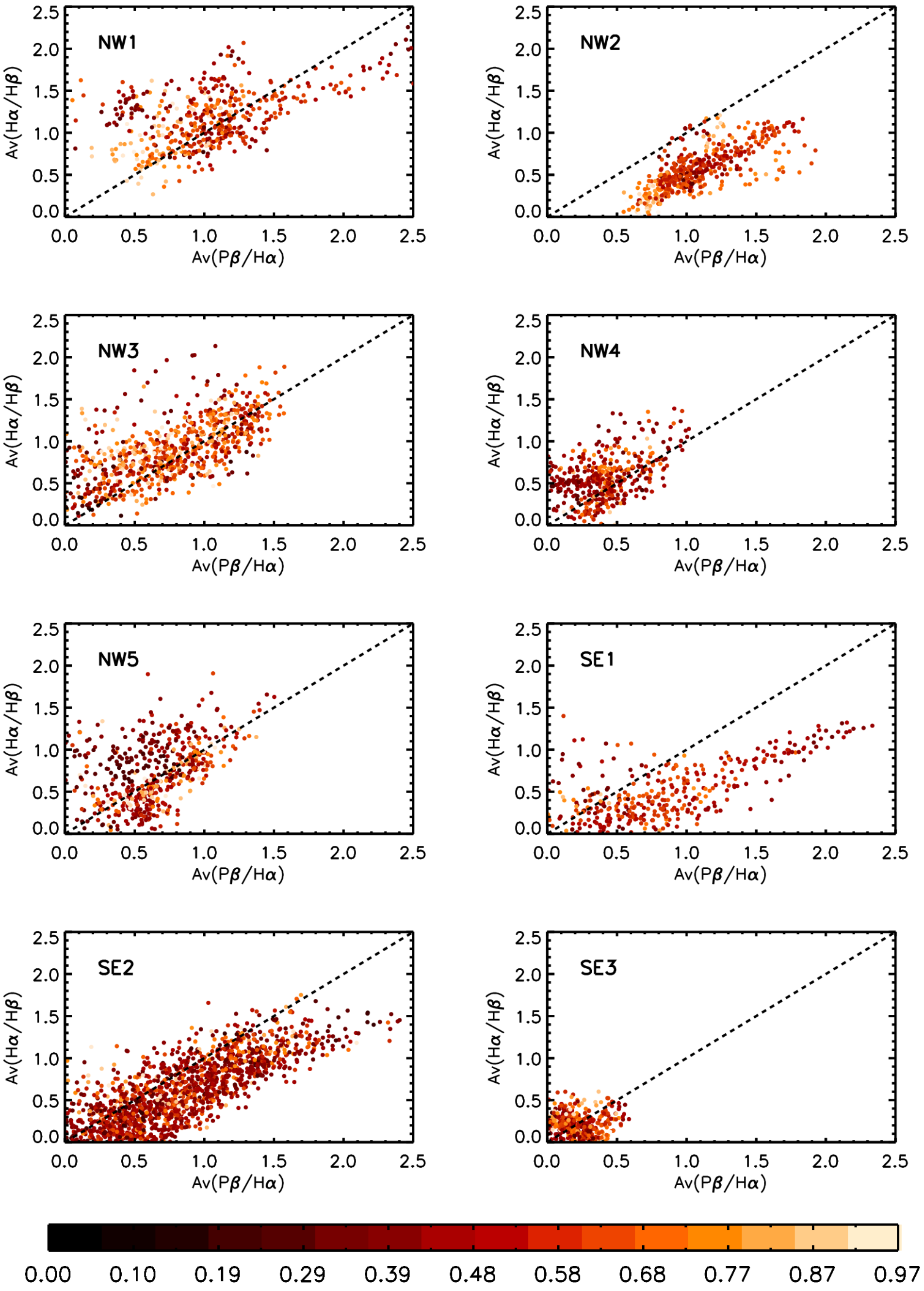

Figure 2.9: Plots pixel-by-pixel of $A^{P\beta/H\alpha}$ vs. $A^{H\alpha/H\beta}$ (in magnitudes) measured for $R_V = 5.45$ in the photo-ionized regions shown in Figure 2.6. The colour bar corresponds to the error (Δmag/pix) of the $A^{H\alpha/H\beta}$ map. The dashed line corresponds to x = y.

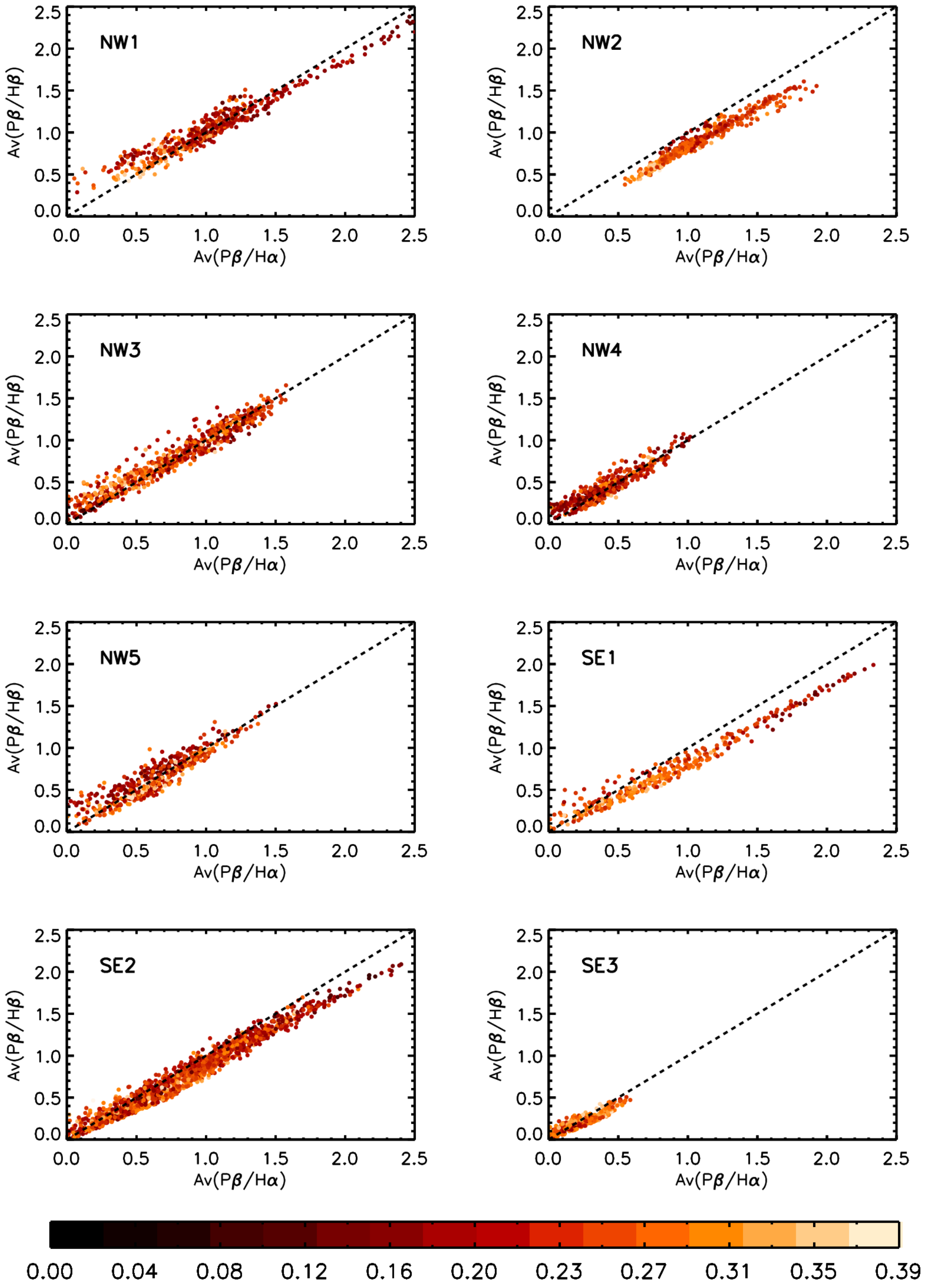

Figure 2.10: Plots pixel-by-pixel of $A^{P\beta/H\alpha}$ vs. $A^{P\beta/H\beta}$ (in magnitudes) measured for R_V = 5.45 in the photo-ionized regions shown in Figure 2.6. The colour bar corresponds to the error (Δmag/pix) of the $A^{P\beta/H\beta}$ map. The dashed line corresponds to x = y.

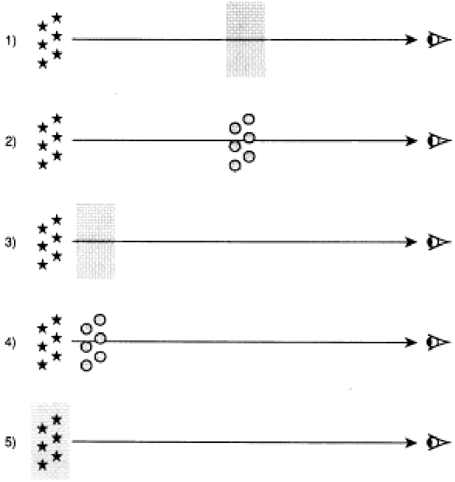

Figure 2.11: Original figure presented by Calzetti et al. (1994) illustrating different geometrical scenarios of dust and gas. From top to bottom the models are: uniform dust screen (1), clumpy dust screen (2) uniform scattering slab (3), clumpy scattering slab (4), and internal dust (5).

1. In the *uniform dust screen* model the dust screen is located physically distant from the cloud of ionised gas. This is the model used in our work to derive the value of the extinction for the observed line-ratio. In this configuration, the effect of the dust is to remove photons from the line of sight via absorption and scattering. In this case, as we have already shown in Equation 1.8, the relation of the observed and the intrinsic fluxes and the extinction for a certain wavelength λ is:

$$\mathrm{I}(\lambda) = \mathrm{I}_0(\lambda)\, 10^{-\mathrm{A}_\lambda/2.5} = \mathrm{I}_0(\lambda)\, \mathrm{e}^{-\tau_\lambda} \tag{2.28}$$

2. In the *clumpy dust screen* model the dust is also distant from the source of radiation but in this case, the dust is organised in clumps. If the observations of Hα and Hβ cover a large number of clumps, the total emission is dominated by regions with small extinction, so that the extinction derived from the Balmer ratio is expected to be biased to low values. The clumpy distribution of the dust can be parametrised in terms of the opacity of the clumps, $\tau^{\mathrm{c}}_{\lambda}$, and the number of clumps in the line of sight, $\mathcal{N}$. For this configuration, the extinction can be calculated as:

$$\mathrm{I}(\lambda) = \mathrm{I}_0(\lambda)\, \mathrm{e}^{-\mathcal{N}\left(1-\mathrm{e}^{-\tau^{\mathrm{c}}_{\lambda}}\right)} \tag{2.29}$$

3. In the *uniform scattering slab* model the dust is uniformly distributed similar to case (1), but in this case, it is located close to the source of radiation. Due to the this, the dust screen the emitting region subtends a large angle centred on the dust grains, so that the scattering by the dust grains not only removes photons from the line of sight but also bring photons back into it; i.e., scattering can provide a positive contribution to the emerging radiation. Thus, the scattering dust properties of the dust grains (the albedo, ω_λ, and the scattering phase function, g_λ) have to be taken into account as a function of the wavelength.

   In this case, the extinction can be calculated as:

   $$\mathrm{I}(\lambda) = \mathrm{I}_0(\lambda)\, e^{\alpha_\lambda^{\mathrm{eff}}\tau_\lambda} \tag{2.30}$$

   where

   $$\alpha_\lambda^{\mathrm{eff}} = h_\lambda \sqrt{1-\omega_\lambda} + (1-h_\lambda)(1-\omega_\lambda) \tag{2.31}$$

   being h_λ a function that depends on g_λ and the angle of scattering.

4. The *clumpy scattering slab* model is equivalent to the previous model but the dust is organised in clumps located close to the source. This model includes the properties of the clumpy dust screen and of the uniform scattering slab and therefore, the extinction can be calculated by combining Equations 2.29 and 2.30.

5. In the *internal dust* model the dust and the ionised gas are uniformly mixed. In this model, scattering is effective in bringing back photons into the line of sight. The extinction in this model can be calculated as:

   $$\mathrm{I}(\lambda) = \mathrm{I}_0(\lambda)\, \frac{1 - e^{-\alpha_\lambda^{\mathrm{eff}}\tau_\lambda}}{\alpha_\lambda^{\mathrm{eff}}\tau_\lambda} \tag{2.32}$$

   In this case the optical depth measured from line-ratios has an upper limit. In the case of the extinction derived from the Balmer decrement, the optical depth at the Hβ wavelength reaches a maximum value of $\sim 0.2 - 0.3$ (see Figure 11 in Calzetti et al. 1994).

Our observations show (Figures 2.7 to 2.10) that in our case the uniform dust screen model can not fully explain the trend of the pixel-by-pixel plots. By comparing the predictions of the different models to our observations we can draw the following conclusions:

- From the trend of the pixel-by-pixel plots, it seems clear that a positive contribution of scattered photons is necessary to account for the deviations from linearity observed at high extinctions. The albedo of the dust grains has its maximum near Hβ. Under these conditions, one would expect that more Hβ photons are conveyed back to the line of sight than Hα photons, and thus, the "excess" of scattered Hβ photons into our line sight would have the effect of decreasing the extinction obtained with the Hβ line (i.e., $A^{H\alpha/H\beta}$ and $A^{P\beta/H\beta}$). This effect is precisely what the pixel-by-pixel plots show in those photo-ionised regions where the extinction reaches high values.

- As we have already mentioned in the discussion of the clumpy dust screen model, the extinction measured with Hα/Hβ might be biased towards lower values of the extinction. This effect would be not present in the extinction maps based on line-ratios that includes Pβ since the extinction at this wavelength is very small. Under these conditions, one would expect that $A^{H\alpha/H\beta} < A^{P\beta/H\alpha} = A^{P\beta/H\beta}$. Thus, this model is not able in predicting why we obtain $A^{H\alpha/H\beta} < A^{P\beta/H\beta} < A^{P\beta/H\alpha}$.

The uniform scattering slab, the clumpy scattering slab and the internal dust models proposed by Calzetti et al. 1994 provide a positive contribution of scattered photons. Due to the existence of values of the extinction much greater than the maximum value allowed, it is clear that the internal dust model is not able to explain by itself the extinction measured in the photo-ionised regions of NGC 4214, and therefore, the positive contribution of scattered photons might be due to an uniform or clumpy scattering slab. However, the distribution of the extinction shown in Figure 2.4 seems to favour the hypothesis of dust organised in clumps enveloping the ionised gas, as it would correspond to dust within a fragmented PDR.

2.3.3 Intrinsic Hα emission

We can now use the derived extinction map to correct the Hα emission and obtain an intrinsic (i.e., extinction-corrected) map of Hα. We carry out the extinction correction based on the $A_{V,5.45}^{P\beta/H\alpha}$ map, since this map is less affected by uncertainties in the the value of R_V (Section 2.3.1) and it is less sensitive to a positive contribution of scattered photons (Section 2.3.2). Besides, since Pβ suffers only little extinction, this map is the most reliable tracer of the extinction.

From the Cardelli et al. (1989) extinction law with $R_V = 5.45$, we convert the extinction map $A_{V,5.45}^{P\beta/H\alpha}$ (in magnitudes in the V-band) into $A_{H\alpha,5.45}^{P\beta/H\alpha}$ (magnitudes at the Hα wavelength), as:

$$A_{H\alpha,5.45}^{P\beta/H\alpha} = 0.857 \times A_{V,5.45}^{P\beta/H\alpha} \tag{2.33}$$

From Equations 1.8 and 2.33, we can calculate intrinsic Hα line emission as:

$$\mathrm{I}^{0}_{\mathrm{H}\alpha} = \mathrm{I}_{\mathrm{H}\alpha} \times 10^{-0.4\times0.857\times\mathrm{A}^{\mathrm{P}\beta/\mathrm{H}\alpha}_{\mathrm{V},5.45}} \tag{2.34}$$

This last equation is based for consistency, equally as the calculation of the extinction, on a foreground dust screen. In Figure 2.12 the observed (left) and the intrinsic (right) Hα emission maps are compared. The most remarkable difference between these two maps comes from the shell structure within the NW regions, whose morphology is reinforced in the intrinsic map. Besides, the knot NW-1, barely noticeable in the observed map, is the second brightest structure in the intrinsic image. Regarding to the SE region, most of its knots, with the exception of the knot located closer to the NW region, appear brighter in the intrinsic map.

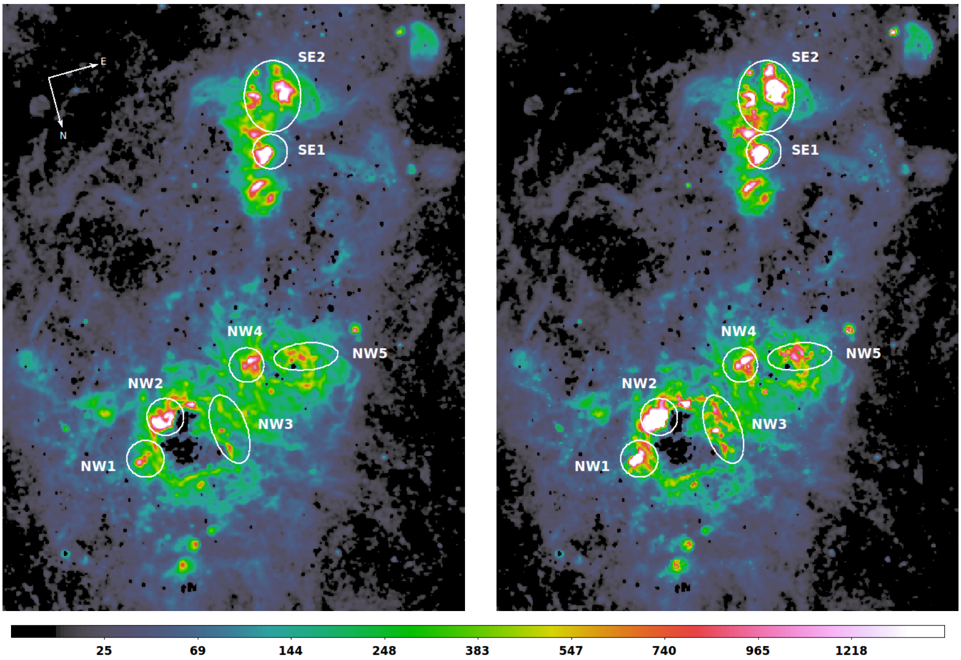

Figure 2.12: Observed (left) and intrinsic (right) Hα emission of NGC 4214. The units are $10^{-18}\,\mathrm{erg\,s^{-1}\,cm^{-2}}$.

We extracted the photometry of the knots using the apertures presented in Table 2.5. Besides, in order to obtain the total fluxes for the SF regions, we also performed the photometry over two circular apertures that enclose NW and SE, as well as the entire FoV of the HST. The results are shown in Table 2.6.

Region	$I_{H\alpha}$ [ergs s^{-1} cm^{-2}]	$< A_{H\alpha} >$	$I^0_{H\alpha}$ [ergs s^{-1} cm^{-2}]
NW	5.876×10^{-12}	0.441	7.261×10^{-12}
NW1	0.193×10^{-12}	0.886	0.427×10^{-12}
NW2	0.380×10^{-12}	0.935	0.823×10^{-12}
NW3	0.266×10^{-12}	0.662	0.430×10^{-12}
NW4	0.238×10^{-12}	0.362	0.319×10^{-12}
NW5	0.241×10^{-12}	0.545	0.348×10^{-12}
SE	2.304×10^{-12}	0.578	3.602×10^{-12}
SE1	0.319×10^{-12}	0.750	0.752×10^{-12}
SE2	0.720×10^{-12}	0.731	1.472×10^{-12}
HST FoV	15.733×10^{-12}	0.469	18.519×10^{-12}

Table 2.6: Observed Hα intensity, $I_{H\alpha}$, average extinction, $< A_{H\alpha} >$, and intrinsic Hα intensity, $I^0_{H\alpha}$, measured in the small apertures around photo-ionised regions, in the apertures enclosing the NW and SE complexes and the FoV of the HST.

2.3.4 Comparison with the dust emission

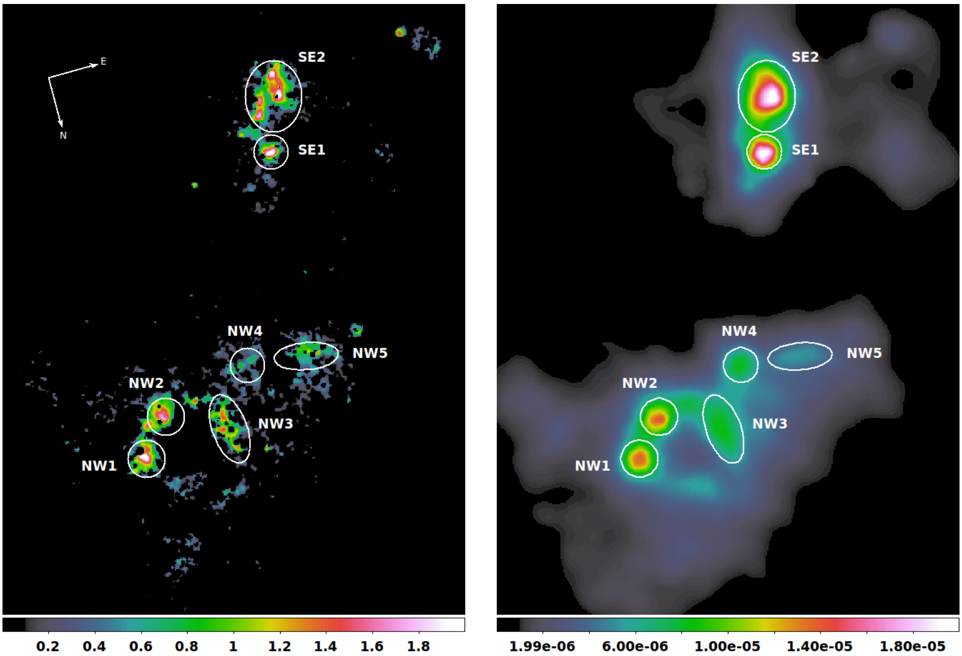

Figure 2.13: Dust extinction map (left) and dust emission mapped with the IRAC 8 μm camera (right) of the star forming complexes of NGC 4214. The units are magnitudes and Jy for dust extinction and dust emission, respectively.

In Figure 2.13 we compare the dust extinction to the dust emission at 8 μm. The IRAC 8 μm map has the highest spatial resolution of all dust emission map ($\sim 2''$), but is still almost one order of magnitude lower than the resolution of the extinction map. We found in general a good correlation between the dust extinction and the dust emission. The higher resolution allows to reveal a clumpy structure of the dust distribution which is not visible in the smoother IRAC 8 μm map. For example, in the SE2 knot, it is possible to distinguish four different dust clumps in the extinction map that appear like one only big knot in the emission map.

CHAPTER 3

Radiative transfer models

"All models are wrong, but some are useful."

– George Edward Pelham Box (1979)

In order to interpret the dust SED of a galaxy and to understand the differences in the SEDs of dwarf galaxies, a physical model based on realistic dust properties and taking into account the heating and emission of dust immersed in a wide range of interstellar radiation fields (ISRFs) is needed. Ideally, radiation transport in a realistic geometry should be done, but this is often difficult due to the complex geometry and large number of parameters. Models can generally be classified into three broad groups: (1) modified blackbody fits, which are too simple to describe reality correctly but give a first idea of the dust temperature ranges, (2) semi-empirical models that try, in a simplified way, to describe dust immersed in a range of different ISRFs (e.g. Dale et al. 2001, Draine et al. 2007, Galametz et al. 2009, 2011, da Cunha et al. 2008, Natale et al. 2010) and (3) models that include full radiation transfer (e.g. Popescu et al. 2011 for spiral galaxies, Siebenmorgen and Krügel 2007 for starburst galaxies, see also Silva et al. 1998, Popescu et al. 2000, Popescu et al. 2004, Misiriotis et al. 2001, Bianchi 2008, Baes et al. 2010, 2011 and MacLachlan et al. 2011), which are the most precise description of a galaxy if all parameters, including the geometry, are known.

The new IR facilities with their high angular resolution and sensitivity and complete coverage of the dust SED allow for the first time a detailed comparison between models and data. For nearby, and thus spatially resolved galaxies the spatial variations of the dust SED can be probed and modelled. In particular, a good spatial resolution allows us to separate and treat independently the emission from dust heated by the UV radiation of massive stars in HII regions and their adjacent photo dissociation regions (PDR) and the diffuse dust heated by the general ISRF. The dust temperature and the SED of its emission are completely different for both components and therefore the models can be better constrained if they are applied to each component separately.

In star forming galaxies, interstellar dust is present in the sites of formation of the stars as well as in the diffuse component that fills most of the volume of the galaxy. Since the dust grains in these two components are exposed to very different radiation fields, their physical properties (temperature, ionization, chemical composition) are different and they must be analyzed separately.

We compare the data for the diffuse dust to the model library of the dust emission from disk galaxies from Popescu et al. (2011) and the dust emission associated with the star forming complexes to the models of dust in HII+PDR region by Groves et al. (2008). In the following, a detailed description of both models is given.

3.1 The model of Popescu et al. (2011)

Popescu et al. (2011) presented a self-consistent model based on full radiative transfer calculations of the propagation of starlight in disk galaxies. The optical properties of the grains, the chemical composition and the grain size distribution are taken from Weingartner and Draine (2001) and Draine and Li (2007) dust models, which incorporate a mixture of silicate, graphite and PAH molecules.

In Popescu et al. (2011) model the large scale distribution of stars and dust are approximated as continuous spatial functions of stellar emissivity, η, and a dust extinction coefficient, $\kappa_{\rm ext}$. More specifically, the model has three separate components:

i) The **old component**, that consists of an old stellar disk, an old stellar bulge and a dust disk, whose spatial distributions are respectively approximated as:

$$\eta^{\rm disk}(\lambda, {\rm R}, {\rm z}) = \eta^{\rm disk}(\lambda, 0, 0) \exp\left(-\frac{\rm R}{\rm h_s^{disk}} - \frac{\rm z}{\rm z_s^{disk}}\right) \tag{3.1}$$

$$\eta^{bulge}(\lambda, R, z) = \eta^{bulge}(\lambda, 0, 0) \times B^{-7/8} \times \exp\left(-7.67B^{1/4}\right) \tag{3.2}$$

$$\kappa_{ext}^{disk}(\lambda, R, z) = \kappa_{ext}^{disk}(\lambda, 0, 0) \exp\left(-\frac{R}{h_d^{disk}} - \frac{z}{z_d^{disk}}\right) \tag{3.3}$$

The superscripts *disk* and *bulge* are used to distinguish the two different stellar distributions of the old component. The subscripts s and d denote whether the scale-length, h, and the scale-height, z, are referred to the stellar disk (s) or to the its associated disk of dust (d). The dust disk associated with the old stellar component is referred to as *thick disk of dust*.

ii) The **young component**, that consists of a young stellar disk and a dust disk, whose spatial distributions are respectively approximated as:

$$\eta^{tdisk}(\lambda, R, z) = \eta^{tdisk}(\lambda, 0, 0) exp\left(-\frac{R}{h_s^{tdisk}} - \frac{z}{z_s^{tdisk}}\right) \tag{3.4}$$

$$\kappa_{ext}^{tdisk}(\lambda, R, z) = \kappa_{ext}^{tdisk}(\lambda, 0, 0) exp\left(-\frac{R}{h_d^{tdisk}} - \frac{z}{z_d^{tdisk}}\right) \tag{3.5}$$

In this case the superscript *tdisk* denotes that these distributions are related with the young stellar disk and its associated disk of dust, which is also referred to as the *thin disk of dust*. The young component is introduced to mimic the more complex distribution of young stars and diffuse dust associated with the spiral arms.

iii) The **clumpy component**, consisting of the parent molecular clouds of massive stars.

In Figure 3.1 a schematic representation of the components assumed in Popescu et al. (2011) model is shown.

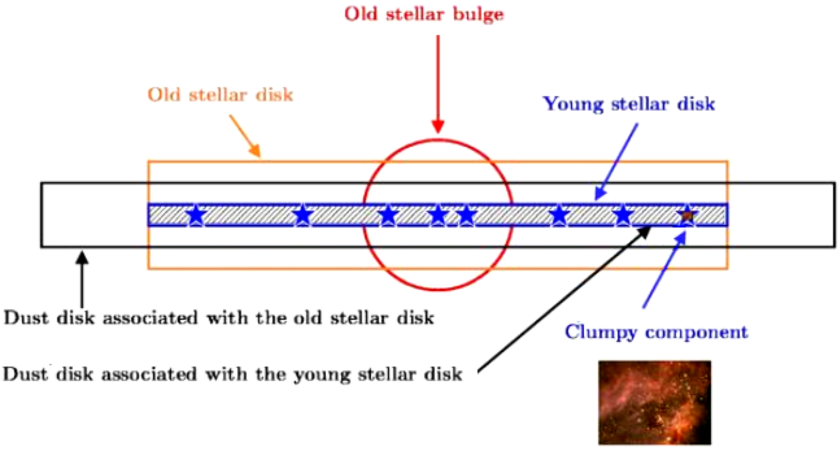

Figure 3.1: Adaptation of the original figure presented in Popescu et al. (2011) with an schematic representation of the geometrical distributions of stellar and dust components in Popescu et al. (2011) model.

In the Popescu et al. (2011) model the geometry of the old stellar disk and of the thick dust disk are empirically constrained from resolved optical and near-IR images via the results of the modelling procedure of Xilouris et al. (1999). Unlike the old component, the geometry of the young stellar population has not been constrained due to the high obscuration suffered by the stellar light in this case. The scale-length of the young stellar disk was taken to be 90 pc (the value of the the Milky way) and its scale-length was set equal to that of the B-band scale-height of the old stellar disk. The thin disk of dust was fixed to have the same scale-length and the same scale-height as the young stellar disk.

All the scale-lengths and scale-heights corresponding to both young and old components of stars and dust are expressed in terms of the B-band scale-length of the old stellar disk. Fixing the geometry in terms of $\mathrm{h_s^{disk}(B)}$ minimizes the number of parameters of the model but makes the model not flexible to changes in the geometry.

The extinction coefficient of the thin disk and of the thick disk are parametrized in terms of their corresponding B-band face-on opacities $\tau_B^{f,tdisk}$ and $\tau_B^{f,disk}$. To minimise the number of free parameters both opacities are assumed to have a constant ratio $\tau_B^{f,disk}/\tau_B^{f,tdisk}$ of 0.387.

In order to parametrise the intensity of the ISRF to which the dust is exposed, the Popescu et al. (2011) model introduces the parameters *SFR*, describing the radiation fields produced by the young stellar disk, *old*, by the old stellar disk, and *B/D*, by the bulge. These parameters are linked to observable quantities as the luminosity of the young stellar disk, L^{tdisk}, the luminosity of the old stellar disk, $\mathrm{L^{disk}}$, and the luminosity of the bulge, L^{bulge}, by the following equations:

$$\mathrm{SFR} = \frac{\mathrm{L^{tdisk}}}{\mathrm{L^{young}_{unit}}} \tag{3.6}$$

$$\mathrm{old} = \frac{\mathrm{L^{disk}}}{\mathrm{L^{old}_{unit}}} \tag{3.7}$$

$$\mathrm{B/D} = \frac{\mathrm{L^{bulge}}}{\mathrm{old} \times \mathrm{L^{old}_{unit}}} \tag{3.8}$$

where $L_{unit}^{young} = 4.235 \times 10^{36}\,W$ is the luminosity produced by a SFR of $1\mathrm{M}_\odot\,yr^{-1}$ in the range from 912 to 50000 Å, $L_{unit}^{old} = 2.241 \times 10^{37}\,W$, corresponds to 10 times the luminosity of the non-ionising UV photons produced by a $1\mathrm{M}_\odot\,yr^{-1}$ young stellar population.

In order to parametrise the light escaping from the SF regions, the model of Popescu et al. (2011) makes use of the clumpiness factor F, which can be physically identified with the luminosity-weighted mean fraction of directions from the massive stars, averaged over the lifetime of the stars, which intersects the birth-cloud. The clumpiness factor F is linked to the fraction of photons that escapes ($f_{\rm esc}$) from the SF regions into the diffuse medium as $F = 1{-}f_{\rm esc}$.

From the primary parameters SFR and F, Popescu et al. (2011) define the star formation rate powering the diffuse emission, SFR', as it follows (Eq. 45 in Popescu et al. 2011):

$$SFR' = SFR \times (1 - F) \tag{3.9}$$

The library of diffuse SEDs of Popescu et al. (2011) contains results for a four-dimensional parameter space spanned by τ_B^f, SFR', old and B/D. The diffuse component is calculated as an extrinsic quantity corresponding to a reference size (corresponding to a reference scale-length). In order to scale the intensity of the ISRF heating the diffuse dust in a galaxy, the parameters SFR' and old must be scaled to the reference size by comparing the scale-lengths (Eq. D.3 in Popescu et al. 2011):

$$SFR^{model} = SFR' \times \left(\frac{h_s^{ref}(B)}{h_s(B)} \right)^2 \tag{3.10}$$

$$old^{model} = old \times \left(\frac{h_s^{ref}(B)}{h_s(B)} \right)^2 , \tag{3.11}$$

where $h_s^{ref}(B) = 5670\,pc$ and $h_s(B)$ are the reference B-band scale-length and the B-band scale-length of the galaxy under study, respectively. We note here that SFR^{model} and old^{model} are only internal parameters that allow us to interface with the library of models. Because of this all the results in this paper are presented only in terms of the SFR and old, the real parameters of the galaxy under study.

An additional scaling is required to set the flux levels of the SEDs from the library to the observed SED of our galaxy. Thus, the SED that represents our galaxy, F_λ^d, is determined as (Eq. D.2 in Popescu et al. 2011):

$$F_\lambda^d = \left(\frac{h_s(B)}{h_s^{ref}(B)} \right)^2 \times F_\lambda^{d,model}(B/D, \tau_B^f, SFR^{model}, old^{model}). \tag{3.12}$$

We would like to stress that in these models the absolute flux level of the predicted dust SED is fixed by the input parameters.

The models of Popescu et al. (2011) have been designed to provide the formalism for fitting the integrated emission of galaxies, since for most galaxies resolved information on the dust emission is not available. In particular dust emission SEDs of individual star-forming complexes cannot be derived in most cases. Consequently, the model of Popescu et al. (2011) provides an average template SED for the dust emission of the ensemble of the HII regions. This template has been empirically calibrated on data of a representative sample of prominent star forming complexes in our Galaxy, as fitted using the model of Groves et al. (2008). By contrast, in the case of the nearby dwarf galaxies studied in this work, we have resolved information on the star forming complexes, and can therefore replace the average template with a detailed modelling of these complexes using directly the model of Groves et al. (2008), while still retaining the general framework of the model of Popescu et al. (2011), when calculating the attenuation of stellar light in the clumpy component. This allows us to reach a self-consistent treatment of the diffuse and clumpy component, mediated by the fact that the two models used here have a common parameter, the F factor.

3.2 The model of Groves et al. (2008)

The model of Groves et al. (2008) describes the dust emission from the HII region and the surrounding PDR (see Figure 3.2) via radiation transfer calculations. In this model the HII regions are treated as one-dimensional mass-loss bubbles driven by the mechanical energy input of their stars and supernovae (Castor et al. 1975). The mechanical energy input, $L_{\rm mech}$, is determined from the Starburst99 output. The radius $R(t)$ of the HII region at any given time t is determined by both $L_{\rm mech}$ and the ambient pressure p_0. At any point within the HII region or its surrounding PDR, the distribution of the grain temperatures (and therefore the form of the far-IR continuum) is determined by the intensity and the SED of the stellar radiation field, which depends on the luminosity of the cluster and on the the radius of the HII region ($L_{star}/4\pi R(t)^2$). In Groves et al. (2008) model this is parametrised with the compactness parameter, $\mathcal{C}$, in the form:

$$\mathcal{C} \propto \frac{\langle L_{star} \rangle}{\langle R(t)^2 \rangle} \tag{3.13}$$

The dust model consists of three components: graphites, silicates, and PAHs. The optical data for each of these come from Laor and Draine (1993), Li and Draine (2001) , and Weingartner and Draine (2001). The IR spectrum arising from dust, excluding the effects of PAH emission, is calculated self-consistently, including the effects of stochastic heating in small grains. For the PAH emission Groves et al. (2008) have constructed an empirically based IR emission spectrum based on Spitzer-IRS observations of NGC 4676 and NGC 7252. PAHs destruction

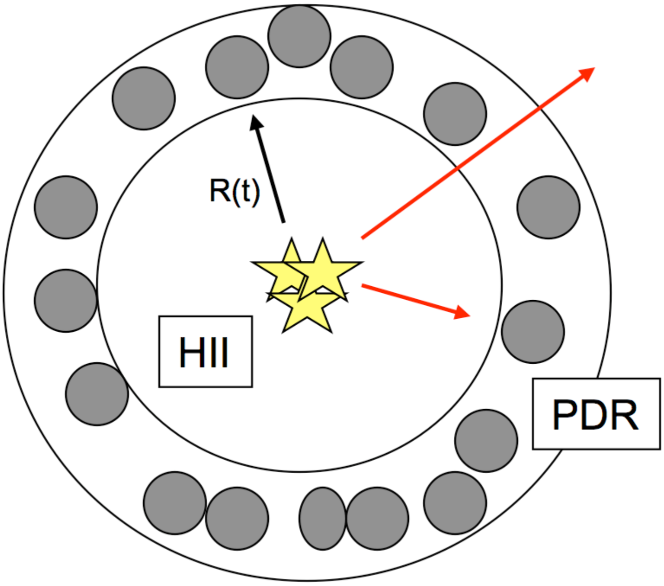

Figure 3.2: Schematic representation of the geometrical distributions of stellar and dust components in Groves et al. (2008) model.

within the ionized parts of the HII region is also taken into account. The total dust-to-gas ratio within the code is set by the fraction of metals depleted from the gas onto dust.

At a given age, the model self-consistently calculates the luminosity distribution of the star cluster and the radius of the inner edge of the PDR and computes the emergent SED for the dust in the HII region without considering the PDR, F_λ^{HII}, and for the dust from the HII region which is completely covered by a PDR, $F_\lambda^{HII+PDR}$. The total emergent SED from the star forming region which is partially covered by the PDR, F_λ^{SF}, is then given by:

$$F_\lambda^{SF} = (1 - f_{cov}) \times F_\lambda^{HII} + f_{cov} \times F_\lambda^{HII+PDR} \tag{3.14}$$

CHAPTER 4

SED modelling of dwarf galaxies

> *"You certainly usually find something, if you look,*
> *but it is not always the something you were after."*
>
> – John Ronald Reuel Tolkien (*The Hobbit*, 1937)

For our study of the SEDs of dwarf galaxies we chose the two Magellanic galaxies NGC 4214 and NGC 4449. Both objects are well above the Galactic disk and therefore, the contamination of dust from the Milky Way is negligible.

4.1 The data set

A wide range of data exists in archives for NGC 4214 and NGC 4449, from the UV to the radio. The entire dust emission SED from the Mid-IR to the submm is covered by data from Spitzer, Herschel and Planck. In addition, to extend the dust SED of NGC 4214 to the mm range we have mapped this galaxy at 1.2 mm with the IRAM 30 m telescope. In the following subsections we describe the data and the reduction that we have performed prior to extracting the photometry. A selection of images at different wavelengths is shown in Figure 4.1 and 4.2 for NGC 4214 and NGC 4449, respectively.

4.1.1 GALEX

The Galaxy Evolution Explorer (GALEX) is an orbiting space telescope led by the California Institute of Technology (CALTECH). The GALEX far-ultraviolet (FUV) detector has an ef-

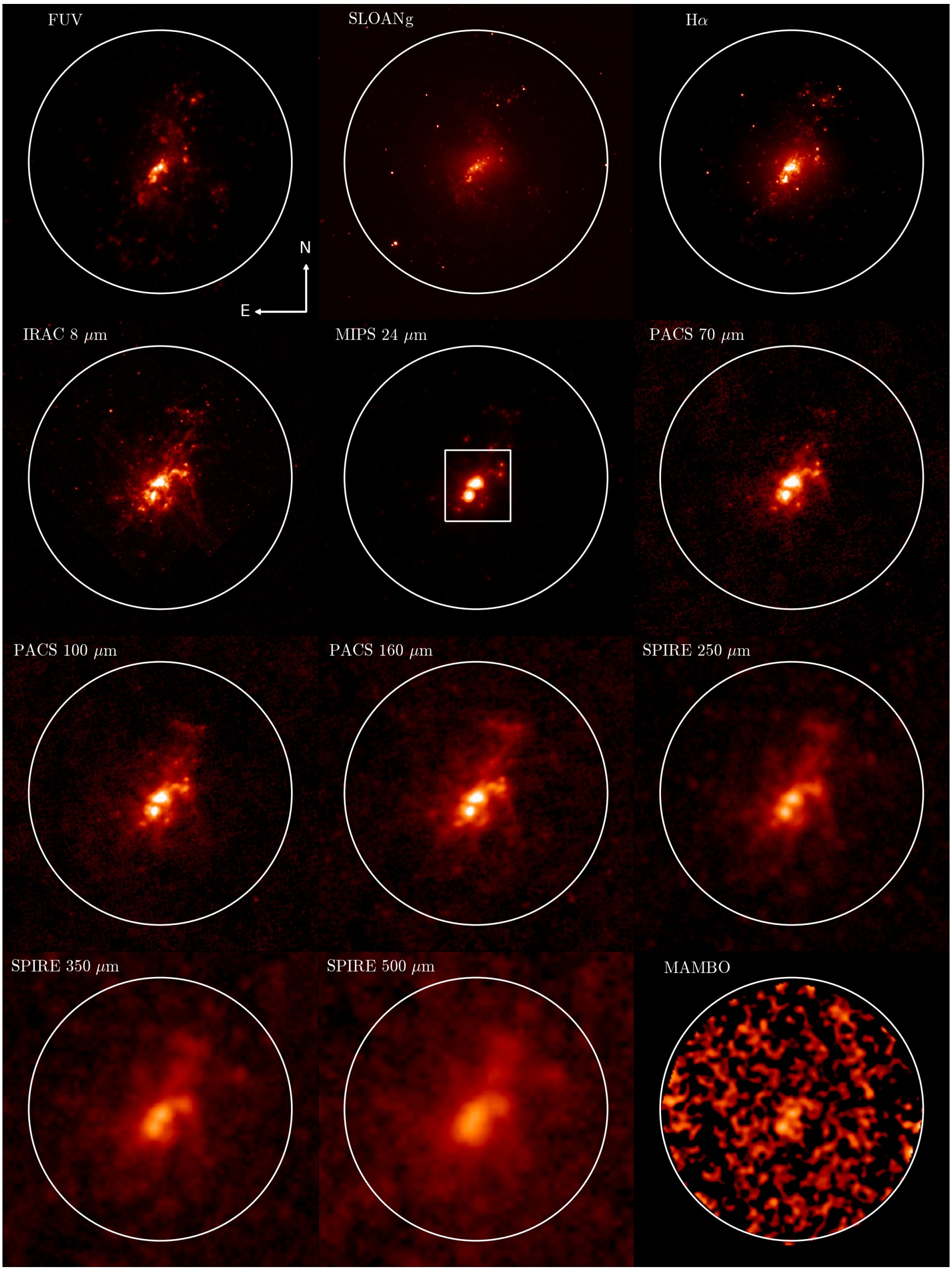

Figure 4.1: Images of NGC 4214 at different wavelengths. The large circle shows the aperture that we chose for the entire disk emission. The small box at the centre encloses the SF complexes (see left panel of Figure 4.3).

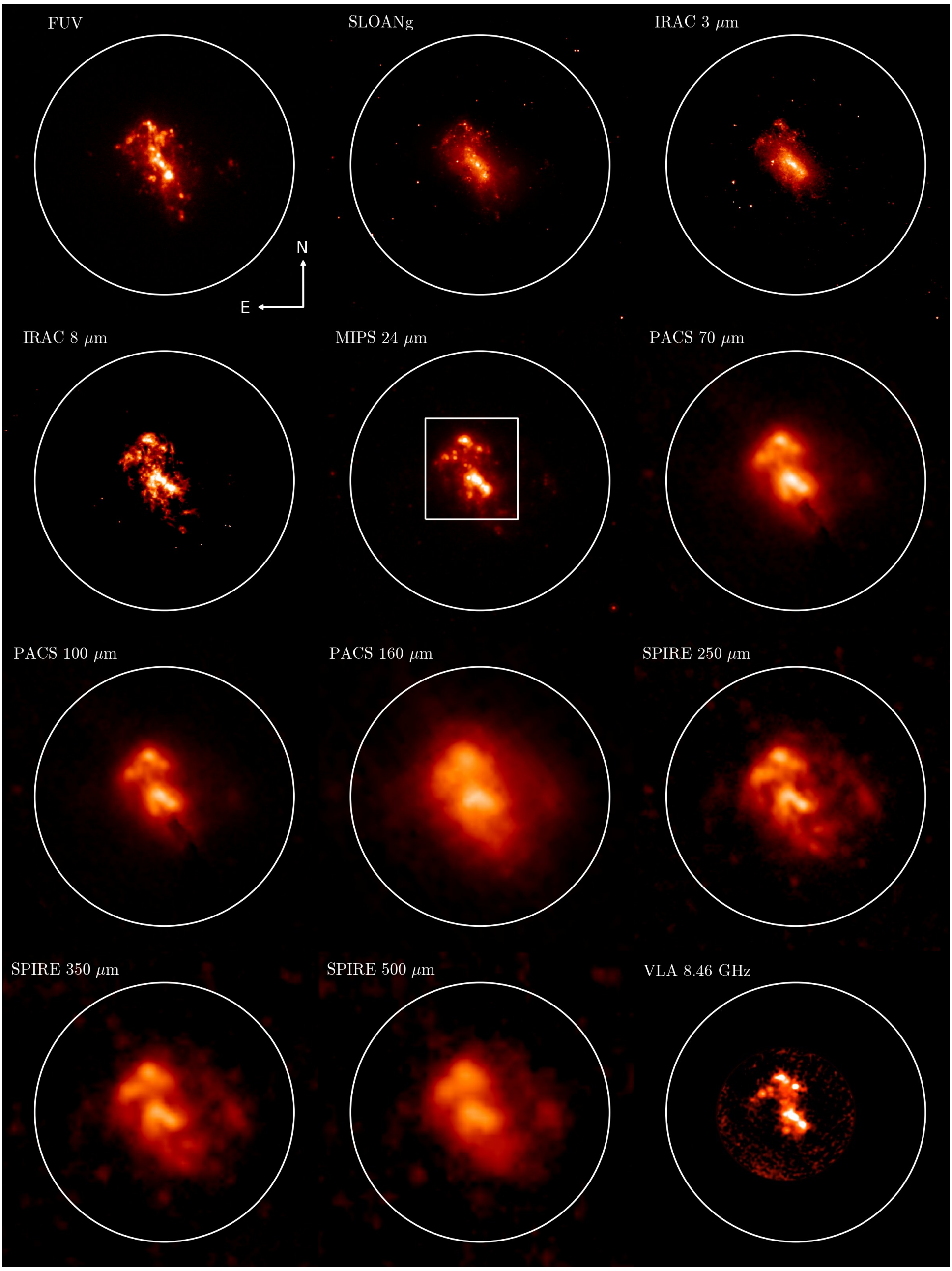

Figure 4.2: Images of NGC 4449 at different wavelengths. The large circle shows the aperture that we chose for the entire disk emission. The small box at the centre encloses the SF complexes (see right panel of Figure 4.3).

fective wavelength of 1539 Å, a bandwidth of 442 Å and an image resolution of 4.2″. For the near-ultraviolet (NUV) detector, the effective wavelength is 2316 Å, the bandwidth 1060 Å and the image resolution 5.3″.

The FUV and NUV data used in this work for NGC 4214 and NGC 4449, which traces the photo-spheric emission from O and B stars, are part of the *11 Mpc Hα UV Galaxy Survey* (11HUGS), which provides Hα and GALEX UV imaging for an approximately volume-limited sample of ~ 300 spiral and irregular star forming galaxies within a distance of 11 Mpc located outside of the plane of the Milky Way (Lee et al. 2009).

NGC 4214 and NGC 4449 were observed with GALEX the 13th of January 2010 and the 15th of May 2006, respectively. FUV and NUV photometric maps were obtained. With both detectors the main SF complexes are well resolved and the field of view, with a radius of about 36′, covers the entire disk of both galaxies (see Figures 4.1 and 4.2 for NGC 4214 and NGC 4449, respectively.)

For both galaxies, we have retrieved the calibrated maps from the archive and subtracted the background using the corresponding maps.

4.1.2 HST

HST data of NGC 4214 covering its central SF regions were obtained with the WFC3 camera. A complete description of these data was given in Sect. 2.1.

HST data of NGC 4449 were obtained with the Advanced Camera for Surveys (ACS) as part of the ACS Nearby Galaxy Survey Treasury (ANGST) program (Dalcanton et al. 2009). ANGST is a systematic survey to establish a legacy of uniform multi-colour photometry of resolved stars for a volume-limited sample of nearby galaxies. NGC 4449 was mapped with the F502N, F550M, F658N, F660N and F814W filters. We obtained the calibrated data from the archive.

4.1.3 Spitzer

The Spitzer data used in this work are part of the Local Volume Legacy (LVL) survey (Dale et al. 2009). The LVL sample contains 258 galaxies within 11 Mpc, which have been mapped with both MIPS (3 bands) and IRAC (4 bands).

For both galaxies, MIPS exposure times were 146.8, 83.8 and 16.76 seconds at 24, 70, and 160 μm, respectively. The area mapped in the three bands, approximately 16′×16′ for NGC 4214 and 12′×12′ for NGC 4449, covers the whole disk of both galaxies. We obtained the images from the archive and subtracted the background, which we determined as the mean value of an annulus located outside the disk of the galaxy.

As for several other galaxies in the LVL sample, IRAC data of NGC 4214 and NGC 4449 were taken from the ”Mid-IR Hubble Atlas of Galaxies” (Fazio and Pahre 2004). As part of this program, both galaxies were observed in May 2004 at the IRAC 3.6, 4.5, 5.8 and 8.0 μm bands. In our study of the SF regions, we only use the IRAC 3.6 μm band, which we assumed as pure stellar emission, and the IRAC 8.0 μm band. In order to isolate the dust component from the IRAC 8.0 μm we subtracted the stellar emission using the IRAC 3.6 μm image and applied the formula provided in Helou et al. (2004). In all the cases, the subtracted flux was $\lesssim$ 10%. With an angular resolution of 1.7″and 2.0″ for the IRAC 3.6 and 8.0 μm bands, respectively, the SF complexes of both galaxies are resolved into several smaller HII regions.

The total mapped area by IRAC, approximately of 13′×6′, covered the central part of the galaxies but not the total extent of the apertures used in this work to measure their total flux. Therefore, the total emission at 3.6 and 8μm that we obtain might be underestimated. However, judging from the IRAC 8.0 μm images in Figures 4.1 and 4.2, the area mapped seems to contain most of the extended emission at these two bands and therefore we believe that the underestimate is not significant.

The uncertainty in the flux calibration is better than 10% for all IRAC (Reach et al. 2005, Fazio et al. 2004) and MIPS 24 μm bands (Engelbracht et al. 2007), and is better than 20% for MIPS 70 and 160 μm bands (Rieke et al. 2004). We adopt these numbers as the calibration uncertainties in our error estimates for the fluxes (see Sect. 4.2.5).

4.1.4 Herschel

NGC 4214 and NGC 4449 were observed by Herschel’s PACS and SPIRE instruments as part of the Dwarf Galaxy Survey programme (PI. S. Madden), a guaranteed time key program with the aim of mapping the dust and gas in 51 nearby dwarf galaxies.

SPIRE data of NGC 4449 were obtained the 13th of June 2011 and cover a circular area of approximately 14′. NGC 4214 was observed the 26th of the same month and the the data cover a circular area of approximately 17′. We retrieved the HIPE Level 2.0 images from the archive and performed further analysis for our purposes. Due to their good quality and absence of artefacts, we only subtracted the background which we measured in the same annulus used for MIPS data. The resolution of the images is 18″, 25″ and 37″ at SPIRE 250, 350 and 500 μm bands, respectively. Swinyard et al. (2010) reported for SPIRE 250, 350 and 500 μm bands an uncertainty in the flux calibration of 15%, which we adopted in our error calculation.

PACS data of NGC 4214 were obtained the 27th and 28th of December 2011 and cover an area of ~25′×25′. The data from the archive were processed to level 1 with HIPE 8.2.0. To complete the reduction we used the Scanamorphos (Roussel, 2012) map making technique. The background was subtracted from the final maps using the same annulus mentioned before. The resolution of PACS at 70, 100 and 160 μm is 5.2″, 7.7″ and 12″, respectively. The uncertainty in the flux calibration is of the order of 10%. In the case of NGC 4449, no public data from PACS is available.

4.1.5 Planck

The ”PLANCK Early Release Compact Source Catalogue” includes detections of NGC 4214 and of NGC 4449 at 350, 550 and 850 μm, all of them composed of two different observations. For the three detections the subtracted Cosmic Microwave Background (CMB) flux was less than 30% of the total flux measured originally by PLANCK. The catalogue gives two estimates for the total flux of a source: i) FLUX, obtained by aperture photometry within the nominal sky-averaged FWHM, which is 4.45′, 4.71′ and 4.62′ for 350, 550 and 850 μm, respectively, and ii) FLUXDET, obtained by their native detection algorithm (Planck Collaboration et al., 2011b). We adopt here the first flux estimate, FLUX, which is recommended for sources that are point-like with respect to the PLANCK beam, as is the case for NGC 4214 and NGC 4449. We use the difference between the two estimates (which is larger than the nominal error of each flux) as an estimate of the errors.

4.1.6 IRAM 30 m

Several observations of NGC 4214 at 1200 μm were made by our group between December 2009 and November 2010 at the IRAM 30 m telescope on Pico Veleta (Spain), with the 37-channels bolometer array of the Max-Planck-Institut für Radioastronomie (MPIfR). The 37 pixels are located in a hexagonal structure with a beam-size of 10.8″ and a pixel-to-pixel separation of about 23″. The observations were done on-the-fly and they were calibrated by observations of the planet Mars and secondary calibrators. Observations were reduced and combined into an image with Robert Zylka's MOPSIC[1] pipeline in a standard manner including baseline subtraction, spike and sky noise removal. We smoothed the combined image to a resolution of 18″ in order to increase the signal-to-noise ratio. At this resolution, the two main star forming complexes are still resolved. Following Lindner et al. (2011), we adopt 30% calibration uncertainty.

---

[1] See http://www.iram.es/IRAMES/mainWiki/CookbookMopsic

NGC 4449 was observed at the IRAM 30 m telescope in December 1998 by S. Khole and the data was published in Böttner et al. (2003). The total integration time was about 8 hours and the area mapped, of $\sim 350'' \times 250''$, cover the central part of NGC 4449, including the SF regions considered in this work, but not the entire disk.

4.1.7 Thermal radio emission

Public radio data at 8.46 GHz (3.5 cm) of NGC 4449 from the Very Large Array (VLA) in New Mexico (USA) is available in the VLA Archive Survey[1]. The observations were made in 1996 but the image was reprocessed in 2007. The beam of the VLA image is $7.11''$ and the FoV, with a radius of $160''$, covers the central SF regions but not the entire disk.

The distribution of thermal fraction in NGC 4449 was derived by Chyży et al. (2000) from the distribution of the spectral index between 8.46 and 4.86 GHz. The thermal fraction at 8.46 GHz shows clear peaks at the positions of bright SF complexes of NGC 4449, with values of $\sim 80\%$. We adopted this estimation to correct by multiplying by a factor 0.8 the fluxes obtained for the SF complexes.

No public data from of thermal radio emission is available for NGC 4214. For this reason, we estimate the thermal radio emission using the Hα emission. The thermal radio emission in an HII region is proportional to the production rate of Lyman continuum photons $N_{\rm Lyc}$. Condon (1992) gives the following relation between the thermal radio emission and the extinction-corrected Hβ line flux, $F(\mathrm{H}\beta)$, which is proportional to $N_{\rm Lyc}$:

$$\frac{S_{\rm T}}{\rm mJy} \sim \frac{1}{0.28}\left(\frac{T}{10^4{\rm K}}\right)^{0.52}\left(\frac{\nu}{\rm GHz}\right)^{-0.1}\frac{F(\mathrm{H}\beta)}{10^{-12}{\rm erg\,cm^{-2}s^{-1}}}, \tag{4.1}$$

where S_T is the thermal flux density at the frequency ν for an HII region with a temperature T.

We use the measurements of the Hα emission from MacKenty et al. (2000) to calculate the expected thermal radio emission from NGC 4214 - NW and NGC 4214 - SE. They presented an Hα narrowband map of the centre of NGC 4214 obtained with the HST Wide Field and Planetary Camera (WFPC2). They used the spectroscopic values of the Balmer ratio Hα/Hβ presented by Maíz-Apellániz (2000) to correct for dust extinction and they reported intrinsic Hα fluxes of NGC 4214 - NW and NGC 4214 - SE. Assuming that the dust is well mixed with the gas, MacKenty et al. (2000) calculated extinction-corrected Hα fluxes of 12.88×10^{-12} erg cm^{-2} s^{-1} for the NGC 4214 - NW complex and 5.75×10^{-12}erg cm^{-2} s^{-1} for the NGC 4214 - SE complex.

---

[1] ©2005-2007 AUI/NRAO

For the NGC 4214 - NW region, MacKenty et al. (2000) used a circular aperture of radius 20.6″, practically identical to the aperture used in this work (see Sec. 4.2.1). For the NGC 4214 - SE region they used a smaller aperture (9.96″). We therefore multiplied their flux by a factor 1.4, corresponding to the ratio of the uncorrected Hα fluxes measured from the same image in apertures of 9.96″ and 18″, respectively. Using these extinction-corrected Hα fluxes, the intrinsic $H\alpha/H\beta$ ratio and the temperature of 10^4K reported by Kobulnicky and Skillman (1996), we obtain with Eq. 4.1 flux densities at 8.46 GHz (3.5 cm) of 13 and 8 mJy for NGC 4214 - NW and NGC 4214 - SE, respectively.

The combined prediction for the thermal radio emission of NGC 4214 - NW and NGC 4214 - SE (21 mJy) can be roughly compared with the measurement from the VLA at 8.46 GHz of 24.2±4.8 mJy given by Kepley et al. (2011) for the total radio emission, which includes synchrotron and thermal emission. From the uncorrected Hα emission, Kepley et al. (2011) estimated that the fraction of thermal emission is on average $\sim$ 0.5 (see Figure 9 in their paper). However, since these authors did not correct the Hα emission for dust attenuation, their estimation gives a lower limit of the thermal fraction. Our estimation of free-free emission (21 mJy) falls within the limits of thermal fractions of 0.5 (12.1 mJy) and 1.0 (24.2 mJy) and is thus consistent with their data. We used their limits to roughly estimate an error of the thermal radio flux of $\sim$ 30%.

4.2 Photometry

We need to separate the dust emission from the major SF complexes and the diffuse disk, in order to establish the individual SEDs of these morphological components. We therefore independently carried out aperture photometry for the SF regions and for the total emission of the entire galaxy. We determined the diffuse dust emission as the difference between the total emission and the sum of the emissions of the SF regions.

Prior to extracting the photometry, we re-gridded all the images to a common pixel size keeping the original resolution of each image. Then, corresponding aperture corrections were applied to the fluxes in each band. In this section we describe how we performed the aperture photometry, which corrections were applied and how the errors were handled.

4.2.1 Apertures

We chose the apertures around the SF regions large enough to enclose the entire localized dust emission and simultaneously tried to include as little as possible emission from the diffuse component. Mainly based on the MIPS 24μm image (see Figure 4.3), in the case of

NGC 4214 we chose circular apertures whereas in the case of NGC 4449, due to the elongated geometry of the SF complexes, we decided to use elliptical apertures.

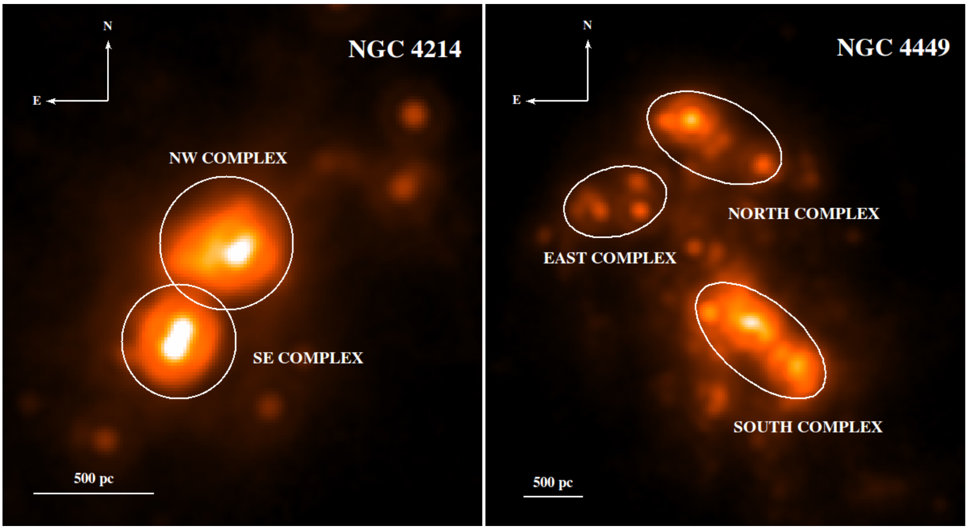

Figure 4.3: MIPS 24 μm image with the apertures used to extract the photometry of the SF regions of NGC 4214 (left) and NGC 4449 (right)

BAND	$\lambda_0(\mu\mathrm{m})$	$F_{\mathrm{NW}}^{\mathrm{sub}}$ (Jy)	C_{apert}	C_{color}	F_{NW} (Jy)
IRAC8	7.872	0.163	1.000	0.590	0.276 ± 0.035
MIPS24	23.680	0.733	1.078	0.986	0.801 ± 0.103
PACS70	70.000	7.612	1.039	0.982	8.053 ± 1.031
PACS100	100.000	8.443	1.050	0.985	9.000 ± 1.153
PACS160	160.000	6.114	1.075	1.010	6.507 ± 0.833
SPIRE250	250.000	2.329	1.110	0.992	2.605 ± 0.443
MAMBO$^{(*)}$	1200.000	0.031	1.067	1.000	0.033 ± 0.010
S_{T}(0.5 cm)	5000.000	0.011	1.000	1.000	0.011 ± 0.003

Table 4.1: Flux densities for region NGC 4214 - NW obtained for an aperture of 21″ radius centred at RA=12h15m39.6s Dec=+36°19′36.″5 (J2000) (see left panel of Figure 4.3). $F_{\mathrm{NW}}^{\mathrm{sub}}$ is the measured, background-subtracted flux and F_{NW} is the final flux, after applying aperture and colour corrections. $^{(*)}$ The contribution from thermal radio emission was not subtracted.

The MIPS 24 μm image was used as it is the filter which is expected to most faithfully trace the warm dust in thermal equilibrium with the strong radiation fields from the star clusters in the PDRs and HII regions associated with the SF regions. The measured, background-subtracted fluxes are listed in column 3 in Tables 4.1 and 4.2 for NGC 4214 - NW ($F_{\mathrm{NW}}^{\mathrm{sub}}$)

BAND	$\lambda_0(\mu\mathrm{m})$	$F_{\mathrm{SE}}^{\mathrm{sub}}$ (Jy)	C_{apert}	C_{color}	F_{SE} (Jy)
IRAC8	7.872	0.105	1.000	0.590	0.178 ± 0.023
MIPS24	23.680	0.602	1.069	0.986	0.653 ± 0.084
PACS70	70.000	4.659	1.032	0.982	4.896 ± 0.627
PACS100	100.000	5.416	1.040	0.985	5.719 ± 0.732
PACS160	160.000	4.094	1.057	1.010	4.285 ± 0.549
SPIRE250	250.000	1.689	1.078	0.992	1.835 ± 0.312
MAMBO(*)	1200.000	0.029	1.021	1.000	0.029 ± 0.009
$\mathrm{S_T}$(0.5 cm)	5000.000	0.005	1.400	1.000	0.007 ± 0.002

Table 4.2: Flux densities for region NGC 4214 - SE obtained for an aperture of 18″ radius centred at RA=12h15m40.8s Dec=+36°19′05.″5 (J2000) (see Figure 4.3). $F_{\mathrm{SE}}^{\mathrm{sub}}$ is the measured, background-subtracted flux and F_{SE} is the final flux, after applying aperture and colour corrections. (*) The contribution from thermal radio emission was not subtracted.

and NGC 4214 - SE ($F_{\mathrm{SE}}^{\mathrm{sub}}$), respectively, and in Tables 4.4, 4.5 and 4.6 for NGC 4449 - EAST ($F_{\mathrm{EAST}}^{\mathrm{sub}}$), NGC 4449 - NORTH ($F_{\mathrm{NORTH}}^{\mathrm{sub}}$) and NGC 4449 - SOUTH ($F_{\mathrm{SOUTH}}^{\mathrm{sub}}$), respectively.

One issue of particular relevance to the quantitative analysis presented in this paper is that of the subtraction of the local background underlying the SF regions. Ideally, we need to cleanly separate the localised dust/PAH emission associated with the HII regions and the local PDRs on scales of tens of parsecs (marking the interface between the tenuous gas ionised by the star cluster and the dense material of the parent molecular clouds) from the underlying extended emission from diffuse dust distributed on the kpc scale of the disk. In practice it is very challenging to perform such a separation, not only because of blending effects due to the finite angular resolution (these are quantified through the aperture corrections described in Section 4.2.2, below) but also because of the limited range of UV photons which have escaped the SF regions and have passed into the diffuse dust layer, forming a halo around the SF regions. In the case of the very luminous and dominant SF regions, this escaping UV light is expected to produce a detectable halo of dust emission extending beyond the local PDRs on linear scales of the mean free path between absorption events on dust grains in the diffuse dust layer.

The extent and brightness of this diffuse halo emission is expected to vary strongly with infrared wavelength in a way which is both difficult to measure directly and also uncertain to predict theoretically on an a priori basis. Therefore, for simplicity, we have opted to make no attempt to subtract the underlying diffuse background when performing aperture photometry on the SF regions. For future reference we simply note here that we may thereby be overestimating the flux densities of the SF regions, most particularly in the PAH bands,

BAND	$\lambda_0(\mu\mathrm{m})$	$F_{\mathrm{DISK}}^{\mathrm{sub}}$ (Jy)	C_{color}	F_{DISK} (Jy)	F_{DIFF} (Jy)
IRAC8	7.872	0.678	0.590	1.149 ± 0.115	$0.695^{+0.075}_{-0.090}$
MIPS24	23.680	2.050	0.986	2.080 ± 0.208	$0.625^{+0.104}_{-0.124}$
MIPS70	71.440	23.945	0.893	26.814 ± 5.363	$13.417^{+3.082}_{-4.084}$
PACS70	70.000	24.209	0.982	24.652 ± 2.466	$11.703^{+1.393}_{-1.672}$
PACS100	100.000	35.309	0.985	35.847 ± 3.585	$21.128^{+2.279}_{-2.735}$
PACS160	160.000	34.097	1.010	33.759 ± 3.376	$22.967^{+2.380}_{-2.856}$
MIPS160	155.900	39.016	0.971	38.574 ± 7.715	$27.287^{+5.605}_{-6.042}$
SPIRE250	250.000	18.888	0.992	19.033 ± 2.855	$14.594^{+2.204}_{-2.645}$
PLANCK350	350.000	9.546	0.986	9.682 ± 0.988	$7.933^{+0.797}_{-0.870}$
SPIRE350	363.000	10.059	0.999	10.068 ± 1.510	$8.453^{+1.281}_{-1.321}$
SPIRE500	517.000	4.497	1.025	4.387 ± 0.659	$3.848^{+0.580}_{-0.590}$
PLANCK550	550.000	3.635	0.921	3.947 ± 1.318	$3.510^{+1.173}_{-1.177}$
PLANCK850	850.000	0.946	0.887	1.066 ± 0.264	$0.958^{+0.231}_{-0.232}$
MAMBO$^{(*)}$	1200.000	0.350	1.000	0.350 ± 0.106	$0.288^{+0.087}_{-0.105}$

Table 4.3: Flux densities of NGC 4214 for an aperture of 5′ radius centred at RA=12h15m39.1s Dec=+36°19′34.″5 (J2000) (see Figure 4.1). $F_{\mathrm{DISK}}^{\mathrm{sub}}$ is the measured, background-subtracted flux, F_{DISK} is the final flux of the entire galaxy, after applying colour correction, and F_{DIFF} is the flux of the diffuse emission obtained as $F_{\mathrm{DISK}} - (F_{\mathrm{NW}} + F_{\mathrm{SE}})$. The lower error of F_{DIFF} includes the contribution of smaller and less intense SF regions in the disk (see Sect. 4.4). $^{(*)}$ The contribution from thermal radio emission was not subtracted.

but also to some extent around the peak of the SED in the FIR. The effect at MIPS 24 μm , however, is likely to be small, since, as already noted, this band is primarily sensitive to warm dust heated by the intense radiation fields in the PDRs and HII regions close to the star clusters.

For the measurement of the total emission of NGC 4214 and NGC 4449 we chose, in both cases, an aperture of 5′ in radius (see Figures 4.1 and 4.2). We tested with growth curves at all wavelengths that this aperture enclosed the entire emission of the galaxies (see Figures 4.4 and 4.5 for a selection of growth curves at MIPS 24 μm, MIPS 70 μm, MIPS 160 μm, SPIRE 250 μm, SPIRE 350 μm, and SPIRE 500 μm bands). For the PLANCK measurements, which include the total emission of the galaxy, the apertures could not be chosen. However, their values are very close (see Section 4.1.5) to ours, and our growth curves showed that at the radius of the PLANCK beam the emission was enclosed completely.

The total emission from the MAMBO 1.2 mm map of NGC 4214 is more uncertain due to

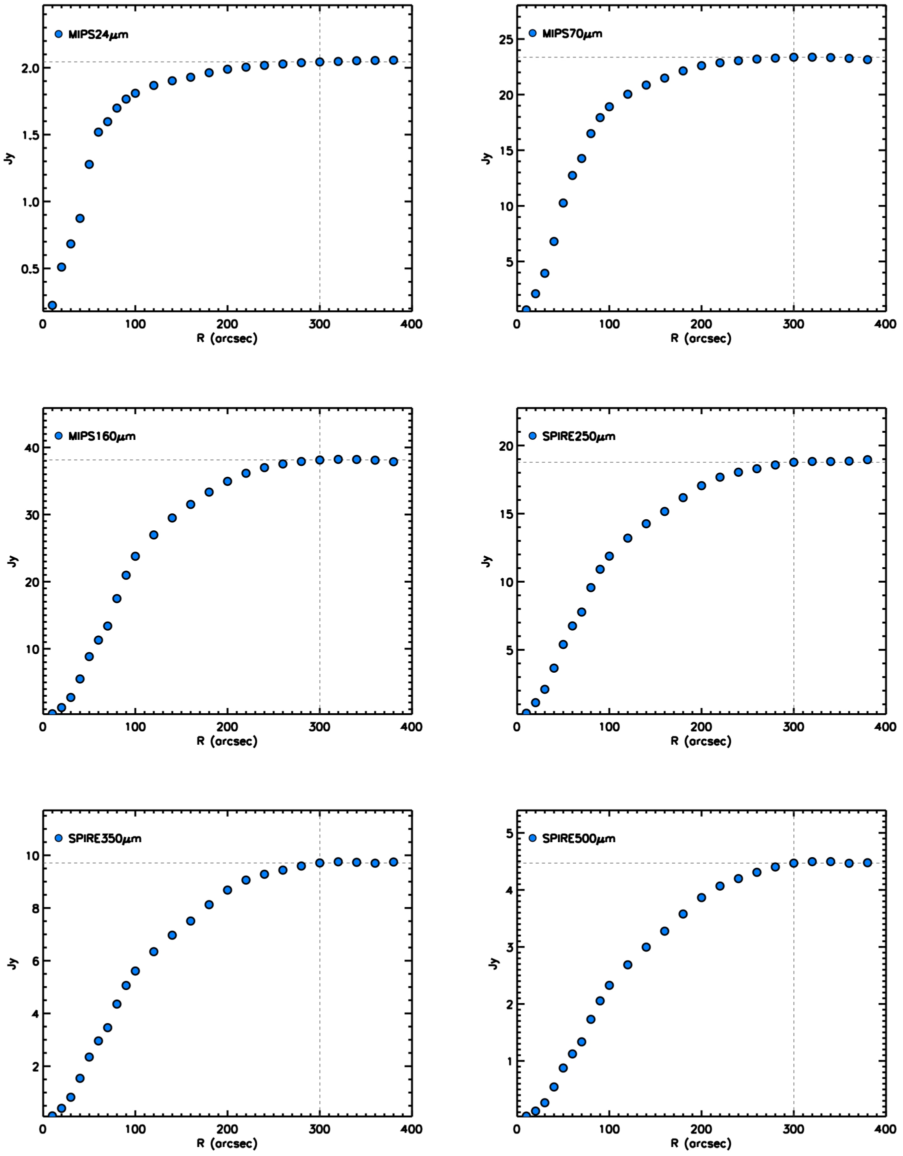

Figure 4.4: MIPS 24 μm (top left), MIPS 70 μm (top right), MIPS 160 μm (middle left), SPIRE 250 μm (middle right), SPIRE 350 μm (bottom left) and SPIRE 500 μm (bottom right) growth curves of NGC 4214.

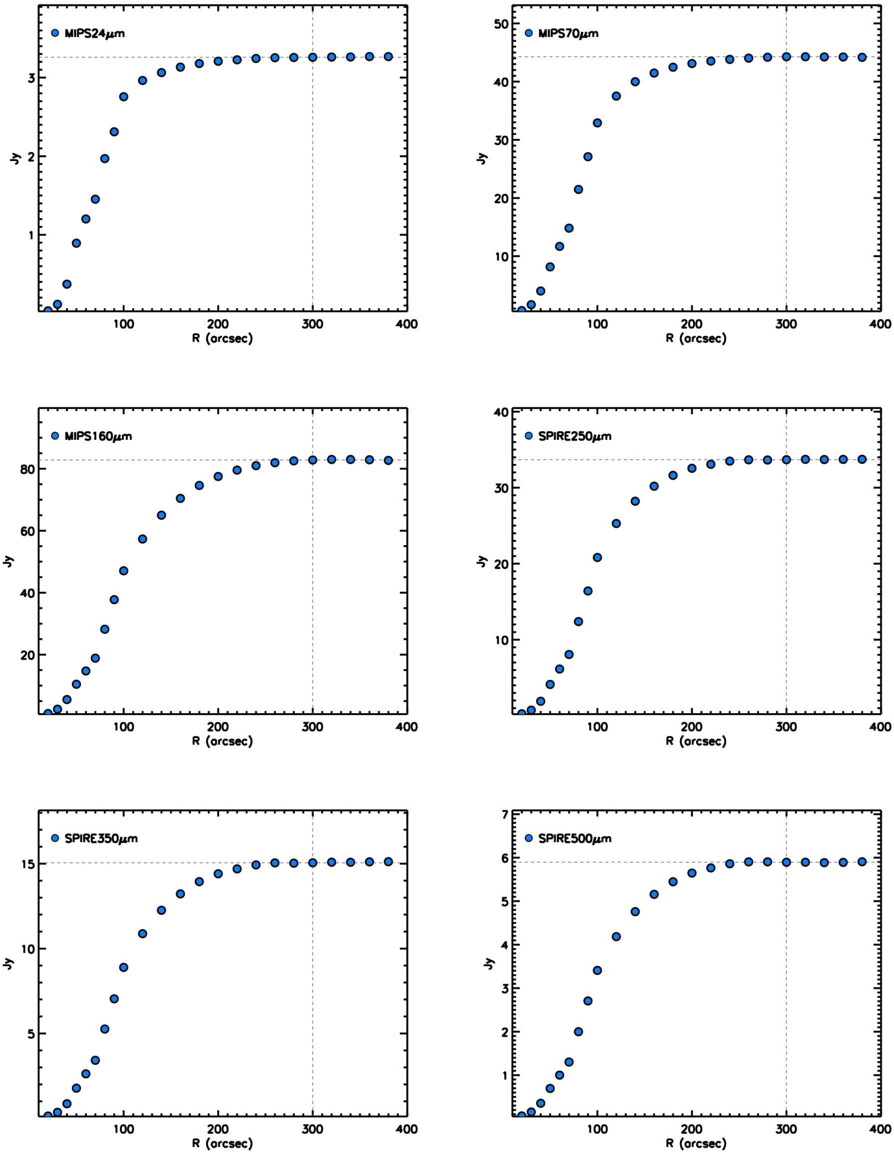

Figure 4.5: MIPS 24 μm (top left), MIPS 70 μm (top right), MIPS 160 μm (middle left), SPIRE 250 μm (middle right), SPIRE 350 μm (bottom left) and SPIRE 500 μm (bottom right) growth curves of NGC 4449.

BAND	$\lambda_0(\mu\mathrm{m})$	$F^{\mathrm{sub}}_{\mathrm{EAST}}$ (Jy)	C_{apert}	C_{color}	F_{EAST} (Jy)
IRAC8	7.872	0.088	1.000	0.590	0.150 ± 0.030
MIPS24	23.680	0.158	1.121	0.986	0.180 ± 0.036
MIPS70	71.440	2.035	1.381	0.893	3.147 ± 0.629
MIPS160	155.900	2.332	1.717	0.971	4.123 ± 0.825
SPIRE250	250.000	1.461	1.189	0.992	1.751 ± 0.350
SPIRE350	363.000	0.582	1.282	0.999	0.746 ± 0.149
SPIRE500	517.000	0.203	1.429	1.004	0.288 ± 0.058
VLA3cm	35300.000	0.003	1.000	1.000	0.003 ± 0.001

Table 4.4: Flux densities for region NGC 4449 - EAST obtained for an aperture of semi-major axis of 23.8″, semi-minor axis of 15.4″ and position angle of 15.4° centred at RA=12h28m17.0s Dec=+44°06′32.″8 (J2000) (see right panel of Figure 4.3). $F^{\mathrm{sub}}_{\mathrm{EAST}}$ is the measured, background-subtracted flux and F_{EAST} is the final flux, after applying aperture and colour corrections.

the poor signal-to-noise ratio at the outer parts of the area covered by our observations, which is practically the same as the aperture of 5′ used for the other images. In the moderately smoothed image (resolution 18″), shown in Figure 4.1 no diffuse emission can be seen. However, when we smooth the map to an angular resolution of 40″ diffuse dust emission becomes visible in the inner 160″ (see Figure 4.6) whose structure resembles to those in the SPIRE 500 μm map. Beyond this radius we are not sure that the structures are real. The growth curve of MAMBO 1.2 mm keeps raising until ~ 200″ where it becomes approximately flat. We obtained integrated fluxes of 0.26 ± 0.03 Jy and 0.35 ± 0.11 Jy for the apertures of 160″ and 300″, respectively. The lower value should represent a reliable lower limit for the total flux in NGC 4214. The total flux is more uncertain, however, given the flatness of the growth-curve beyond 200″, we are confident that the flux at 300″ is a reasonable estimate. In the case of NGC 4449 we used as a lower limit the flux reported by Böttner et al. (2003), which covers the three SF complexes but not the entire disk of the galaxy. Due to these uncertainties, for both galaxies we did not include the MAMBO data point in our fitting procedure but we show it in the figures for comparison with the models.

The measured, background-subtracted fluxes of the total emission are listed in column 3 of Tables 4.3 and 4.7 for NGC 4214 and NGC 4449, respectively.

BAND	$\lambda_0(\mu\mathrm{m})$	$F^{\mathrm{sub}}_{\mathrm{NORTH}}$ (Jy)	C_{apert}	C_{color}	F_{NORTH} (Jy)
IRAC8	7.872	0.179	1.000	0.590	0.303 ± 0.061
MIPS24	23.680	0.443	1.132	0.986	0.509 ± 0.102
MIPS70	71.440	4.306	1.425	0.893	6.871 ± 1.374
MIPS160	155.900	4.582	1.925	0.971	9.084 ± 1.817
SPIRE250	250.000	2.825	1.202	0.992	3.424 ± 0.685
SPIRE350	363.000	1.076	1.304	0.999	1.404 ± 0.281
SPIRE500	517.000	0.376	1.503	1.004	0.563 ± 0.113
VLA3cm	35300.000	0.012	1.000	1.000	0.012 ± 0.002

Table 4.5: Flux densities for region NGC 4449 - NORTH obtained for an aperture of semi-major axis of 32.5″, semi-minor axis of 17.9″ and position angle of 155.5° centred at RA=12h28m12.8s Dec=+44°07′01.″8 (J2000) (see right panel of Figure 4.3). $F^{\mathrm{sub}}_{\mathrm{NORTH}}$ is the measured, background-subtracted flux and F_{NORTH} is the final flux, after applying aperture and colour corrections.

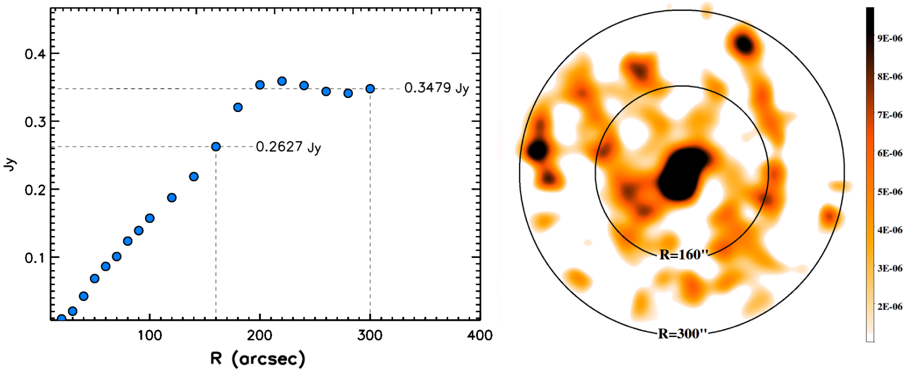

Figure 4.6: MAMBO 1.2 mm growth curve (left) obtained for the 40″ smoothed image (right) for the galaxy NGC 4214. The units of the colorbar are Jy.

BAND	$\lambda_0(\mu\mathrm{m})$	$F^{\mathrm{sub}}_{\mathrm{SOUTH}}$ (Jy)	C_{apert}	C_{color}	F_{SOUTH} (Jy)
IRAC8	7.872	0.464	1.000	0.590	0.787 ± 0.157
MIPS24	23.680	1.171	1.139	0.986	1.352 ± 0.270
MIPS70	71.440	7.534	1.475	0.893	12.445 ± 2.489
MIPS160	155.900	6.879	2.213	0.971	15.678 ± 3.136
SPIRE250	250.000	4.058	1.202	0.992	4.918 ± 0.984
SPIRE350	363.000	1.533	1.312	0.999	2.013 ± 0.403
SPIRE500	517.000	0.498	1.544	1.004	0.766 ± 0.153
VLA3cm	35300.000	0.018	1.000	1.000	0.018 ± 0.004

Table 4.6: Flux densities for region NGC 4449 - SOUTH obtained for an aperture of semi-major axis of 35.3″, semi-minor axis of 17.9″ and position angle of 140.5° centred at RA=12h28m10.9s Dec=+44°05′29.″8 (J2000) (see right panel of Figure 4.3). $F^{\mathrm{sub}}_{\mathrm{SOUTH}}$ is the measured, background-subtracted flux and F_{SOUTH} is the final flux, after applying aperture and colour corrections.

BAND	$\lambda_0(\mu\mathrm{m})$	$F^{\mathrm{sub}}_{\mathrm{DISK}}$ (Jy)	C_{color}	F_{DISK} (Jy)	F_{DIFF} (Jy)
IRAC8	7.872	1.786	0.590	3.028 ± 0.606	$1.788^{+0.358}_{-0.429}$
MIPS24	23.680	3.261	0.986	3.308 ± 0.662	$1.267^{+0.253}_{-0.304}$
MIPS70	71.440	44.198	0.893	49.494 ± 9.899	$27.031^{+5.406}_{-6.487}$
MIPS160	155.900	82.968	0.971	85.446 ± 17.089	$56.561^{+11.312}_{-13.575}$
SPIRE250	250.000	33.658	0.992	33.929 ± 6.786	$23.837^{+4.767}_{-5.721}$
PLANCK350	350.000	14.745	0.986	14.955 ± 2.991	$10.895^{+2.179}_{-2.325}$
SPIRE350	363.000	15.042	0.999	15.057 ± 3.011	$10.894^{+2.179}_{-2.615}$
SPIRE500	517.000	5.891	1.004	5.867 ± 1.173	$4.251^{+0.850}_{-1.020}$
PLANCK550	550.000	4.804	0.903	5.320 ± 1.064	$4.301^{+0.860}_{-0.884}$
PLANCK850	850.000	1.218	0.887	1.373 ± 0.275	$1.130^{+0.226}_{-0.231}$
MAMBO	1200.000	0.260	1.000	0.260 ± 0.078	$0.182^{+0.055}_{-0.057}$

Table 4.7: Flux densities of NGC 4449 for an aperture of 5′ radius centred at RA=12h15m39.1s Dec=+36°19′34.″5 (J2000) (see Figure 4.2). $F^{\mathrm{sub}}_{\mathrm{DISK}}$ is the measured, background-subtracted flux, F_{DISK} is the final flux of the entire galaxy, after applying colour correction, and F_{DIFF} is the flux of the diffuse emission obtained as $F_{\mathrm{DISK}} - (F_{\mathrm{NW}} + F_{\mathrm{SE}})$. The lower error of F_{DIFF} includes the contribution of smaller and less intense SF regions in the disk (see Sect. 4.5).

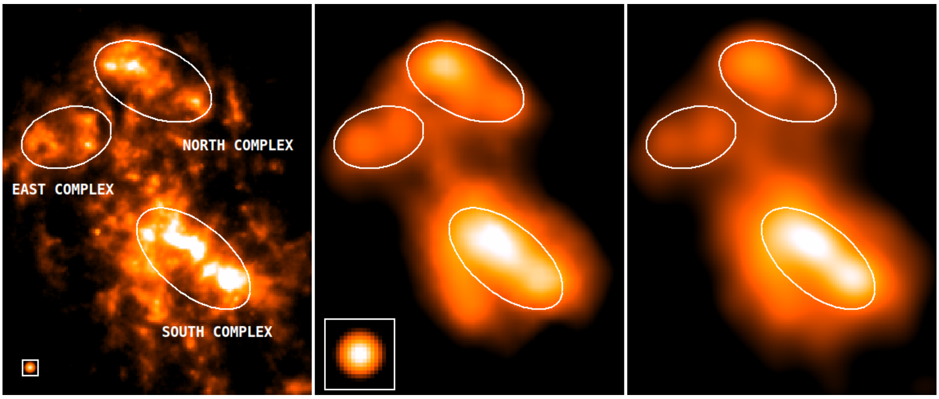

Figure 4.7: Illustration of the method used in this work to calculate the aperture corrections. The IRAC 8 μm image of NGC 4449 (left) is used as the high-resolution model of emission distribution at the MIPS 70 μm band (middle). The outgoing flux measured in the convolved IRAC 8 μm image (right) is used to compute the aperture correction. At the left lower corner of the IRAC 8 μm and MIPS 70 μm images their PSFs are shown. The side of the square is $4''$ and $36''$ for IRAC 8 μm and MIPS 70 μm, respectively. In both cases, the side of the box is twice the FWHM.

4.2.2 Aperture correction

Because of the different resolutions of the images we applied aperture corrections to the IR fluxes of the SF regions. We derived values of the aperture correction by adopting the IRAC 8 μm as the high-resolution model of the flux distribution. We first measured the flux within the SF region apertures in the IRAC 8 μm image. Then we convolved the IRAC 8 μm image with the point-spread-function (PSF) of the FIR/submm bands, and measured again the flux within the same apertures. The ratio between the flux measured in the original and convolved images gives the aperture correction for each band (see Figure 4.7). The values are listed in column 4 of Tables 4.1 and 4.2.

4.2.3 Colour corrections

When photometric measurements are made with a broad filter, then the total flux measured, $F = \int F_{\nu} T_{\nu} d\nu$ (with T_{ν} being the transmission curve of the filter), is related to a monochromatic flux assuming a certain spectral shape of the source. In order to directly compare the monochromatic fluxes with the models of Popescu et al. (2011) and Groves et al. (2008), we applied colour corrections to the IRAC, MIPS, PACS, SPIRE and Planck fluxes. We followed the procedures described in the corresponding manuals[1], where colour correction factors for different source distributions are listed.

We chose the colour correction factors for the spectrum that most closely resembled the model spectrum at a given wavelength. For both galaxies, for the MIPS 24 μm band we adopted a blackbody with a temperature of 70 K, whereas in the range from 70 μm to 160 μm a blackbody with a temperature of 50 K.

In the FIR/submm range, NGC 4214 and NGC 4449 present SEDs with different slopes (see Figure 4.8). For SPIRE 250 and 350 μm and PLANCK 350 μm we used the colour corrections for spectral indexes $\alpha = +2$ and $\alpha = +2.5$ for NGC 4214 and NGC 4449, respectively. For SPIRE 500 μm and PLANCK 550 μm we adopted $\alpha = +2.5$ and $\alpha = +3.0$ for NGC 4214 and NGC 4449, respectively. Finally, for PLANCK 850 μm we used $\alpha = +3.0$ for NGC 4214 and $\alpha = +3.5$ for NGC 4449.

For the particular case of IRAC 8 μm, for both galaxies we adopted the colour correction for a PAH-dominated spectrum. At 8 μm we additionally compared model and data by generating synthetic integrated fluxes. For this we (i) multiplied the model spectrum with the 8 μm filter profile and integrated it over the 8 μm filter band and (ii) multiplied the observed 8 μm data, adopting the black body of $T = 10^4$ K profile on which the flux definition of IRAC is based, with the 8 μm profile and integrated it over the 8 μm filter band. The comparison of both values allowed an alternative estimate of the colour correction, based entirely on the data and the model spectrum. We found that this comparison produced within 10% the same ratios as the comparison between colour corrected data point and model flux.

The colour corrections for NGC 4214 are listed in Tables 4.1, 4.2 and 4.3, and in Tables 4.4, 4.5, 4.6 and 4.7 for NGC 4449.

4.2.4 Line contamination

Most of the FIR/submm broad-band filters used for this work are contaminated by molecular or atomic emission lines. In the cases where data were available, we estimated the line contamination by comparing the luminosity of the emission line with the total luminosity measured in the filter, obtained by integrating the product of the source spectrum and the spectral response of the filter over the frequency range of the filter band.

Emission lines from different CO rotational transitions fall into SPIRE, PLANCK and MAMBO filters. In the case of NGC 4214, we used the CO(1-0) map presented by Walter et al. (2001)

---

[1] see the IRAC Instrument Handbook, MIPS Instrument Handbook, PACS Observer's Manual, SPIRE Observers' Manual and Planck Collaboration (2011) for IRAC, MIPS, SPIRE and Planck, respectively.

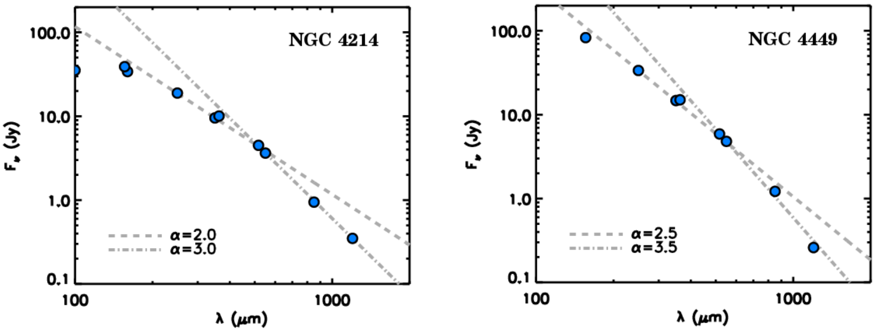

Figure 4.8: FIR/submm SEDs of NGC 4214 (left) and NGC 4449 (right). Note the different slopes of the SEDs in this regime. the exponent α is defined as $F_\nu \propto \nu^\alpha$.

as a reference. We determined a velocity integrated flux of 9.3 Jy km s^{-1} in the NW region and 12.8 Jy km s^{-1} in the SE region. The MAMBO filter band, with a bandwidth of about 80 GHz, is affected by the CO(2-1) line. We estimate the flux of the CO(2-1) line from the measured CO(1-0) value assuming that the line intensity ratio it is given by the value for optically thick, thermalised CO, $\mathrm{I_{CO(1-0)}}/\mathrm{I_{CO(2-1)}} = 1$. The contribution of the CO(2-1) line to the total measured flux at 1.2 mm of the NW and SE complex is then 0.87% and 1.27%, respectively. For other bands, the contamination by higher CO transitions is more than an one order of magnitude smaller.

PACS spectroscopic maps of atomic FIR lines ([OI] 63, [OIII] 88, [NII] 122, [OI] 146, [CII] 158 and [NII] 205μm) of NGC 4214 were presented by Cormier et al. (2010). With a field of view of 1.6′ x 1.6′, only the central part of the galaxy is observed. However, this region completely covers the main SF complexes NGC 4214 - NW and NGC 4214 - SE where the major part of the line emission originates. Therefore, we do not expect to severely underestimate the total emission of these lines. [OI] 63 and [OIII] 88μm fall into the bandpass of the MIPS 70 μm (see left panel in Figure 4.9) and PACS 70 μm filter. The luminosities reported by Cormier et al. (2010) are $0.89 \times 10^6\ L_\odot$ for [OI] 63 μm and $1.99 \times 10^6\ L_\odot$ for [OIII] 88μm. The sum of these values corresponds to 1.11% (1.33%) of the total luminosity measured in the PACS 70 μm (MIPS 70 μm) band. [OIII] 88μm fall into the bandpass of the PACS 100 μm filter. Its luminosity corresponds to 1.73% of the total luminosity measured in the PACS 100 μm band. [OI] 146 and [CII] 158μm fall into the bandpass of the MIPS 160 μm (see right panel in Figure 4.9) and PACS 160 μm filter. The reported luminosities for [OI] 146 and [CII]μm lines are $0.05 \times 10^6\ L_\odot$ and $2 \times 10^6\ L_\odot$, respectively, which together represents 2.88% (4.26%) of the total luminosity measured in the PACS 160 μm (MIPS 160 μm) band.

Due to the small contribution from the atomic and molecular lines to the FIR/submm bands, we did not apply any decontamination to our measurements except for the PACS 160 μm and MIPS 160 μm bands. These have been included in Tables 4.1, 4.2 and 4.3.

In the case of NGC 4449, the flux reported by Böttner et al. (2003) at 1.2 mm included CO decontamination, and therefore, no further corrections were necessary. Note that no atomic line emission data is available for NGC 4449. However, due to the negligible/small corrections applied in the case of NGC 4214, we do not believe that the line contamination has a noticeable impact on the SEDs of NGC 4449.

4.2.5 Error handling

In our analysis, the monochromatic flux for each band, F_{reg}, with the subindex *reg* corresponding to the SF regions as well as to the disk depending on the aperture considered, was calculated from the background-subtracted flux as it follows:

$$F_{reg} = \frac{C_{\mathrm{apert}}}{C_{colour}} \times F_{reg}^{\mathrm{sub}} - F^{lines}, \tag{4.2}$$

where C_{apert} and C_{colour} are the aperture and colour corrections, respectively, and F^{lines} is the total flux of the lines present in the bandpass of the filter. To estimate the flux of the background, we measure the median value of an annulus beyond the disk of the galaxy.

To calculate the errors of the fluxes, we took into account three types of error: (i) calibration,

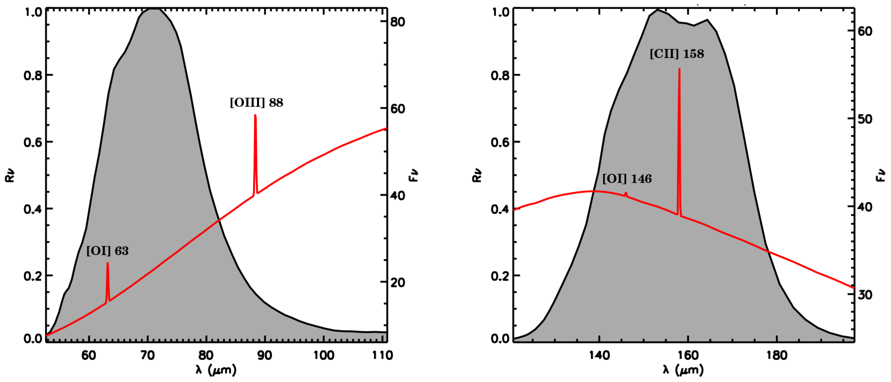

Figure 4.9: Atomic line-emission at the MIPS 70 μm (left) and MIPS 160 μm filters spectral responses. In both figures, the left vertical axis corresponds to the spectral response of the filter (grey area) and the right vertical axis corresponds to the flux density of the SED (red).

$\Delta_{\rm cal}$, for which we adopted the values mentioned in Sect. 4.1, (ii) measurement error due to background fluctuations, $\Delta_{\rm back}$, and (iii) an estimate of the error due to the uncertainty in the aperture size of regions SE and NW, $\Delta_{\rm apert}$ (this error was not relevant for the total emission). We neglected the uncertainties introduced by the colour and aperture corrections.

The error due to the background fluctuations was calculated assuming that each pixel within the aperture has an error given by the standard deviation of the background noise, $\sigma_{\rm back}$. In addition, we had to take into account the error of the background which was subtracted within an aperture of $N_{\rm apert}$ pixels. This error is $\sigma_{\rm back} N_{\rm apert} / \sqrt{N_{\rm back}}$, where $N_{\rm back}$ is the number of pixels used to compute the level of background. This gives (see also Dale et al. 2012) a total error for the background subtracted flux of:

$$\Delta_{\rm back} = \sigma_{\rm back} \sqrt{N_{\rm apert} + \frac{N^2_{\rm apert}}{N_{\rm back}}} \tag{4.3}$$

We estimated the error $\Delta_{\rm apert}$ by changing the aperture size for the SF regions by $\pm 1''$. We obtained changes in the integrated fluxes between 4 and 8% for the different bands. We adopted conservatively an error of $\Delta_{\rm apert} = 8\%$ for all bands.

The final error for the flux is the quadratic sum of $\Delta_{\rm cal}$, $\Delta_{\rm back}$, and $\Delta_{\rm aper}$. This is listed for NGC 4214 in Tables 4.1, 4.2 and 4.3 for the fluxes in each band, and in Tables 4.4, 4.5, 4.6 and 4.7 for NGC 4449. The dominant error sources were $\Delta_{\rm cal}$ and $\Delta_{\rm aper}$, whereas $\Delta_{\rm back}$ was found to be negligible for most wavelengths.

4.3 Constraints on the input parameters

The large amount of ancillary data covering a wide wavelength range, as well as the result of previous studies from the literature allow us to determine or at least constrain most of the input parameters for both models.

4.3.1 Parameters of Groves et al. (2008) model

The main SF complexes of NGC 4214 and NGC 4449 are formed by an ensemble of smaller HII regions. Ideally, all these smaller knots of SF should be modelled separately. However, IR/submm observations lack the angular resolution to perform such a detailed analysis. Due to this limitation, for the SF complexes we adopted parameter ranges which are wide enough to enclose the values of their individual knots.

For both galaxies, $N_{\rm HI}^{\rm PDR}$ was not constrained but fixed the value 10^{22} cm^{-2}, typical of molecular clouds in our own galaxy. In the case of NGC 4214, with the only exception of $N_{\rm HI}^{\rm PDR}$, the input parameters of the model of Groves et al. (2008) were observationally constrained. In the case of NGC 4449, it was not possible to constrain the parameters $\mathcal{C}$ and p_0.

(i) Metallicity: For the SF regions of NGC 4214 Kobulnicky and Skillman (1996) found the values of $Z = 0.32\,Z_\odot$ for NW and $Z = 0.41\,Z_\odot$ for SE. We used a metallicity of $Z=0.4\,Z_\odot$ and also tested $Z=0.2\,Z_\odot$, which yielded a similar result (no template for $Z=0.3\,Z_\odot$ is available in Groves et al. (2008)). For the SF regions of NGC 4449 we adopted $Z=0.4\,Z_\odot$ as the closest value to the averaged metallicity of $Z = 0.45 \pm 0.07\,Z_\odot$from Lequeux et al. (1979), Talent (1980), and Martin (1997).

(ii) Age: The age of the stellar clusters of NGC 4214 (see top panel of Figure 4.10) have been extensively studied by different authors. Leitherer et al. (1996) presented HST *Faint Object Spectrograph* (FOS) ultraviolet spectra covering the main star cluster of the NW complex. Using spectral synthesis modelling, Leitherer et al. (1996) reported for this stellar cluster an age of 4-5 Myr. Maíz-Apellániz et al. (1998) obtained optical long-slit spectra of NGC 4214 with the ISIS spectrograph of the William Herschel Telescope. Their bidimensional spectra covered both SF complexes. From the comparison of different observationally determined parameters (equivalent width of Hβ, Wolf-Rayet population, effective temperature and UV absorption lines) to synthesis models, they determined ages of 3±1 Myr for both regions. MacKenty et al. (2000) mapped the central part of NGC 4214 with the HST *Wide Field Planetary Camera 2* (WFPC2). From the Hα equivalent width, these authors determined an average age of 3.0-4.0 Myr and 2.5-3.0 Myr for the NW and SE regions, respectively. More recently, Úbeda et al. (2007) also used the WFPC2 data set to determine the ages of the star clusters by a likelihood-maximization technique from the photometric colours. They determined an age of 5 Myr and of 2-4 Myr for the star clusters within the NW and the SE complex, respectively. Based on the dispersion found by these studies, we adopted ages of the NW and SE complexes of 3-5 Myr and 2-4 Myr, respectively.

In the case of NGC 4449, Reines et al. (2008) reported the age of 13 thermal radio sources by comparing their Hα equivalent widths with spectral synthesis models. The radio sources studied by these authors are shown in the bottom panel of Figure 4.10. It is important to note that Reines et al. (2008) excluded from their study those radio sources where the radio spectrum includes a contribution from synchrotron emission, which are more evolved sources. Therefore, we expect that the age that we estimate for the SF complexes from the biased sample of Reines et al. (2008) underpredicts their actual age.

(iii) Ambient pressure and Compactness: p_0 and $\mathcal{C}$ can be determined by comparing the expected and the observed radii of the individual HII regions as a function of the age. For a

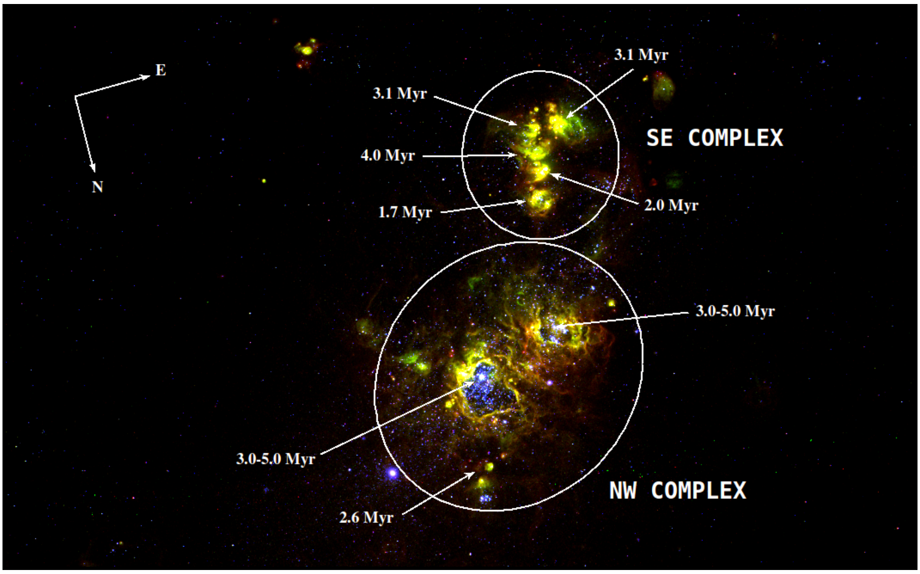

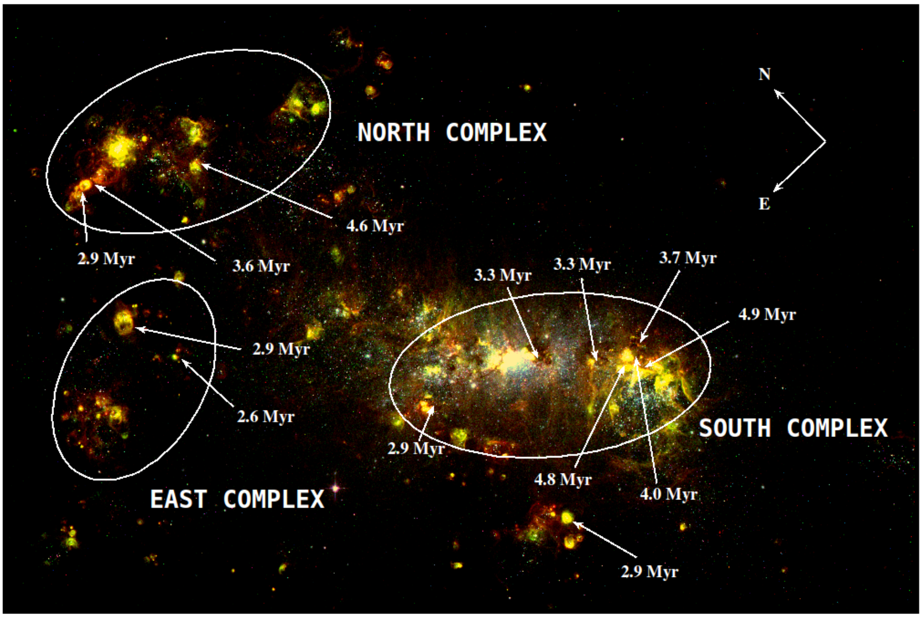

Figure 4.10: RGB composition of the HST-WFC3 data of NGC 4214 (top) and HST-ACS data of NGC 4449 with the ages of the stellar clusters superimposed.

cluster of a given age it is possible to find different combinations of p_0 and $\mathcal{C}$ that provide the observed radius of the expanding bubble. However, this degeneracy can be avoided when the mass of the star cluster is known, since both parameters p_0 and $\mathcal{C}$ are related by the equation:

$$\log\left(\frac{M_{cl}}{M_{\odot}}\right) = \frac{5}{3} \times \log(\mathcal{C}) - \frac{2}{3} \times \log\left(\frac{p_0/k}{cm^{-3}K}\right) \tag{4.4}$$

In the case of NGC 4214 we used the values of the masses reported by Úbeda et al. (2007) and we obtained that for the NW complex the value of p_0 ranges from 7.0 to 8.0 and $\mathcal{C}$ ranges from 5.5 to 6.5. For the case of the SE complex, we found that p_0 ranges from 6.0 to 7.0 and that $\mathcal{C}$ ranges from 4.5 to 5.5. We used these intervals to constrain both parameters.

In the case of NGC 4449, Reines et al. (2008) reported the mass of the 13 radio sources shown in Figure 4.10. However, their biased sample only represents a fraction of the stellar clusters that are actually heating the dust and therefore, it was not possible to constrain $\mathcal{C}$ and p_0 for this galaxy.

(iv) Covering factor: We assumed that the PDR consists of optically thick, homogeneously distributed clouds that surround the star cluster, leaving a fraction uncovered so that the light can escape unattenuated from these ”holes”. To a good approximation, the intrinsic luminosity of the central star cluster is the sum of the observed luminosities of the stars, L_{star}, and the luminosity re-emitted by the dust, L_{dust}. The covering factor is then $f_{cov} = L_{dust}/(L_{dust} + L_{star})$. We obtained L_{dust} by integrating the best-fit model template (see Sect. 6) from 3μm to 1.5 mm. Ideally, to calculate L_{star} we need to correct fluxes measured in our apertures for the SF regions for the attenuation produced by the diffuse dust layer and then, integrate these fluxes from *GALEX* FUV to IRAC 3 μm. However, the exact value of the opacity in front of the SF regions due to the diffuse dust is not known.

For NGC 4214 we carried out two different estimates of the local opacity, τ^{local}, of the diffuse dust layer, the first based on the lowest and the second on the highest realistic opacity. i) We adopted as τ^{local} the foreground opacity of $\tau_V = 0.35$ (Úbeda et al. 2007) measured locally in front of the main stellar cluster of the NGC 4214 - NW region. The stars in this cluster seem to have evacuated most of the surrounding material associated with the HII region so that this value is expected to be lower than the average disk opacity in this area. Since both SF regions are located at the centre of NGC 4214, we assumed that this value of τ^{local} is representative for both SF regions. We obtained $f_{cov}^{NW} = 0.45$ and $f_{cov}^{SE} = 0.65$ for the NGC 4214 - NW and NGC 4214 - SE regions, respectively. ii) We used the value of $\tau_B^f = 2.0$ which is the best fit value derived from our modelling of the diffuse emission (see Section 4.4.2). Assuming that the regions are at the centre of the galaxy and at mid-plane, and using the inclination angle i = 44° (Walter et al. 2008), the opacity in front of the SF complexes is calculated as

$\tau^{\rm local} = 0.5 \times \tau_{\rm B}^{\rm f} / \cos({\rm i}) = 1.4$. In this case, we obtained $\rm f_{cov}^{NW} = 0.20$ and $\rm f_{cov}^{SE} = 0.30$. Thus, we obtain estimates for the covering factor of $\rm f_{cov}^{NW} = 0.20 - 0.45$ and $\rm f_{cov}^{SE} = 0.30 - 0.65$ for both SF complexes of NGC 4214.

In the case of NGC 4449 there is no study similar to the performed by Úbeda et al. 2007 of the main cluster of NGC 4214 - NW. For this reason, we assume as a lower limit for the dust extinction that the stellar clusters have removed totally the diffuse dust in front of them, i.e., we assume that $\tau^{\rm local} = 0$. In this case, we obtained $\rm f_{cov}^{EAST} = 0.65$, $\rm f_{cov}^{NORTH} = 0.70$ and $\rm f_{cov}^{SOUTH} = 0.45$ for the NGC 4449 - EAST, NGC 4449 - NORTH and NGC 4449 - SOUTH regions, respectively. The second estimation was obtained from the value derived from our modelling (τ_B^f=3, see Section 4.5.2) similarly as we did in point ii) for NGC 4214. In the case of NGC 4449, the SF complexes are not located at the centre of the galaxy. We estimate $\tau^{\rm local}$ at the distance from the centre of each region using the same exponential distribution of dust assumed in Popescu et al. (2011) model:

$$\tau_B(r) = \tau_B^f \times e^{-r/h_{dust}} = \tau_B^f \times e^{-r/1.4\times h_s} \tag{4.5}$$

Note that the scale-length of the dust distribution, $\rm h_{dust}$, is fixed to $1.4\times\rm h_s$ in the Popescu et al. (2011) model. Thus, for an inclination angle of i = 60° (Walter et al. 2008) and assuming that the regions are at mid-plane, we obtained $\rm f_{cov}^{EAST} = 0.50$, $\rm f_{cov}^{NORTH} = 0.55$ and $\rm f_{cov}^{SOUTH} = 0.10$. Thus, for NGC 4449 we obtained the ranges of $\rm f_{cov}^{EAST} = 0.55 - 0.65$, $\rm f_{cov}^{NORTH} = 0.55 - 0.70$ and $\rm f_{cov}^{SOUTH} = 0.10 - 0.45$.

4.3.2 Parameters of Popescu et al. (2011) model

In the case of the model of Popescu et al. (2011) the parameters that we could determine observationally are:

(i) Bulge-to-disk ratio: Since no bulge is visible in the late-type galaxies NGC 4214 and NGC 4449, we set B/D = 0.

(ii) Inclination angle: Following Walter et al. (2008), we fix i = 44° and i = 60° for NGC 4214 and NGC 4449, respectively.

***(iii) Scale-length**:* For both galaxies, we determined the radial stellar scale-length in the B-band from a SLOAN g-band image. First, we removed the background of the image by calculating the average value of a wide set of small circular apertures placed strategically outside the disk of both galaxies. Then, we removed the contamination from foreground stars and HII regions, including the central SF regions. We used the IRAF task ellipse (STSDAS package) with steps of 20″ to determine the isophotes. Finally, we fitted an exponential function to the surface brightness profile determined with the mean values in each isophotal ellipse. We considered the ellipses whose mean values and the corresponding uncertainties were above the dispersion of the background level (~ 1 count).

For both galaxies, we found that it is not possible to fit the profile for the whole disk with a single exponential function. For this reason we decided to calculate separately the scale-length in the inner and the outer part of their disks (see Fig. 4.11). We visually determined the changes of slope to take place at a radius ~ 90″ and ~ 110″ for NGC 4214 and NGC 4449. The profile of the inner part of the disk (after masking the SF regions) can be well fitted with scale-lengths of ~ 450 pc and ~ 605 pc for NGC 4214 and NGC 4449, respectively. For the outer parts we determined a scale-length of 873^{+172}_{-123} pc and 1002^{+83}_{-71} pc for NGC 4214 and NGC 4449, respectively.

***(iv) Clumpiness**:* As a first estimate of the clumpiness factor F, we used the mean value from the upper and the lower limits obtained for the SF complexes, i. e., F = 0.40 ± 0.20 for NGC 4214 and F = 0.50 ± 0.20 for NGC 4449. Note that the clumpiness is only used for the modelling of the total integrated UV/optical/FIR emission described in Sections 4.4.3 and 4.5.3 for NGC 4214 and NGC 4449, respectively.

***(v) old**:* We derived old by assuming that all the luminosity in the J, H and K bands (see Tables 4.8 and 4.9 for NGC 4214 and NGC 4449, respectively) corresponds to the old stellar population. For both galaxies we integrated the luminosity in the J, H and K bands and derived *old* as the ratio of this luminosity and the integrated luminosity of the model galaxy (Table E2 in Popescu et al. 2011). We obtained old = 0.009 and old = 0.028 for NGC 4214 and NGC 4449, respectively.

4.4 The SED of NGC 4214

In a first step we separately fitted the emission from the SF regions and from diffuse dust. In a second step we self-consistently combined the emission from the SF regions with that from the diffuse dust to fit the total emission of the galaxy.

The emission from the NGC 4214 - NW and NGC 4214 - SE regions have been directly measured from the maps as described in Section 4.2. The diffuse emission has been calculated as the difference between the total emission and the sum of the emission from the two SF com-

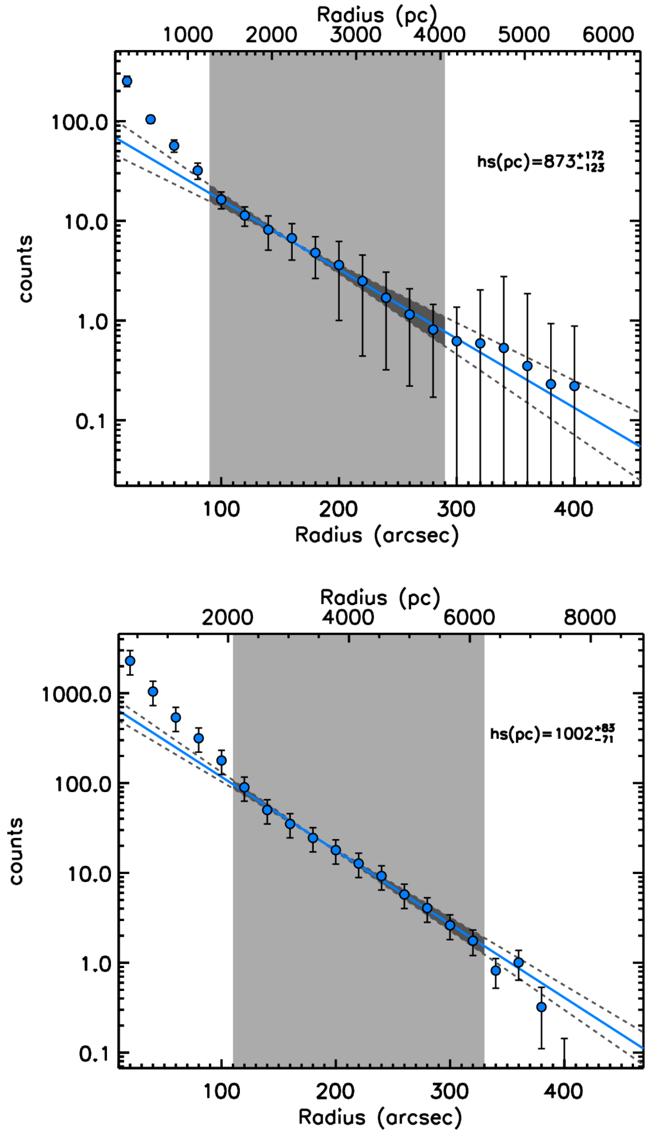

Figure 4.11: B-band scale-length of the stellar disk of NGC 4214 (top) and NGC 4449 (bottom). The fit (solid line) was achieved using the isophotes in the radial range marked by the grey-shaded area. The uncertainty in the slope is represented by the dark grey area and the dark grey dashed lines.

plexes. For the data points where no direct measurement was available, the best-fit model value (see below) was taken. The values for the diffuse dust emission are listed in Table 4.3.

BAND	$\lambda_0(\mu\text{m})$	F_{DISK} (Jy)	Reference
FUV	0.154	0.072 ± 0.007	1
NUV	0.232	0.091 ± 0.009	1
B	0.445	0.354 ± 0.056	2
V	0.551	0.446 ± 0.064	2
J	1.220	0.520 ± 0.014	3
H	1.630	0.614 ± 0.023	3
K	2.200	0.458 ± 0.022	3

Table 4.8: Total stellar flux densities of NGC 4214. (1) This work, (2) de Vaucouleurs et al. (1991b), (3) Jarrett et al. (2003).

BAND	$\lambda_0(\mu\text{m})$	F_{DISK} (Jy)	Reference
FUV	0.154	0.152 ± 0.030	1
NUV	0.232	0.165 ± 0.033	1
SLOANu	0.355	0.241 ± 0.048	1
B	0.445	0.450 ± 0.090	2
SLOANg	0.469	0.495 ± 0.099	1
SLOANr	0.617	0.717 ± 0.143	1
SLOANi	0.748	0.817 ± 0.163	1
SLOANz	0.893	0.884 ± 0.177	1
J	1.220	0.914 ± 0.183	3
H	1.630	1.070 ± 0.214	3
K	2.190	0.839 ± 0.168	3

Table 4.9: Total stellar flux densities of NGC 4449. (1) This work, (2) de Vaucouleurs et al. (1991b), (3) Jarrett et al. (2003).

In order to take into account the emission from smaller and less intense SF regions in the disk of NGC 4214, we estimated their contribution from the Hα emission of the ten brightest secondary SF regions which corresponds to 18% of the Hα emission of NGC 4214 - SE+NW. We assume that the shape of the dust SED from these smaller SF regions is the same as the sum of the SEDs of NGC 4214 - SE+NW, and we include their contribution in the calculation of the lower error range of the fluxes of the diffuse dust component in each band (see Table 4.3). The smaller HII regions only have a noticeable effect on the emission at 24 and

70 μm.

4.4.1 Best fits for the SF regions

The best-fit models for the NGC 4214 - NW and NGC 4214 - SE complexes are shown in Figures 4.12 and 4.13, respectively. We obtained a good fit for all our observed photometric points longwards of 10 μm. For a metallicity of Z=0.4 $Z_\odot$ the best-fit models of the two complexes correspond to the parameters $\mathcal{T}$= 4.0 Myr, $\mathcal{C}$= 5.0, p_0= 8 and f_{cov}= 0.30 for both regions. With the exception of the $\mathcal{C}$ of the NGC 4214 - NW region and p_0 of the NGC 4214 - SE region, all the parameters fall within our parameter ranges constrained from the observations (see Sect. 4.3.1).

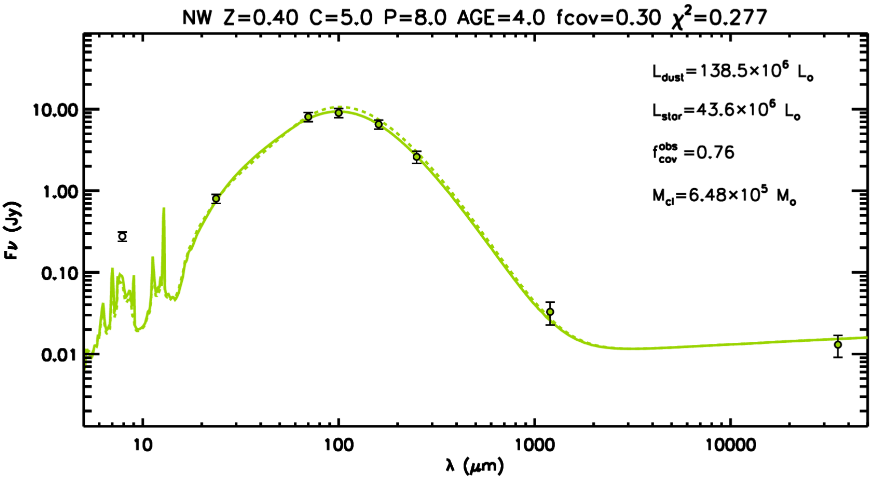

Figure 4.12: Best-fit models to the NGC 4214 - NW complex for Z=0.4 $Z_\odot$ (solid line) and Z=0.2 $Z_\odot$ (dashed line). The values of the reduced χ^2 (neglecting the IRAC 8 μm point, drawn with an open circle) are 0.28 and 0.78 for Z=0.4 and 0.2 $Z_\odot$, respectively.

For a metallicity of Z=0.2 $Z_\odot$ the best fit parameters are in the case of the NGC 4214 - NW region $\mathcal{T}$= 5.0 Myr, $\mathcal{C}$= 5.0, p_0= 7 and f_{cov}= 0.30 and in the case of the NGC 4214 - SE region $\mathcal{T}$= 3.5 Myr, $\mathcal{C}$= 4.5, p_0= 8 and f_{cov}= 0.60. The value for $\mathcal{C}$ in NGC 4214 - NW is slightly lower, and p_0 in NGC 4214 - SE slightly higher, but the rest of the parameters are within the constrained ranges.

We note that the IRAC 8 μm data point was excluded from our fitting procedure. The reason is that both models considerably underestimate the emission at 8 μm. Specifically, from our best-fit models for Z=0.2 $Z_\odot$ we obtained that the observed fluxes are larger than the model values by a factor of 3.8 and 4.0 for NGC 4214 - NW and NGC 4214 - SE, respectively. In the

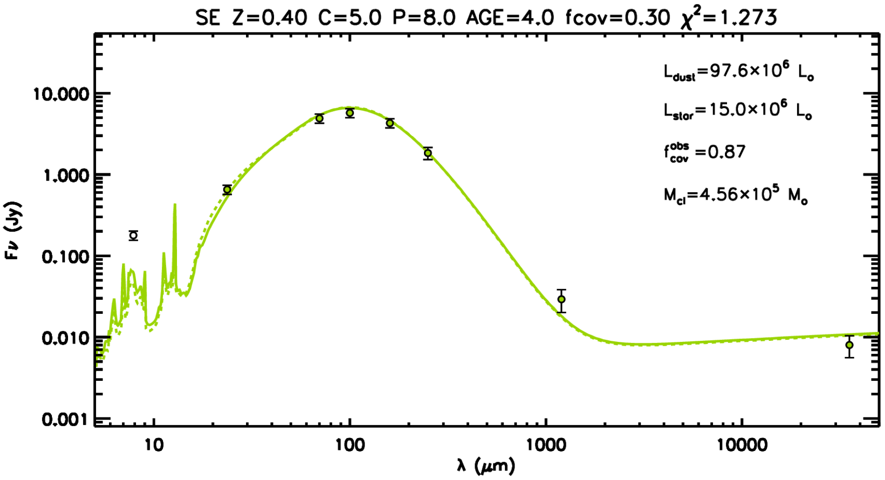

Figure 4.13: Best-fit model to the NGC 4214 - SE complex for Z=0.4 $Z_\odot$ (solid line) and Z=0.2 $Z_\odot$ (dashed line). The values of the reduced χ^2 (neglecting the IRAC 8 μm point, drawn with an open circle) are 1.27 and 0.97 for Z=0.4 and 0.2 $Z_\odot$, respectively.

case of the best-fit models of Z=0.4 $Z_\odot$ the discrepancy decreases to a factor of 3.1 and 2.9 for NGC 4214 - NW and NGC 4214 - SE, respectively. A complete discussion of the IRAC 8 μm discrepancy will be given in Sect. 4.6.

4.4.2 Best fit for the diffuse emission

We searched the library of the diffuse dust SEDs of Popescu et al. (2011) for the best fit to the data in the MIR/submm range, leaving τ_B^f and SFR' as free parameters and keeping *old* fixed to the value 0.009. Fig. 4.14 shows the best fit obtained for our measured value h_s = 873 pc (solid red line), where we determined as best-fit values $\tau_B^f = 2$ and $\mathrm{SFR}' = 0.059\,M_\odot\,\mathrm{yr}^{-1}$. Neither the data point at 8 μm nor at 1.2 mm were taken into account in the χ^2 fitting procedure, the latter due to the observational limitations discussed in Sect. 4.2.1.

The model fits the data points in general very well. The largest discrepancy occurs at 8 μm where the model overpredicts the observations by a factor of 1.9. We will discuss this further in Sect. 4.6. At 160 μm there is a discrepancy with the PACS value which is overpredicted by 34% by the model, but the model prediction agrees within the errors with the MIPS data point at the same wavelength. The model overpredicts the SPIRE 250 μm point by 24% and underpredicts the 850 μm point by 34%. For the other data points the model predictions agree within the error bars.

It is instructive to compare this value of SFR', derived from the fit to the diffuse component

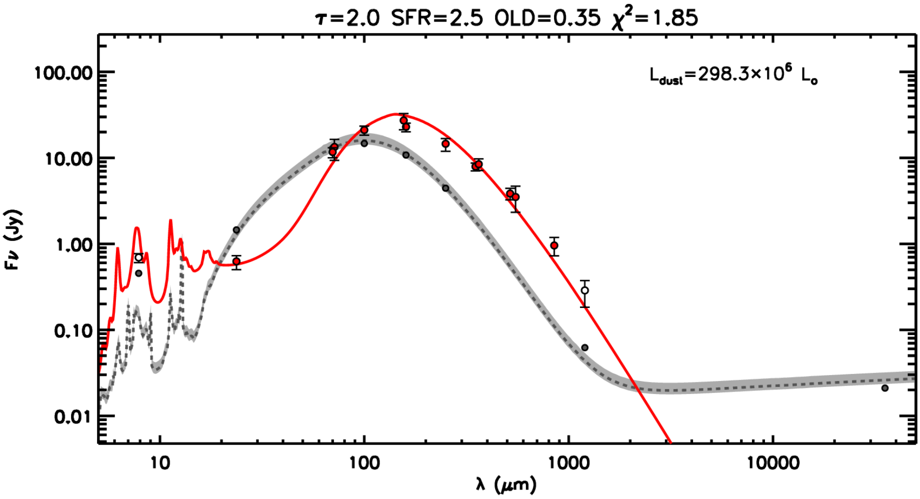

Figure 4.14: Fit to the diffuse emission of NGC 4214 keeping fixed *old* = 0.009 and leaving τ_B^f and SFR' as free parameters. The red solid line represents the best fit to the MIR/submm SED for the measured value of the scale-length h_s = 873 pc, obtained for τ_B^f= 2.0, and SFR′ = 0.059 $M_\odot\,yr^{-1}$. The dark grey dashed line corresponds to the sum of the best fit models of the HII regions presented in Figs. 4.12 and 4.13 and the grey-filled circles correspond to the sum of the photometric points of NGC 4214 - NW and NGC 4214 - SE regions. The light grey area represents the uncertainty in the estimation of the total emission of the HII regions. The value of the reduced χ^2 (neglecting the IRAC 8 μm and MAMBO 1.2 mm points, drawn with open circles) is 1.85.

of the dust emission, with the value for SFR' derived from our measurement of the spatially integrated flux density in the UV-to-blue band and which we will call, for clarity, $SFR'_{\rm UV}$ in the following. Applying the attenuation corrections due to diffuse dust, as tabulated in Popescu et al. (2011) for $\tau^{\rm f}_{\rm B}$ = 2 and an inclination of 44° we derive a value of $L_{\rm UV}$ = 3.70×10^{35} W. We then determine $SFR'_{\rm UV}$ following Eq. 17 in Popescu et al. (2011) as $SFR'_{\rm UV} = L_{\rm UV}/L^{young}_{unit,UV}$, where $L^{young}_{unit,UV}$ is the normalization factor. We obtain $\text{SFR}'_{\rm UV}$ = 0.165 $M_\odot\,yr^{-1}$. This is a factor of 2.8 times higher than the value of SFR' derived from the fitting of the diffuse dust emission. The most straightforward explanation for this discrepancy would be that the true value for the disk scale length h_s is higher than the adopted of 873 pc. This would favour a disk with lower dust surface densities, leading to a higher value of SFR' needed to account for the observed amplitude and colour of the diffuse dust emission. If we adopt for the scale-length the maximum allowed by the B-band images, h_s = 1045 *pc*, we obtain a best fit to the diffuse dust emission SED of $\tau^{\rm f}_{\rm B}$ = 1.2 and SFR′ = 0.088 $M_\odot\,yr^{-1}$. At the same time, this reduction in $\tau^{\rm f}_{\rm B}$ means that the deattenuated, integrated UV luminosity, $L_{\rm UV}$, is now lower, yielding $\text{SFR}'_{\rm UV}$ = 0.147 $M_\odot\,yr^{-1}$ which is only a factor of 1.67 greater than the value of SFR' derived from the diffuse dust emission. A complete discussion of this discrepancy will be given in Sect. 4.6.

As a further consistency check we can use the value of SFR' derived from the diffuse dust emission to make a different, global estimate of the fraction of the UV radiation escaping from the SF regions, $f_{\rm esc}$, and the corresponding clumpiness factor, F, and compare it with the corresponding value already derived in Sect. 4.3 from analysis of the direct and dust-re-radiated UV light seen from the spatially resolved SF regions. For this, we have to assume that the effective star formation rate powering the diffuse dust, SFR', is due to radiation escaping from the regions NW and SE. The total effective SFR produced by NW+SE is then $SFR'{+}SFR_{\rm loc}$ where $SFR_{\rm loc}$ is the effective star-formation rate needed to power the dust emission from the SF regions. We calculate $SFR_{\rm loc}$ by integrating the dust SED from the SF regions over the entire wavelength range, obtaining $L_{\rm dust}$, and assuming that this luminosity is equivalent to the same amount of UV radiation absorbed by the dust locally. We then determine $SFR_{\rm loc}$ in an equivalent way as described for $SFR'_{\rm UV}$ above, as $SFR_{\rm loc} = L_{\rm dust}/L^{young}_{unit,UV}$. We obtain $L_{\rm dust} = 9.06 \times 10^{34}$ W, which gives $\rm SFR_{loc} = 0.040\,M_{\odot}\,yr^{-1}$. With $\rm SFR' = 0.059\,M_{\odot}\,yr^{-1}$, derived from our best fit for the diffuse emission, we then obtain $f_{\rm esc}{=}\, SFR'/(SFR' + SFR_{\rm loc}) =$ 60% of the UV radiation of the SF region is required to escape from the SF complexes in order to heat the diffuse dust. This escape fraction corresponds to a $f_{\rm cov} = F = 1 - 0.60 = 0.40$, which is the same value derived in Sect. 4.3. We thus adopt in the following $F = 0.40 \pm 0.20$ (where the error comes from the range of $f_{\rm cov}$ derived in Sect. 4.3.1). From the best-fit value of SFR' and $F = 0.40$ we can estimate the value of the total star formation rate of NGC 4214 as $SFR = SFR'/(1 - F) = 0.059/(1 - 0.40) = 0.098\ \rm M_{\odot}yr^{-1}$.

4.4.3 Best fit for the total emission

On the MIR/FIR/submm part of Fig. 4.15 we show the fit to the total dust emission, which is the sum of the SEDs from the SF regions and the SED from the diffuse dust obtained in the previous sections. The entire dust SED from 8 μm to 850 μm can be well fitted.

On the UV/optical/NIR part of Fig. 4.15 we show the observed UV-optical SED (purple-filled circles). Following Eq. C.12 of Popescu et al. (2011), the UV/optical SED of the young stellar disk (purple-dashed line) of NGC 4214 was derredened (purple-solid line) using the composite attenuation, Δm_{λ}, which is for the case of $old \sim 0$:

$$\Delta m_{\lambda} = -2.5 \log (1 - F\, f_{\lambda}) + \Delta m_{\lambda}{}^{tdisk} \tag{4.6}$$

where the first part takes into account the attenuation in the SF regions and $\Delta m_{\lambda}{}^{tdisk}$ the

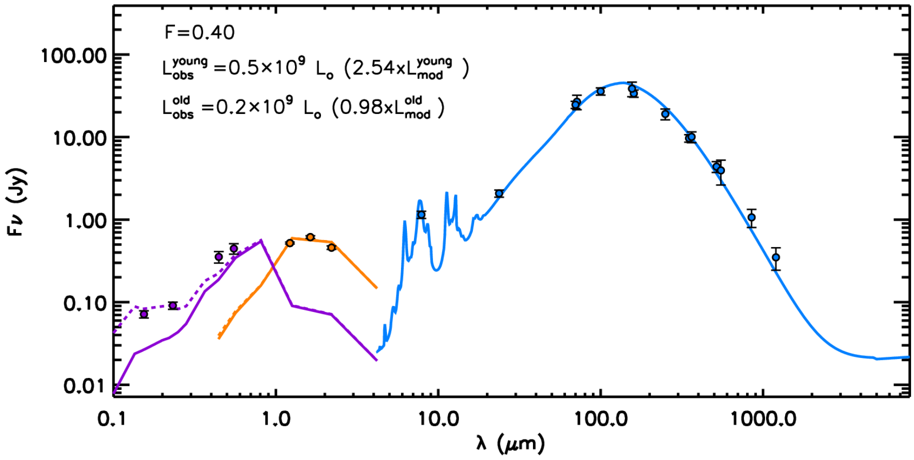

Figure 4.15: SED for the total emission of NGC 4214. On the MIR/FIR/submm part we show the best-fit solution for the total emission (blue solid line) obtained as the sum of the best fit models of the HII regions from Figs. 4.12 and 4.13 and the best fit model to the diffuse emission from Fig. 4.14, obtained for τ_B^f= 2.0 and SFR = 0.098 $M_\odot\,yr^{-1}$. On the UV/optical/NIR part, the purple-filled circles represent the observational UV/optical data and the orange-filled circles the observational IR data. The purple and orange dashed lines correspond to the intrinsic emission of the young and the old stellar populations, respectively; whereas the purple and orange solid lines correspond to the attenuated emission of the young and the old stellar populations, respectively.

attenuation of the diffuse component. The wavelength dependence of the escape fraction, f_λ, is tabulated in Table A.1 in Tuffs et al. (2004). The old stellar population SED (orange-dashed line) was attenuated (orange-solid line) using the attenuation correction derived for the old stellar component in the model of Popescu et al. (2011) $\Delta m_\lambda = \Delta m_\lambda{}^{disk}$. For both stellar populations we used the value of τ_B^f= 2.0 obtained from our best-fit model and an inclination angle of $i = 44°$ (Walter et al. 2008).

We now calculate, in a similar way as in Sect. 6.2 for SFR', from the intrinsic UV-to-blue luminosity the predicted value of the SFR, by applying Eq. 17 from Popescu et al. (2011), $SFR = L_{UV}^{tdisk}/L_{unit,UV}^{young}$. Using $F = 0.40$ in Eq. 4.6, we derive SFR = 0.22 $M_\odot\,yr^{-1}$, which is a factor of 2.24 higher than the value derived from the fitting of the dust SED (SFR = 0.098 $M_\odot\,yr^{-1}$). For $F = 0.20$ and $F = 0.60$, the highest and lowest values suggested by our data, the corresponding ratios are 2.51 and 2.18, respectively. If we adopt for the scale-length the maximum value allowed by the data h_s = 1045 pc, we obtain the best fit for τ_B^f = 1.2 and SFR′ = 0.088 $M_\odot\,yr^{-1}$, yielding $SFR = SFR'/(1-F) = 0.088/(1-0.40) = 0.14$

$M_\odot yr^{-1}$. In this case, the discrepancy with the value derived from the derredened UV-optical data, SFR = 0.188 $M_\odot$ yr^{-1}, decreases to a factor of 1.34 for $F = 0.40$ (1.50 and 1.27 for the $F = 0.20$ and $F = 0.60$, respectively).

A complete discussion of this discrepancy will be given in Sect. 4.6.

4.4.4 Gas-to-dust mass ratio

The total diffuse dust mass can be calculated from Eq. 44 of Popescu et al. (2011) ($M_{dust}^{diff} = \tau_B \times h_s^2 \times 0.99212\ pc^{-2} M_\odot$). With our values of $h_s = 873$ pc and $\tau_B = 2$ we obtain $M_{dust}^{diff} = 1.5 \times 10^6\ M_\odot$. This value is quite robust again changes in parameters: choosing the largest permitted scale-length, $h_s = 1045$ pc and the corresponding best fit for the opacity, $\tau_B = 1.2$, we obtain $M_{dust}^{diff} = 1.3 \times 10^6\ M_\odot$, only 13% lower. From the modelling of the HII complexes for $Z=0.4\,Z_\odot$, we derived dust masses of $M_{dust}^{NW} = 0.79 \times 10^5\ M_\odot$ and $M_{dust}^{SE} = 0.42 \times 10^5\ M_\odot$ for the NW and SE complexes, respectively. We therefore derived for NGC 4214 a total mass of dust $M_{dust}^{total} = M_{dust}^{diff} + M_{dust}^{NW} + M_{dust}^{SE} = 1.62 \times 10^6\ M_\odot$.

The total gas mass can be derived from $M_{HI} = 4.1 \times 10^8\ M_\odot$ (Walter et al. 2008) and $M_{H2} = 5.1 \times 10^6\ M_\odot$ (Walter et al. 2001, obtained with a Galactic conversion factor) and gives, taking into account a helium fraction of 1.36, $M_{gas} = 5.66 \times 10^8\ M_\odot$. The total gas-to-dust mass ratio is then $G_{dust} = 350$.

The Galactic CO-to-H_2 conversion factor (X-factor, adopted here as $N(H_2)/I_{CO} = 2{\times}10^{20}\ cm^{-2}(K\,km\,s^{-1})^{-1}$), most likely severely underestimates the total molecular gas mass in NGC 4214. An indication for this is e.g. the very high CII/CO ratio measured in the central region (Cormier et al., 2010) which shows that a large fraction of the CO is photo-dissociated due to the high radiation field and low dust shielding. Even though the X-factor has been notoriously difficult to determine, progress has been made in recent years mainly due to the possibility to derive dust masses with an increasingly better precision. This allows, together with HI and CO measurements and the assumption of a constant gas-to-dust mass ratio, to derive the ratio between total molecular gas mass and CO emission. Israel (1997) has first used this method and derived for NGC 4214 a 15-30 times higher X-factor than the Galactic value. Leroy et al. (2011) used spatially resolved data for the dust masses, derived from fits to HERSCHEL and SPITZER data, and the gas mass from HI and CO measurements for a small sample of nearby galaxies (M 31, M 33, LMC, SMC and NGC 6822) . Assuming that the gas-to-dust ratio and the X-factor are constant over the area considered they estimated both parameters by minimizing the scatter in the data. They found evidence for a strong increase of the X-factor below metallicities of 12-log(O/H) = 8.2-8.4, most likely due to the dissociation of CO and the creation of extended layers of CO-free H_2. Leroy et al. (2011) find for NGC 6822, which has a similar metallicity as NGC 4214 (12+log(O/H) = 8.2) an X-factor of 4-5 times the Galactic value. For the same galaxy, NGC 6822, and a similar method, Gratier et al. (2010) derived a higher X-factor (20 times the Galactic value). Taking this range of estimates into account, we adopt an X-factor 10 times the Galactic value as a reasonable estimate and derive for this case a gas-to-dust mass ratio of 387.

If we assume that the gas-to-dust mass ratio scales linearly with metallicity (which means that the fraction of metals incorporated in the dust is constant) we expect, based on the solar value of about 150, a value of G_{dust} between 375 (for $Z = 0.4\ Z_\odot$) to 500 (for $Z = 0.3\ Z_\odot$).

Thus, the observed gas-to-dust ratio is very close to the expected value in the case of $Z = 0.4\ Z_\odot$, and a factor 1.3 lower for $Z = 0.3\ Z_\odot$. Even though we consider this discrepancy small, it could indicate that there is a still larger amount of ”dark” molecular gas, not probed by the CO. We would need a conversion factor 35 times the Galactic value in order to obtain a gas-to-dust mass ratio of 500. An alternative possibility is that the dust properties in NGC 4214 are different with a higher dust extinction coefficient in the submillimeter wavelength range. This could be produced e.g. by amorphous graphite as suggested by Galliano et al. (2011) for the case of the LMC. Based on our data, we cannot distinguish between these two possibilities.

4.5 The SED of NGC 4449

We followed the same procedure as in the case of NGC 4214.

The contribution of smaller HII regions not taken into account within our apertures was measured performing photometry aperture over the HST-Hα image of the 30 brighter secondary HII regions and comparing their flux, 3.55×10^{-12}(ergs cm^{-2} s^{-1}), with the combined flux Hα of the primary HII complexes, 16.91×10^{-12}(ergs cm^{-2} s^{-1}). We obtained that the contribution of secondary HII regions is $\sim$ 20%.

4.5.1 Best fits for the SF regions

As in the case of NGC 4214, we obtained good fits for the SF complexes of NGC 4449 longwards of 10 μm. For the three SF regions, the metallicity was fixed to Z=0.4 $Z_\odot$. The best-fits were obtained for $\mathcal{T}$= 4.5 Myr, $\mathcal{C}$= 5.0, p_0= 8 and f_{cov}= 0.60 for NGC 4449 - EAST, $\mathcal{T}$= 4.0 Myr, $\mathcal{C}$= 5.0, p_0= 8 and f_{cov}= 0.55 for NGC 4449 - NORTH and $\mathcal{T}$= 4.0 Myr, $\mathcal{C}$= 5.0, p_0= 8 and f_{cov}= 0.55 for NGC 4449 - SOUTH. The age of NGC 4449 - EAST is higher than the value obtained by Reines et al. (2008) for the two knots within the aperture, whereas for

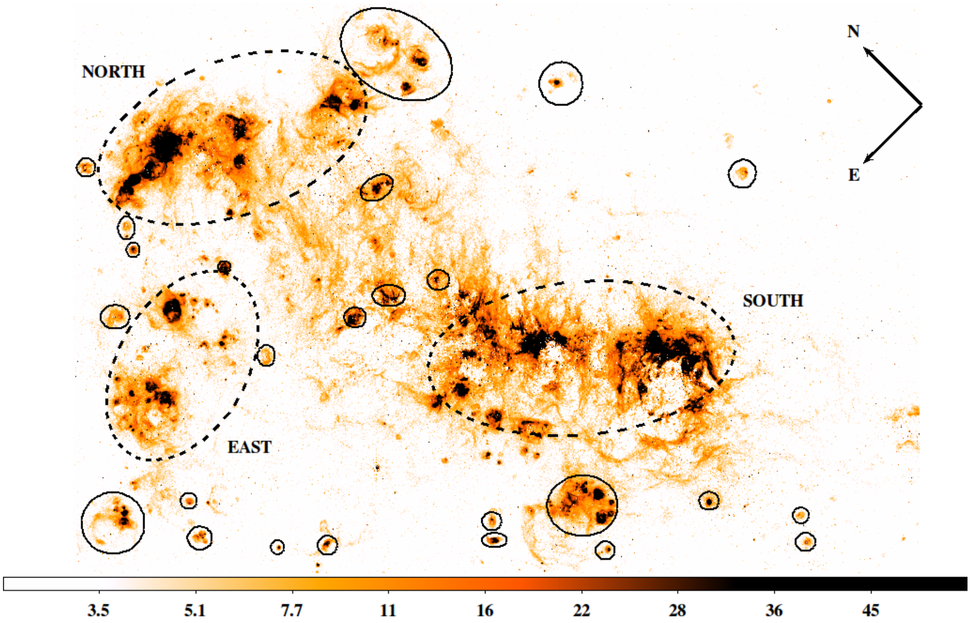

Figure 4.16: HST-ACS Hα image of NGC 4449 obtained with *LINEextractor* subtracting the filter F550M (stellar continuum) from the filter F658N (Hα+ continuum). The filter F814W was used as secondary stellar continuum to mask those pixels with relative error greater than 0.3 (see Section 2.2). The units of the colorbar are $10^{-18} \times \mathrm{erg/cm^2/s}$.

NGC 4449 - NORTH and NGC 4449 - SOUTH the ages found by our modelling fall within the constrained range. In the case of f_{cov}, the values obtained for NGC 4449 - NORTH and NGC 4449 - SOUTH fall slightly out of the range constrained, whereas the value obtained for NGC 4449 - EAST is compatible with the estimate. Although we were not able to constrain the parameters $\mathcal{C}$ and p_0, the values obtained for the SF regions in NGC 4449 are similar to the values found in the SF regions of NGC 4214, which have similar metallicity and age.

As we did in the case of NGC 4214, the IRAC 8 μm data point was excluded from our fitting procedure due to the model underprediction at this band. Specifically, from our best-fit models we obtained that the observed fluxes are larger than the model values by a factor of 4.8, 5.8 and 7.2 for NGC 4449 - EAST, NGC 4449 - NORTH and NGC 4449 - SOUTH, respectively. A complete discussion of the IRAC 8 μm discrepancy will be given in Sect. 4.6.

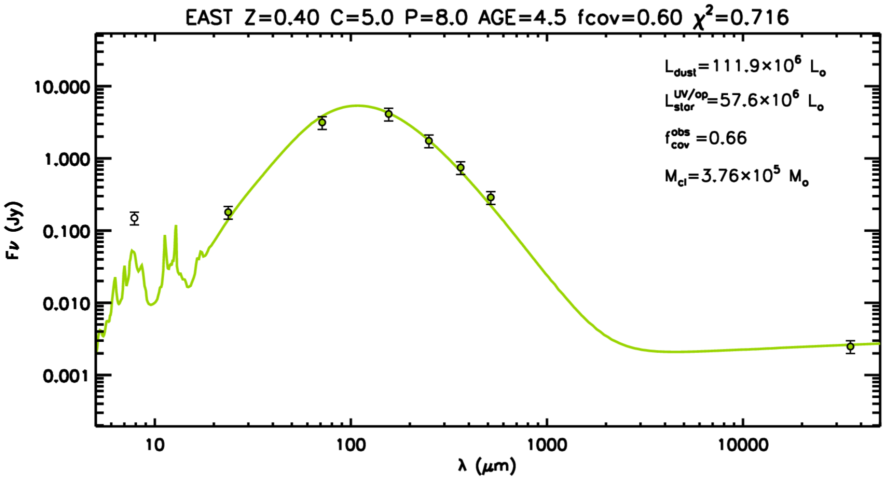

Figure 4.17: Best-fit model to the EAST complex for Z=0.4 $Z_\odot$. The values of the reduced χ^2 (neglecting the IRAC 8 μm point, drawn with an open circle) is 0.716.

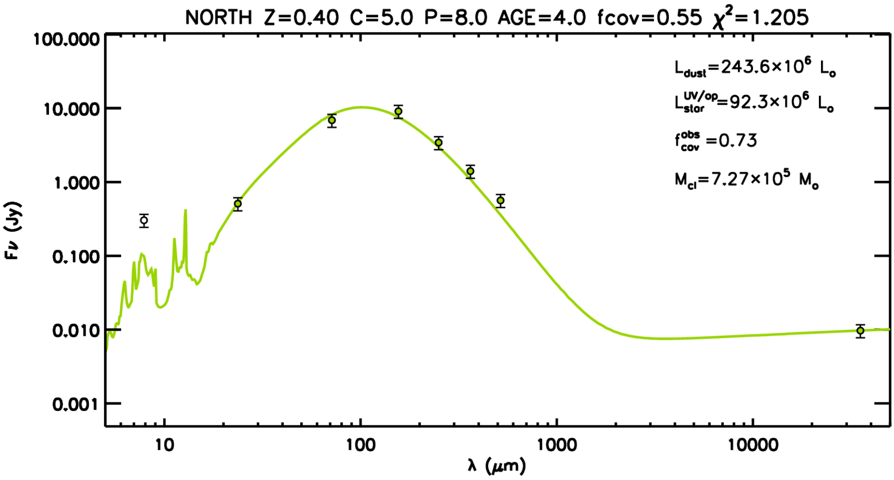

Figure 4.18: Best-fit model to the NORTH complex for Z=0.4 $Z_\odot$. The values of the reduced χ^2 (neglecting the IRAC 8 μm point, drawn with an open circle) is 1.205.

4.5.2 Best fit for the diffuse emission

As we did in the case of NGC 4214, we searched the library of the diffuse dust SEDs of Popescu et al. (2011) for the best fit to the data in the MIR/submm range, leaving τ_B^f and SFR' as free parameters and keeping *old* fixed to the value 0.028. Figure 4.20 shows the best fit obtained for our measured value $h_s = 1002$ pc (solid red line), where we determined as best-fit values $\tau_B^f = 3$ and SFR′ $= 0.187\,M_\odot\,yr^{-1}$. Neither the data point at 8 μm micron nor

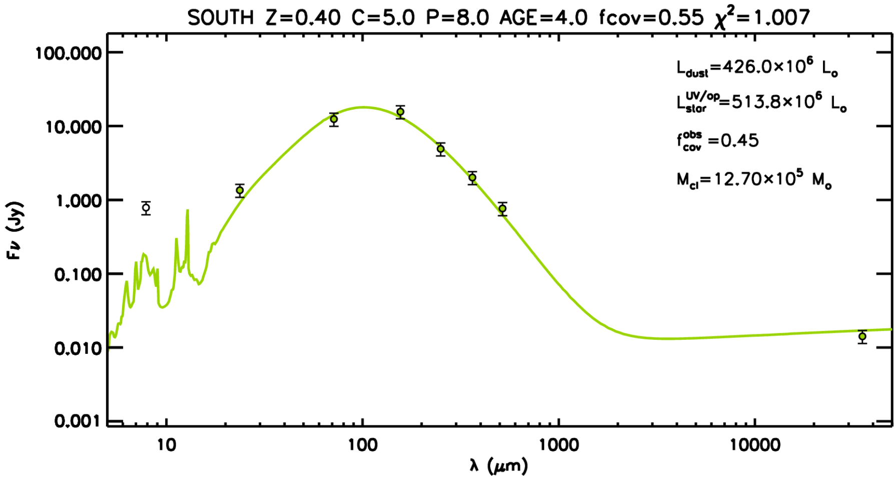

Figure 4.19: Best-fit model to the SOUTH complex for Z=0.4 $Z_\odot$. The values of the reduced χ^2 (neglecting the IRAC 8 μm point, drawn with an open circle) is 1.007.

at 1.2 mm, drawn with open circles, were taken into account in the χ^2 fitting procedure.

The model fits the data points in general very well. As in the case of NGC 4214, the largest discrepancies occur at the IRAC 8 μm band, where the model overpredicts the observations by a factor of 1.6, and at the PLANCK 850 μm band, where the model underpredicts the observations by $\lesssim$ 30%.

As we did in the case of NGC 4214, we can compare the value of SFR$'$ = 0.187 $M_\odot$ yr^{-1} derived from the fit to the diffuse dust emission with the value derived from the spatially integrated flux density in the UV, SFR$'_{\rm UV}$ = 1.083 $M_\odot$ yr^{-1}. The discrepancy in the case of NGC 4449 is 5.79. A complete discussion of this discrepancy will be given in Section 4.6.

As we did for NGC 4214, we can use the value of SFR' derived from the diffuse dust emission to make a different estimate of the clumpiness factor, F, and compare it with the corresponding value already derived in Sect. 4.3. From the best fits to the SF regions, we obtain $L_{\rm dust}$ = 781.5 × 10^6 $L_\odot$, which gives SFR$_{\rm loc}$ = 0.134 $M_\odot$ yr^{-1}. With SFR$'$ = 0.187 $M_\odot$ yr^{-1}, we then obtain $f_{\rm esc}$= $SFR'/(SFR' + SFR_{\rm loc})$ = 58% of the UV radiation of the SF region is required to escape from the SF complexes in order to heat the diffuse dust. This escape fraction corresponds to a $f_{\rm cov}$ = F = 1 − 0.58 = 0.42, which is within the range of the value F = 0.50 ± 0.20 derived in Section 4.3. From the best-fit value of SFR' and F = 0.50 we can estimate the value of the total star formation rate of NGC 4214 as $SFR = SFR'/(1-F) = 0.187/(1-0.50) = 0.374\ M_\odot{\rm yr}^{-1}$.

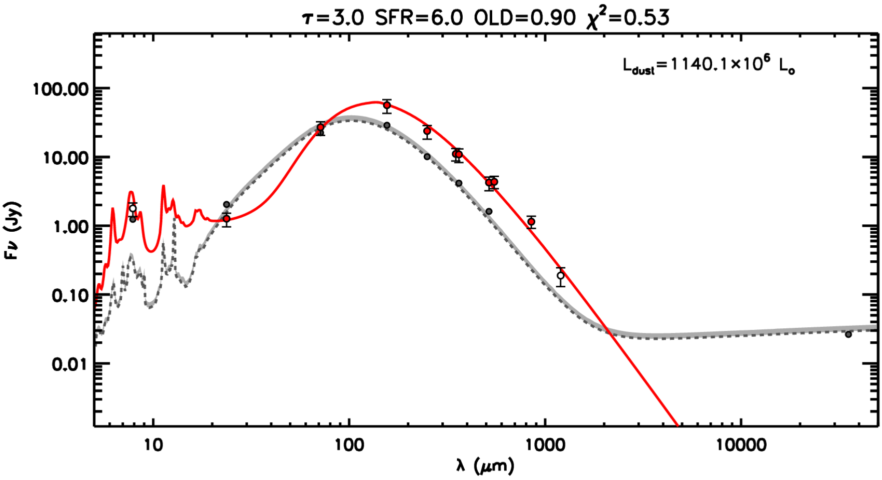

Figure 4.20: Fit to the diffuse emission of NGC 4449 keeping fixed old = 0.028 and leaving τ_B^f and SFR' as free parameters. The red solid line represents the best fit to the MIR/submm SED for the measured value of the scale-length $h_s = 1002\,\mathrm{pc}$, obtained for $\tau_B^f = 3.0$, and SFR′ = $0.187\,\mathrm{M}_\odot\,\mathrm{yr}^{-1}$. The dark grey dashed line corresponds to the sum of the best fit models of the HII regions presented in Figs. 4.17, 4.18 and 4.19 and the grey-filled circles correspond to the sum of the photometric points of NGC 4449 - EAST, NGC 4449 - NORTH and NGC 4449 - SOUTH regions. The light grey area represents the uncertainty in the estimation of the total emission of the HII regions. The value of the reduced χ^2 (neglecting the IRAC $8\,\mu$m and MAMBO 1.2 mm points, drawn with open circles) is 0.52. The MAMBO 1.2 mm photometric flux, reported by Böttner et al. (2003), it is considered a lower limit of the emission at 1.2 mm.

4.5.3 Best fit for the total emission

On the MIR/FIR/submm part of Figure 4.21 we show the fit to the total dust emission, which is the sum of the SEDs from the SF regions and the SED from the diffuse dust obtained in the previous sections. The entire dust SED from $8\,\mu$m to $850\,\mu$m can be well fitted.

On the UV/optical/NIR part of Fig. 4.21 we show the observed UV-optical SED (purple-filled circles). As we described in the case of NGC 4214, we followed the instructions of Popescu et al. (2011) to attenuate the SEDs of the young and old stellar population.

In the case of NGC 4449, we derive SFR = $1.559\,\mathrm{M}_\odot\,\mathrm{yr}^{-1}$ from the UV/optical SED, which is a factor of 4.17 higher than the value derived from the fitting of the dust SED (SFR = $0.374\,\mathrm{M}_\odot\,\mathrm{yr}^{-1}$). A complete discussion of this discrepancy will be given in Sect. 4.6.

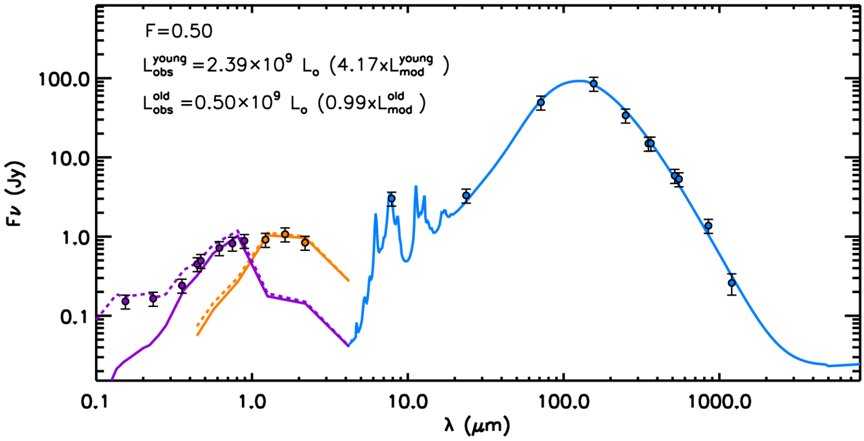

Figure 4.21: SED for the total emission of NGC 4449. On the MIR/FIR/submm part we show the best-fit solution for the total emission (blue solid line) obtained as the sum of the best fit models of the HII regions from Figs. 4.17, 4.18 and 4.19 and the best fit model to the diffuse emission from Figure 4.20, obtained for τ_B^f= 3.0 and SFR = 0.374 $M_\odot$ yr^{-1}. On the UV/optical/NIR part, the purple-filled circles represent the observational UV/optical data and the orange-filled circles the observational IR data. The purple and orange dashed lines correspond to the intrinsic emission of the young and the old stellar populations, respectively; whereas the purple and orange solid lines correspond to the attenuated emission of the young and the old stellar populations, respectively. The MAMBO 1.2 mm photometric flux, reported by Böttner et al. (2003), it is considered a lower limit of the emission at 1.2 mm.

4.5.4 Gas-to-dust mass ratio

Walter et al. (2008) reported for NGC 4449 a total mass of neutral Hydrogen of $M_{HI} = 1.1 \times 10^9\,M_\odot$. Böttner et al. (2003) found that the total luminosity of CO is 7.9×10^6 K km s^{-1} pc^2. For the Galactic CO-to-H$_2$ conversion factor $X_{CO} = 2 \times 10^{20}\,\mathrm{cm}^{-2}\,(\mathrm{K\,km\,s}^{-1})^{-1}$, or equivalently, $X_{CO} = 3.2\,M_\odot\,\mathrm{pc}^{-2}\,(\mathrm{K\,km\,s}^{-1})^{-1}$, we obtain a mass of molecular Hydrogen of $M_{H_2} = 25 \times 10^6\,M_\odot$. Thus, the total mass of Hydrogen is $M_{HI+H_2} = 1.125 \times 10^9\,M_\odot$, and taking into account a Helium fractions of 1.36, we obtain a total mass of gas of $M_{gas} = 1.530 \times 10^9\,M_\odot$.

As we did in the case of NGC 4214, the total diffuse dust mass of NGC 4449 was calculated using Eq. 44 of Popescu et al. (2011) ($M_{dust}^{diff} = \tau_B \times h_s^2 \times 0.99212\,\mathrm{pc}^{-2} M_\odot$). With our values of h_s = 1002 pc and τ_B = 3 we obtain $M_{dust}^{diff} = 3.0 \times 10^6\,M_\odot$, which is twice the mass of the diffuse dust found in NGC 4214. The masses of dust of the SF complexes are $M_{dust}^{EAST} = 0.112 \times 10^6\,M_\odot$, $M_{dust}^{NORTH} = 0.164 \times 10^6\,M_\odot$ and $M_{dust}^{SOUTH} = 0.286 \times 10^6\,M_\odot$. The total mass of dust is thus $M_{dust}^{total} = 3.562 \times 10^6\,M_\odot$, in good agreement with the value $M_{dust} = 3.8 \times 10^6\,M_\odot$

reported by Böttner et al. (2003).

From our modelling, we obtain $G_{dust} = 430$, slightly higher than the upper limit of the expected gas-to-dust ratio. If, as we assumed for NGC 4214, the CO-to-H_2 conversion factor is 10 times the Galactic value, the total mass of gas is $M_{gas} = 1.840 \times 10^9\,M_\odot$ and the gas-to-dust ratio is then $G_{dust} = 484$. For the metallicity of NGC 4449, $Z = 0.45 \pm 0.07\,Z_\odot$, and the Galactic gas-to-dust ratio, $G^\odot = 150$, the expected value of the gas-to-dust ratio is $G^{exp}_{dust} = 288 - 394$.

4.6 Discussion

The analysis presented in the previous sections enables us to draw conclusions about the physical properties of the dwarf galaxies under study. The way this can be achieved is by confirming or rejecting the basic ingredients of the models used to fit the data, from the consistency, between model predictions and data. Since our models are radiative transfer models, they contain a wealth of information regarding the distribution of stars and dust in galaxies, the clumpiness of the ISM, the dust opacity of the dust clouds, the contributions of the different phases of the ISM, and the optical properties of the dust grains, including the relative abundance of PAH molecules.

Although we can fit the FIR SED of these galaxies, the main discrepancy is that the UV emission is underpredicted with respect to our corresponding predictions for attenuation of UV light. We discuss possible causes for this discrepancy, as well as consequences for the derived physical parameters of these galaxies. We also discuss the underprediction of the 8μm emission in the SF regions, and its implications.

4.6.1 Emission from PAHs at 8μm

We found that the observed emission at 8 μm is overpredicted for the diffuse emission, and severely underpredicted for the emission from the HII regions. One reason for this could be, as we discussed in Sect. 4.2.1, that part of the 8μm flux seen in the apertures, although powered by UV light from the star cluster, is actually likely to originate in the diffuse dust layer beyond the PDR+HII region considered by the Groves et al. (2008) model. Although it is impossible to quantify the importance of this effect, we do not think that it is entirely responsible for the discrepancies, because most of the 8 μm emission is clearly associated with the SF regions, as shown by the close correspondence between the 8 μm and Hα distribution (e.g. in the shell structure in the NGC 4214 - NW region.)

The model of Popescu et al. (2011) assumes Galactic dust properties and a fraction of PAHs in dust which is appropriate for our Galaxy. The PAH fraction in NGC 4214 and NGC 4449 might be lower given the lower metallicity (e.g. a lower PAH fraction has been found in the diffuse ISM in the SMC by Sandstrom et al. 2010). If this is the case, we can quantitatively understand the discrepancy.

A possible reason for the excess of 8 μm emission in the HII regions may be that the model of Groves et al. (2008) overpredicts the PAH destruction for these particular objects. In the models of Groves et al. (2008) the PAH abundance is fixed to be proportional to the gas metallicity. In addition to this, it includes a parameter which controls the destruction of the PAHs in intense radiation fields. Thus, this model considers PAH destruction and assumes a lower fraction of PAHs in dust in the SF regions.

Engelbracht et al. (2008) found a good correlation between the equivalent width at 8 μm, EW(8 μm), and the ionization parameter for a set of starburst galaxies. The relation has also been confirmed for HII regions in M101 (Gordon et al., 2008). NGC 4214 and NGC 4449 are part of the sample of galaxies used by Engelbracht et al. (2008). NGC 4214 deviates significantly from this correlation: it exhibits an EW(8 μm) a factor of 3 higher than the one corresponding to the ionization parameter[1]. However, in the case of NGC 4449, for which we obtain a larger discrepancy at 8 μm, Engelbracht et al. (2008) did not report any anomalies.

A final possibility to explain the high 8 μm emission from the SF region is the ratio between neutral and ionized PAHs. The model of Groves et al. (2008) uses templates fitted to the starburst galaxies NGC 4676 and NGC 7252 with a corresponding ratio between neutral and ionized PAHs. This ratio might not be entirely appropriate for the low-metallicity galaxies NGC 4214 and NGC 4449. Ionized PAHs emit about a factor of 10 more energy in the 6-9μm range than at 11-12 μm, whereas neutral PAHs emit about the same amount in both ranges (Draine and Li, 2007). Thus, a higher ionized PAH fraction could boost the predicted emission at 8 μm at the expense of the emission at 11-12 μm. If we assume as an extreme case that the entire emission at 11-12 μm is transferred to the 8 μm band, we can increase the emission for our model spectrum at 8 μm by a factor of ~ 2. Thus, we could indeed improve the agreement between data and model, although some discrepancy would remain, especially for NGC 4449.

---

[1] The spectra used in this analysis are not restricted to the SF regions and thus might contain emission from the diffuse medium (Engelbracht et al. 2008 do not quantify this) and therefore we cannot rigorously compare this result to our findings for the SF complexes. However, since the lines from the ionized atoms and the PAH emission come to a large extent from HII regions and their PDRs (see our Tabs. 1-3) the result of Engelbracht et al. (2008) suggests that the 8 μmemission in the SF regions in NGC 4214 might indeed be high.

4.6.2 The UV emission illuminating the diffuse dust

In Sections 4.4.3 and 4.5.3 we found that there is tension between the observed surface brightness of the disk in the submm and the observed flux of the galaxy in the non-ionising UV in the sense that, although the FIR SED can be fitted, the UV emission required to heat the dust is only a fraction of $\sim$ 40% and $\sim$ 25% of the observed luminosity of NGC 4214 and NGC 4449, respectively. Therefore, in order to match data and model we require that a large fraction of the observed UV-optical luminosity does not contribute to the dust heating, and instead leaves the galaxy unattenuated. Here we discuss the plausibility of such an escape fraction and study further possibilities to explain the differences between model and data.

4.6.2.1 Escape of unattenuated UV radiation

In starburst galaxies, it has been previously observed that a fraction of the UV luminosity can escape from the galaxies without heating the dust, mainly due to the porosity of the ISM created by the energy input of massive stars and SNe which in the extreme case leads to (super)bubbles and galactic winds. Oey et al. (2007) showed that starburst galaxies present a low diffuse Hα emission consistent with an expected escape fraction of ionizing photons of 25% from the galaxy. Other studies show that the escape of ionizing radiation (and therefore non-ionizing as well) could be much lower: Leitherer et al. (1995) pointed out that 3% of the intrinsic LyC photons escape from a set of starburst galaxies; Grimes et al. (2009) found an even lower (<1%) fraction for local starburst galaxies, and Siana et al. (2007) found a low escape fraction for low (subsolar) metallicity starburst galaxies (<8%).

However, the detection of the escaping photons might be determined by the geometry and orientation of the observations if holes and open channels are the medium that the radiation uses to escape from the galaxy (Clarke and Oey 2002, Zastrow et al. 2011). Besides, the escape fraction can be affected by the internal properties of galaxies, depending sensitively on the covering factor of clumps, and the density of the clumped and interclumped medium (Fernandez and Shull 2011).

Conditions that are favorable for an escape are likely to be given in starburst dwarf galaxies which generally show large bubbles and shell structures (Martin, 1998) – similar to what we are seeing in the centres of NGC 4214 and NGC 4449 – that would make the ISM more porous and prone to enable the UV radiation to escape. The simulations of Wise and Cen (2009) showed that an escape fraction as high as 25-80% can be expected due to the irregular morphology of the dwarf galaxies with a clumpy ISM. There are observational confirmations of such an escape. Cormier et al. (2012) found evidence for a escape of 80% of the non-ionizing UV-radiation from the low metallicity Haro 11 and Bergvall et al. (2006) an escape fraction of the Lyman continuum radiation of 4-10% in the same object. Zastrow et al. (2011) have detected an ionized cone above a shell structure in the starburst galaxy NGC 5253 suggesting that ionizing radiation could be escaping from this galaxy. In the presence of such channels we would expect that not only ionizing, but also non-ionizing radiation escape from the galaxies without being affected by dust.

The geometry of the central SF regions of NGC 4214, especially in the case of the NGC 4214 - NW region, suggests that bubbles have been already created in this galaxy. We can make an estimate of how much such a process could affect NGC 4214 by assuming that the entire UV luminosity from these regions leaves the galaxy unattenuated. The UV luminosity of the two main HII regions represent 20% of the total UV luminosity of NGC 4214. Therefore, about 20% of the total UV luminosity possibly does not contribute to the dust heating and should be subtracted when converting into the SFR' heating the dust in the disk. This fraction is close to the lower limit of the observed discrepancy and thus might be able to explain a considerable part of it.

4.6.2.2 A different geometry of dust and stars

In our modeling we have assumed that NGC 4214 and NGC 4449 are a scaled-down version of the model spiral galaxy used in Popescu et al. (2011). However, the differences in the geometry for the spiral and dwarf galaxies can affect the comparison of the data with the model of Popescu et al. (2011).

The relative scale-heights and scale-lengths of the dust and the stars are derived from a sample of edge-on spiral galaxies (Xilouris et al., 1999). However, the geometry of dwarf galaxies is known to be different from that of larger spiral galaxies. In particular, their stellar disks are thicker in comparison to their diameter (e.g. Hunter and Elmegreen, 2006). This is not unexpected because the scale-height depends on the mass surface density, which determines the gravitational potential in the vertical direction and the velocity dispersion. Both are generally similar in dwarf galaxies and in spiral galaxies, therefore the *absolute* value of the vertical scale-height is expected to be similar, and, since they are smaller than spiral galaxies, the ratio between scale-height and scale-length becomes larger. The gas scale-height is even higher in absolute terms than in spiral galaxies (Brinks et al., 2002). Thus, we would expect higher ratios between the vertical scale-heights and the radial scale-lengths than the one assumed in the model. In NGC 4214 Maíz-Apellániz et al. (1999) estimates the vertical stellar scale-height to be about 200 pc, i.e. about 1/4 to 1/5 of the radial scale-length. This is at least a factor of 3 higher than the ratio assumed in the Popescu et al. (2011) model. However, the effects of a difference in the ratio between scale-height and scale-length are not expected to be very large as long as the relative scale ratios between stars and dust are the same.

Another possible, albeit speculative, difference between the model and the real geometry could be a non-central position of the SF regions. Since these regions are dominating the young SF activity in the galaxy and are very likely responsible for a large fraction of the UV emission, their possible position above or below the galactic disk would have an important impact on the dust heating, whereas in large galaxies such an asymmetry is unlikely due to the high number of SF regions.

4.6.2.3 An extended dust component

If the dust is more extended compared to the stellar disk than what is assumed in the model, such an extended dust component will be relatively cold and emit more in the submillimeter. By including such a component we would therefore be able to use a higher value of SFR' for the rest of the dust and decrease the discrepancy with the observed UV emission. Furthermore, an extended, cold dust component could explain the missing flux at the long wavelengths. Popescu et al. (2002) have found indications of such an extended dust component with ISO data in dwarf galaxies, however their data lacked the spatial resolution to directly measure its spatial extent. In order to test whether there are indications for an extended dust component, we derived the radial scale-lengths from SPIRE 250, 350 and 500μm bands. The rather irregular distribution of the dust emission did not allow us to define elliptical isophotes at all galactocentric radii, instead we derived the median values with the isophotal elliptic annuli defined in the g-band image. By carrying out a least square-fit to the radial distribution of these median values, we derived scale-lengths of 835, 920 and 1067 pc for NGC 4214 and of 1042, 1073 and 1118 pc for NGC 4449 at the SPIRE 250, 350 and 500 μm bands (see Figure 4.22), respectively. The increase of the scale-lengths from shorter to longer wavelengths is expected because of the decrease of the dust temperature towards the outer parts of the galaxy. The longest wavelength (SPIRE 500 μm) best represents the scale-length of the dust distribution but most likely still underestimates it.

The model of Popescu et al. (2011) adopts a dust scale-length of $1.406 \times h_{\rm s}$. In the case of NGC 4214, with $h_{\rm s} = 873\,{\rm pc}$ this would predict a dust scale-length of 1227 pc, whereas in the case of NGC 4449, with $h_{\rm s} = 1002\,{\rm pc}$, the prediction is 1409 pc. Thus, in both cases, the predicted value of the dust scale-length is higher than the measured scale-length at SPIRE 500 μm band. Therefore, although we cannot exclude the presence of an extended dust component because the dust scale-length can be longer than that at SPIRE 500 μm band, we do not find any clear evidence for its presence.

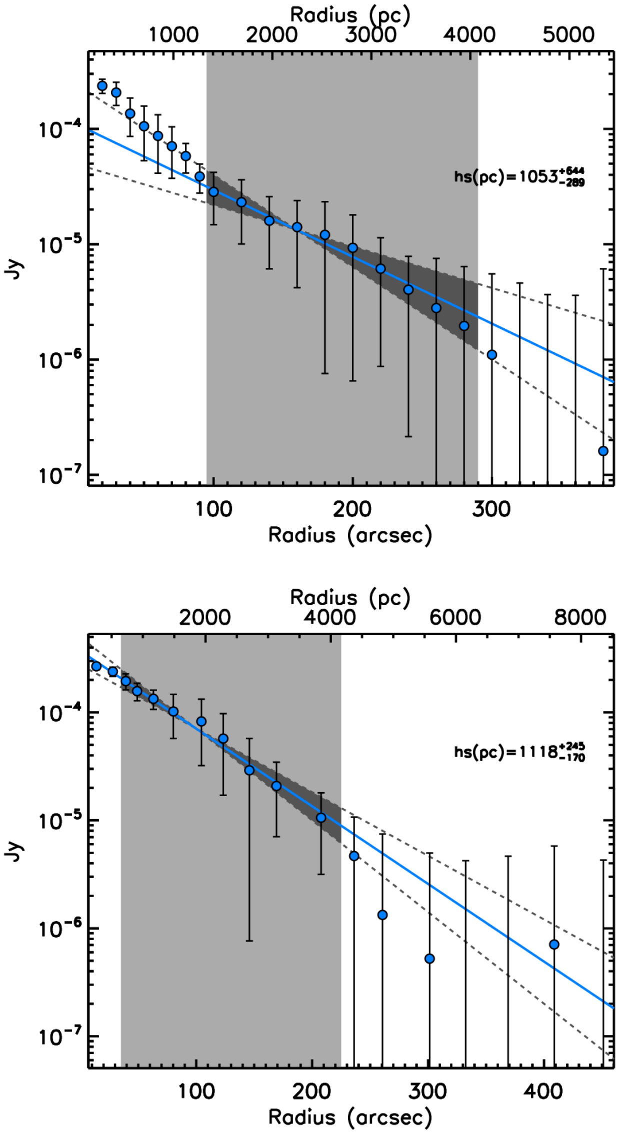

Figure 4.22: SPIRE 500 μm scale-length of NGC 4214 (top) and NGC 4449 (bottom). The fit (solid line) was achieved using the isophotes in the radial range marked by the grey-shaded area. The uncertainty in the slope is represented by the dark grey area and the dark grey dashed lines.

4.6.2.4 Different dust properties

Until now we have mainly discussed different geometrical scenarios for explaining the discrepancies we find in the UV. There is however another possibility, that the submm mass absorption coefficient of grains, as specified by the Weingartner and Draine (2001) model and as used in the radiation transfer model of Popescu et al. (2011), underestimates the true mass absorption coefficient of the grains in the submm, leading to a lower dust surface densities and a lower disk opacity in the UV for the observed submm brightness of the diffuse disk. This is a solution that unfortunately is largely degenerate with the assumed geometry of stars and dust. Because of this, and the lack of independent constraints on the existence of such a dust model, we cannot draw any conclusion on this issue.

4.6.2.5 Physical implications

In the previous subsections we discussed a few possibilities that might have caused the discrepancy in the predicted level of UV emission. Probably the most likely scenario is that dynamical effects associated with a recent burst of SF activity responsible for the central SF complexes has punched holes through the diffuse dust layer, through which the UV photons leaving the SF regions can escape the galaxy without interacting with the diffuse dust. This would be a natural outcome of a non-steady state behaviour of SF activity in dwarf galaxies, in which we may be observing NGC 4214 and NGC 4449 in a post starburst phase, where the star clusters are no longer fully cocooned by dust, but to the contrary have evolved to the point where SN and wind activity have cleared the dust in the ISM above the location of the starburst.

The existence of different grain properties is also plausible, though difficult to distinguish from the other scenarios. This would increase the inferred gas-to-dust mass ratios compared to the radiation transfer model predictions, bringing it closer to the values expected from the observed metallicity of NGC 4214 and NGC 4449.

CHAPTER 5

Conclusions and Future Work

”Extraordinary claims require extraordinary evidence”

– Carl Edward Sagan (*Cosmos*)

We carried out a study of the interstellar dust in starbursting dwarf galaxies from both the perspective of the extinction and the emission of dust grains. We chose this kind of objects because they are simple systems driven by a few star forming regions that dominate the emission and because their dust properties have been a matter of debate over the last decade. In order to be able to study separately the different components of the ISM, we chose the two nearby galaxies NGC 4214 and NGC 4449.

For our study of the extinction we made use of the HST-WFC3 observations of NGC 4214, which cover a broad spectral range from the near-ultraviolet to the near-infrared, including the Hydrogen recombination lines Hβ, Hα and Pβ. We used these three line-emission maps to compute the dust extinction in the central photo-ionised regions of NGC 4214.

To derive the extinction we assumed that the dust is distributed in a foreground screen far from the emitting gas. Regarding the dust geometry, we tested two different extinction laws, the first with $\mathrm{R_V} = 3.10$ (typical of dust in the diffuse ISM) and the second with $\mathrm{R_V} = 5.45$ (more appropriated for dust in molecular clouds). Our main conclusions from this study are listed in the following:

- Extinction maps calculated with different line-ratios show similar structures but they predict different values of the extinction. Specifically, in those regions that present low values of the extinction, the correlation between the different extinction maps is linear. On the other hand, regions with a high extinction show a clear deviation from the linearity.

- For all of the derived maps, these correlations are closer to linearity for $R_V = 5.45$, which indicates the presence of dust as in molecular clouds in our line of sight.
- In general, we found that $A^{P\beta/H\alpha} > A^{P\beta/H\beta} > A^{H\alpha/H\beta}$. This trend can only be understood if scattering is playing an important role in bringing back photons to our line of sight. This indicates that part of the dust that produces the extinction is located close to the ionised gas.
- Based on our high resolution maps, we believe that the most plausible geometrical scenario is that dust is distributed in dense clumps located close to the emitting gas.

In summary, we found that a fraction of the dust that produces the extinction in our line of sight must be dust within molecular clouds most likely distributed in dense clumps located close to the source of radiation, which physically would correspond to a fragmented PDR.

For our study of the dust emission we have the SED of NGC 4214 and NGC 4449 from the UV to radio wavelengths. We used two radiation transfer models to study separately the emission from the star forming regions and from the diffuse dust. The large amount and quality of ancillary data, as well as the results from previous studies, allowed us to constrain a major part of the input parameters of the models. Our main conclusion are:

- In general, we achieved a good agreement between data and models, both for the diffuse dust emission and the dust in HII+PDR regions.
- We found that the emission from PAHs is severely underestimated in the SF regions. Possible reasons for this discrepancy are that the model assumptions (PAH abundance and destruction) are not completely adequate for the cases of NGC 4214 and NGC 4449 or that these galaxies have an unusually high emission at $8\,\mu$m for their metallicities and radiation field, which in the case of NGC 4214 is supported by other studies.
- For both galaxies, we could fit the diffuse dust SED satisfactorily, and we derived global gas-to-dust mass ratios compatible with their expected values from their metallicities.
- We did not find strong evidence of the submm excess usually found in dwarf galaxies.
- Our results does not show clear evidence of the need of different dust properties as it was proposed by several authors.
- We inferred that the UV radiation field needed to power the observed dust emission is only a fraction ($\sim$ 40% for NGC 4214 and $\sim$ 25% for NGC 4449) of the UV radiation field observed. We discussed different explanations for this discrepancy and conclude that the most plausible one is that a large fraction of the UV radiation escapes from the

galaxy unattenuated.

This is the first time a full radiation transfer analysis constrained by the observed SEDs of spatially separated components has been done for dwarf galaxies. Corresponding radiation transfer studies of resolved star-forming dwarf galaxies but with different inclinations and evolutionary states to NGC 4214 and NGC 4449 may allow to explore in more detail the question of the submm excess and the escape of UV radiation.

Due to their close location, the Magellanic Clouds are excellent targets for understanding the dust properties of dwarf irregular galaxies. The Large and the Small Magellanic Clouds (located at a distance of 50 and 62 kpc, respectively) span many degrees on the sky due to their proximity to the Milky Way. In Figures 5.1 and 5.2 the size of the LMC and SMC, respectively, can be compared with the size of NGC 4214 and NGC 4449. It is clear from these figures the advantage of the Magellanic Clouds, even the smaller HII regions within these two galaxies have similar sizes to the whole disk of NGC 4214 and NGC 4449!

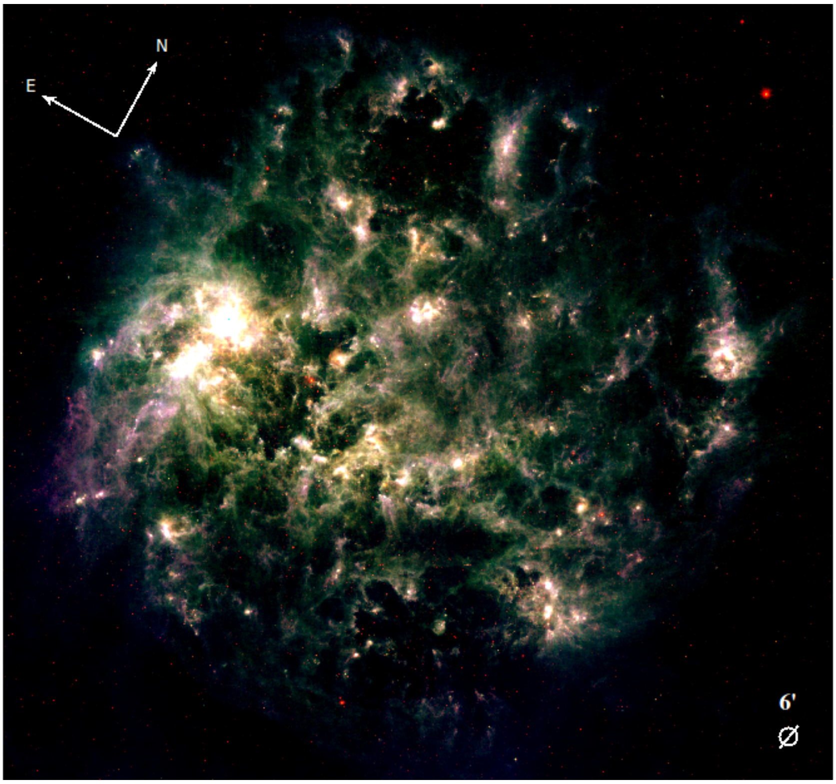

Figure 5.1: Image of LMC from a RGB combination of MIPS 160 μm, MIPS 70 μm and MIPS 24 μm bands from the SAGE survey. The small circle at the right bottom corner has a diameter of 6′, i.e., the same diameter of NGC 4214 and NGC 4449.

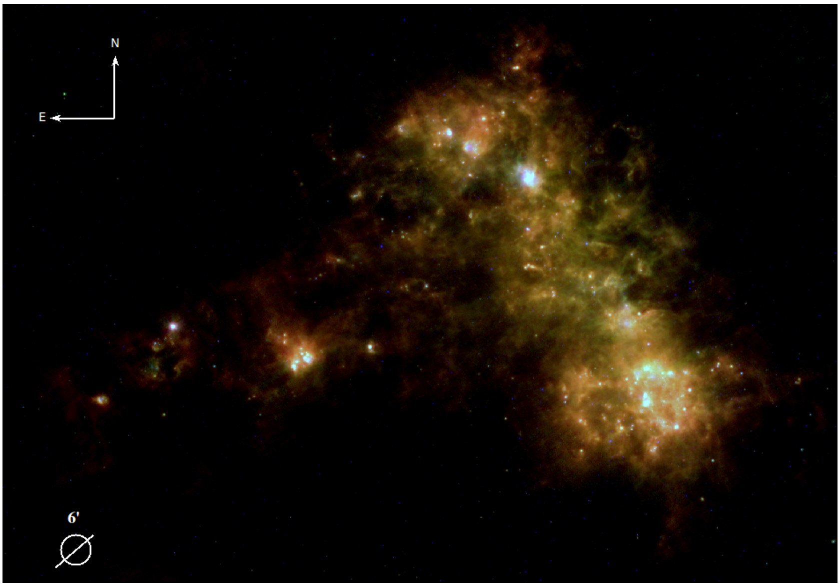

Figure 5.2: Image of SMC from a RGB combination of MIPS 160 μm, MIPS 70 μm and MIPS 24 μm bands from the SAGE survey. The small circle at the left bottom corner has a diameter of $6'$, i.e., the same diameter of NGC 4214 and NGC 4449.

Both Magellanic Clouds were mapped by the program "Surveying the Agents of Galaxy Evolution" (SAGE) with all Spitzer IRAC and MIPS bands. Their mosaics of the LMC ($\sim 7 \times 7$ degrees) and of the SMC ($\sim 9 \times 5$ degrees) cover the whole disk of both galaxies. This data is already public.

The SAGE program is currently being extended with the program "Herschel Inventory of The Agents of Galaxy Evolution" (HERITAGE), which is mapping the Magellanic Clouds with Herschel PACS and SPIRE data from April 2012.

In Figure 5.3 we show the intensity maps from Planck presented in Planck Collaboration et al. (2011a). Whereas for NGC 4214 and NGC 4449 the resolution achieved by Planck does not allow to resolve the SF regions, in the case of the Magellanic Clouds it allows to perform a detailed separation. Besides, unlike NGC 4214 and NGC 4449, Planck successfully detected LMC and SMC in all their bands, which will allow us to perform a detailed study in the submm range. This data is not public yet.

In summary, the proximity of the Magellanic Clouds will allow us to perform a clearer separation between HII regions and the diffuse medium and to carry out a much more detailed study of the submm SED than the performed in the present work.

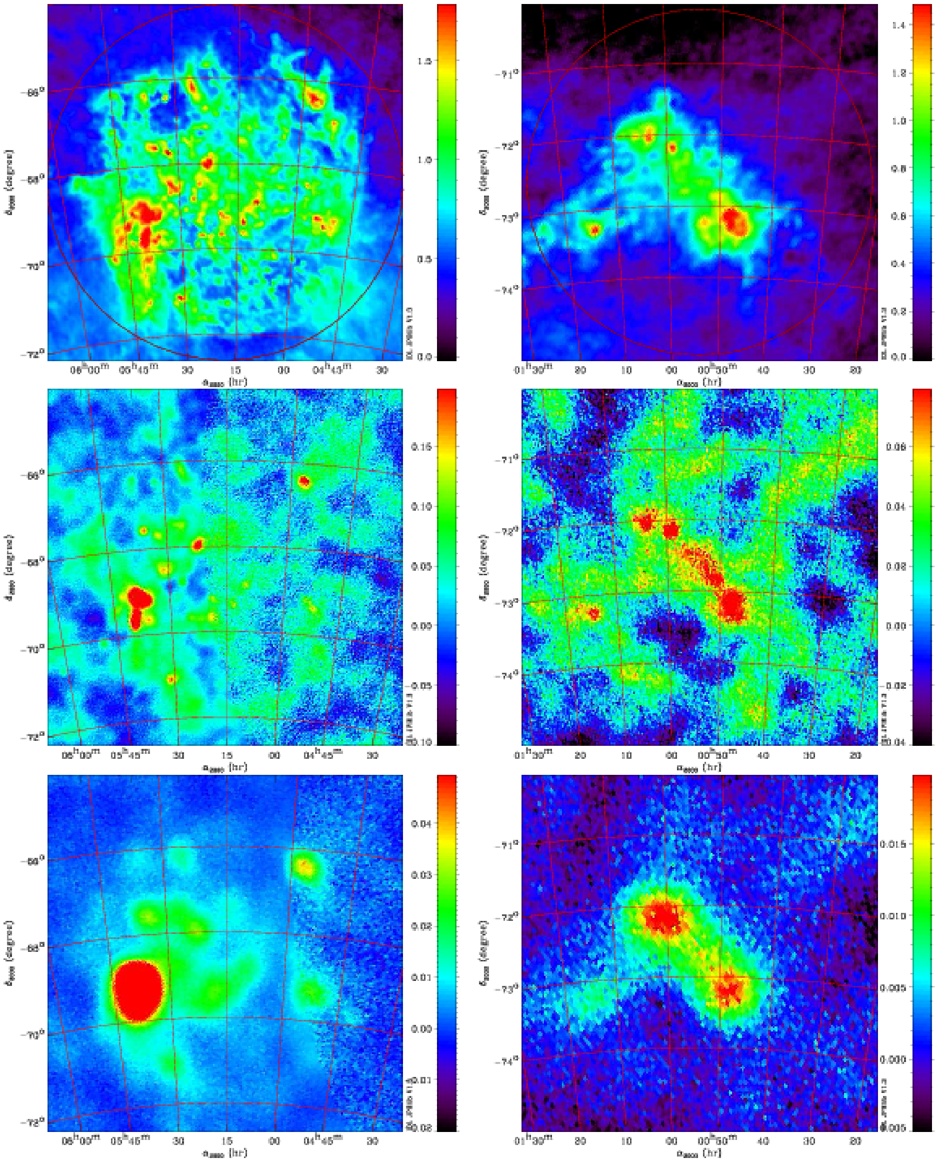

Figure 5.3: PLANCK 350 μm (top), PLANCK 3 000 μm (middle) and PLANCK 10 000 μm (bottom) view of the LMC (left) and of the SMC (right). Image extracted from Planck Collaboration et al. (2011a).

List of Figures

List of Tables

Bibliography

F. Annibali, A. Aloisi, J. Mack, M. Tosi, R. P. van der Marel, L. Angeretti, C. Leitherer, and M. Sirianni. Starbursts in the Local Universe: New Hubble Space Telescope Advanced Camera for Surveys Observations of the Irregular Galaxy NGC 4449. *AJ*, 135:1900–1916, May 2008. doi: 10.1088/0004-6256/135/5/1900. 16, 17

M. Asplund, N. Grevesse, and A. J. Sauval. The Solar Chemical Composition. In T. G. Barnes, III and F. N. Bash, editors, *Cosmic Abundances as Records of Stellar Evolution and Nucleosynthesis*, volume 336 of *Astronomical Society of the Pacific Conference Series*, page 25, September 2005. 17

M. Baes, J. Fritz, D. A. Gadotti, D. J. B. Smith, L. Dunne, E. da Cunha, A. Amblard, R. Auld, G. J. Bendo, D. Bonfield, D. Burgarella, S. Buttiglione, A. Cava, D. Clements, A. Cooray, A. Dariush, G. de Zotti, S. Dye, S. Eales, D. Frayer, J. Gonzalez-Nuevo, D. Herranz, E. Ibar, R. Ivison, G. Lagache, L. Leeuw, M. Lopez-Caniego, M. Jarvis, S. Maddox, M. Negrello, M. Michałowski, E. Pascale, M. Pohlen, E. Rigby, G. Rodighiero, S. Samui, S. Serjeant, P. Temi, M. Thompson, P. van der Werf, A. Verma, and C. Vlahakis. Herschel-ATLAS: The dust energy balance in the edge-on spiral galaxy UGC 4754. *A&A*, 518:L39, July 2010. doi: 10.1051/0004-6361/201014644. 47

M. Baes, J. Verstappen, I. De Looze, J. Fritz, W. Saftly, E. Vidal Pérez, M. Stalevski, and S. Valcke. Efficient Three-dimensional NLTE Dust Radiative Transfer with SKIRT. *ApJS*, 196:22, October 2011. doi: 10.1088/0067-0049/196/2/22. 47

G. J. Bendo, D. A. Dale, B. T. Draine, C. W. Engelbracht, R. C. Kennicutt, Jr., D. Calzetti, K. D. Gordon, G. Helou, D. Hollenbach, A. Li, E. J. Murphy, M. K. M. Prescott, and J.-D. T. Smith. The Spectral Energy Distribution of Dust Emission in the Edge-on Spiral

Galaxy NGC 4631 as Seen with Spitzer and the James Clerk Maxwell Telescope. *ApJ*, 652:283–305, November 2006. doi: 10.1086/508057. 15

N. Bergvall, E. Zackrisson, B.-G. Andersson, D. Arnberg, J. Masegosa, and G. Östlin. First detection of Lyman continuum escape from a local starburst galaxy. I. Observations of the luminous blue compact galaxy Haro 11 with the Far Ultraviolet Spectroscopic Explorer (FUSE). *A&A*, 448:513–524, March 2006. doi: 10.1051/0004-6361:20053788. 97

S. Bianchi. Dust extinction and emission in a clumpy galactic disk. An application of the radiative transfer code TRADING. *A&A*, 490:461–475, October 2008. doi: 10.1051/0004-6361:200810027. 47

C. Bot, N. Ysard, D. Paradis, J. P. Bernard, G. Lagache, F. P. Israel, and W. F. Wall. Submillimeter to centimeter excess emission from the Magellanic Clouds. II. On the nature of the excess. *A&A*, 523:A20, November 2010. doi: 10.1051/0004-6361/201014986. 15

C. Böttner, U. Klein, and A. Heithausen. Cold dust and its relation to molecular gas in the dwarf irregular galaxy ¡ASTROBJ¿NGC 4449¡/ASTROBJ¿. *A&A*, 408:493–498, September 2003. doi: 10.1051/0004-6361:20031009. 61, 68, 74, 93, 94, 95

E. Brinks, F. Walter, and J. Ott. Bloated Dwarfs: The Thickness of the HI Disks in Irregular Galaxies. In E. Athanassoula, A. Bosma, & R. Mujica, editor, *Disks of Galaxies: Kinematics, Dynamics and Peturbations*, volume 275 of *Astronomical Society of the Pacific Conference Series*, pages 57–60, December 2002. 98

G. Bruzual A., G. Magris, and N. Calvet. A model for the effects of dust on the spectra of disk galaxies. I - General treatment. *ApJ*, 333:673–688, October 1988. doi: 10.1086/166776. 9

D. Calzetti, A. L. Kinney, and T. Storchi-Bergmann. Dust extinction of the stellar continua in starburst galaxies: The ultraviolet and optical extinction law. *ApJ*, 429:582–601, July 1994. doi: 10.1086/174346. 34, 35, 40, 41, 42

J. Caplan and L. Deharveng. Extinction and reddening of H II regions in the Large Magellanic Cloud. *A&A*, 155:297–313, February 1986. 34

J. A. Cardelli, G. C. Clayton, and J. S. Mathis. The relationship between infrared, optical, and ultraviolet extinction. *ApJ*, 345:245–256, October 1989. doi: 10.1086/167900. 10, 11, 12, 22, 23, 30, 42, 109

J. Castor, R. McCray, and R. Weaver. Interstellar bubbles. *ApJ*, 200:L107–L110, September 1975. doi: 10.1086/181908. 52

G. Chlewicki and J. Mayo Greenberg. General constraints on the average scattering characteristics of interstellar grains in the ultraviolet. *MNRAS*, 210:791–801, October 1984. 8, 9

K. T. Chyży, R. Beck, S. Kohle, U. Klein, and M. Urbanik. Regular magnetic fields in the dwarf irregular galaxy NGC 4449. *A&A*, 355:128–137, March 2000. 61

C. Clarke and M. S. Oey. Galactic porosity and a star formation threshold for the escape of ionizing radiation from galaxies. *MNRAS*, 337:1299–1308, December 2002. doi: 10.1046/j.1365-8711.2002.05976.x. 97

J. J. Condon. Radio emission from normal galaxies. *ARA&A*, 30:575–611, 1992. doi: 10.1146/annurev.aa.30.090192.003043. 61

D. Cormier, S. C. Madden, S. Hony, A. Contursi, A. Poglitsch, F. Galliano, E. Sturm, V. Doublier, H. Feuchtgruber, M. Galametz, N. Geis, J. de Jong, K. Okumura, P. Panuzzo, and M. Sauvage. The effects of star formation on the low-metallicity ISM: NGC 4214 mapped with Herschel/PACS spectroscopy. *A&A*, 518:L57, July 2010. doi: 10.1051/0004-6361/201014699. 73, 88

D. Cormier, V. Lebouteiller, S. C. Madden, N. Abel, S. Hony, F. Galliano, M. Baes, M. J. Barlow, A. Cooray, I. De Looze, M. Galametz, O. L. Karczewski, T. J. Parkin, A. Remy, M. Sauvage, L. Spinoglio, C. D. Wilson, and R. Wu. The nature of the interstellar medium of the starburst low-metallicity galaxy Haro11: a multi-phase model of the infrared emission. *ArXiv e-prints*, September 2012. 97

E. da Cunha, S. Charlot, and D. Elbaz. A simple model to interpret the ultraviolet, optical and infrared emission from galaxies. *MNRAS*, 388:1595–1617, August 2008. doi: 10.1111/j.1365-2966.2008.13535.x. 47

J. J. Dalcanton, B. F. Williams, A. C. Seth, A. Dolphin, J. Holtzman, K. Rosema, E. D. Skillman, A. Cole, L. Girardi, S. M. Gogarten, I. D. Karachentsev, K. Olsen, D. Weisz, C. Christensen, K. Freeman, K. Gilbert, C. Gallart, J. Harris, P. Hodge, R. S. de Jong, V. Karachentseva, M. Mateo, P. B. Stetson, M. Tavarez, D. Zaritsky, F. Governato, and T. Quinn. The ACS Nearby Galaxy Survey Treasury. *ApJS*, 183:67–108, July 2009. doi: 10.1088/0067-0049/183/1/67. 58

D. A. Dale, G. Helou, A. Contursi, N. A. Silbermann, and S. Kolhatkar. The Infrared Spectral Energy Distribution of Normal Star-forming Galaxies. *ApJ*, 549:215–227, March 2001. doi: 10.1086/319077. 47

D. A. Dale, S. A. Cohen, L. C. Johnson, M. D. Schuster, D. Calzetti, C. W. Engelbracht, A. Gil de Paz, R. C. Kennicutt, J. C. Lee, A. Begum, M. Block, J. J. Dalcanton, J. G. Funes, K. D. Gordon, B. D. Johnson, A. R. Marble, S. Sakai, E. D. Skillman, L. van

Zee, F. Walter, D. R. Weisz, B. Williams, S.-Y. Wu, and Y. Wu. The Spitzer Local Volume Legacy: Survey Description and Infrared Photometry. *ApJ*, 703:517–556, September 2009. doi: 10.1088/0004-637X/703/1/517. 58

D. A. Dale, G. Aniano, C. W. Engelbracht, J. L. Hinz, O. Krause, E. J. Montiel, H. Roussel, P. N. Appleton, L. Armus, P. Beirão, A. D. Bolatto, B. R. Brandl, D. Calzetti, A. F. Crocker, K. V. Croxall, B. T. Draine, M. Galametz, K. D. Gordon, B. A. Groves, C.-N. Hao, G. Helou, L. K. Hunt, B. D. Johnson, R. C. Kennicutt, J. Koda, A. K. Leroy, Y. Li, S. E. Meidt, A. E. Miller, E. J. Murphy, N. Rahman, H.-W. Rix, K. M. Sandstrom, M. Sauvage, E. Schinnerer, R. A. Skibba, J.-D. T. Smith, F. S. Tabatabaei, F. Walter, C. D. Wilson, M. G. Wolfire, and S. Zibetti. Herschel Far-infrared and Submillimeter Photometry for the KINGFISH Sample of nearby Galaxies. *ApJ*, 745:95, January 2012. doi: 10.1088/0004-637X/745/1/95. 15, 75

G. de Vaucouleurs, A. de Vaucouleurs, H. G. Corwin, Jr., R. J. Buta, G. Paturel, and P. Fouque. Book-Review - Third Reference Catalogue of Bright Galaxies. *S&T*, 82:621, December 1991a. 16, 21

G. de Vaucouleurs, A. de Vaucouleurs, H. G. Corwin, Jr., R. J. Buta, G. Paturel, and P. Fouqué. *Third Reference Catalogue of Bright Galaxies. Volume I: Explanations and references. Volume II: Data for galaxies between* 0^h *and* 12^h*. Volume III: Data for galaxies between* 12^h *and* 24^h*.* 1991b. 82

B. T. Draine. Interstellar Dust. *Origin and Evolution of the Elements*, page 317, 2004. 14

B. T. Draine and B. Hensley. The Submm and mm Excess of the SMC: Magnetic Dipole Emission from Magnetic Nanoparticles? *ArXiv e-prints*, May 2012. 15

B. T. Draine and A. Lazarian. Electric Dipole Radiation from Spinning Dust Grains. *ApJ*, 508:157–179, November 1998. doi: 10.1086/306387. 15

B. T. Draine and A. Li. Infrared Emission from Interstellar Dust. IV. The Silicate-Graphite-PAH Model in the Post-Spitzer Era. *ApJ*, 657:810–837, March 2007. doi: 10.1086/511055. 48, 96

B. T. Draine, D. A. Dale, G. Bendo, K. D. Gordon, J. D. T. Smith, L. Armus, C. W. Engelbracht, G. Helou, R. C. Kennicutt, Jr., A. Li, H. Roussel, F. Walter, D. Calzetti, J. Moustakas, E. J. Murphy, G. H. Rieke, C. Bot, D. J. Hollenbach, K. Sheth, and H. I. Teplitz. Dust Masses, PAH Abundances, and Starlight Intensities in the SINGS Galaxy Sample. *ApJ*, 663:866–894, July 2007. doi: 10.1086/518306. 14, 47

C. W. Engelbracht, M. Blaylock, K. Y. L. Su, J. Rho, G. H. Rieke, J. Muzerolle, D. L. Padgett, D. C. Hines, K. D. Gordon, D. Fadda, A. Noriega-Crespo, D. M. Kelly, W. B. Latter, J. L.

Hinz, K. A. Misselt, J. E. Morrison, J. A. Stansberry, D. L. Shupe, S. Stolovy, W. A. Wheaton, E. T. Young, G. Neugebauer, S. Wachter, P. G. Pérez-González, D. T. Frayer, and F. R. Marleau. Absolute Calibration and Characterization of the Multiband Imaging Photometer for Spitzer. I. The Stellar Calibrator Sample and the 24 μm Calibration. *PASP*, 119:994–1018, September 2007. doi: 10.1086/521881. 59

C. W. Engelbracht, G. H. Rieke, K. D. Gordon, J.-D. T. Smith, M. W. Werner, J. Moustakas, C. N. A. Willmer, and L. Vanzi. Metallicity Effects on Dust Properties in Starbursting Galaxies. *ApJ*, 678:804–827, May 2008. doi: 10.1086/529513. iv, viii, 14, 96

G. Fazio and M. Pahre. A Mid-IR Hubble Atlas of Galaxies. In *Spitzer Proposal ID #69*, page 69, September 2004. 59

G. G. Fazio, J. L. Hora, L. E. Allen, M. L. N. Ashby, P. Barmby, L. K. Deutsch, J.-S. Huang, S. Kleiner, M. Marengo, S. T. Megeath, G. J. Melnick, M. A. Pahre, B. M. Patten, J. Polizotti, H. A. Smith, R. S. Taylor, Z. Wang, S. P. Willner, W. F. Hoffmann, J. L. Pipher, W. J. Forrest, C. W. McMurty, C. R. McCreight, M. E. McKelvey, R. E. McMurray, D. G. Koch, S. H. Moseley, R. G. Arendt, J. E. Mentzell, C. T. Marx, P. Losch, P. Mayman, W. Eichhorn, D. Krebs, M. Jhabvala, D. Y. Gezari, D. J. Fixsen, J. Flores, K. Shakoorzadeh, R. Jungo, C. Hakun, L. Workman, G. Karpati, R. Kichak, R. Whitley, S. Mann, E. V. Tollestrup, P. Eisenhardt, D. Stern, V. Gorjian, B. Bhattacharya, S. Carey, B. O. Nelson, W. J. Glaccum, M. Lacy, P. J. Lowrance, S. Laine, W. T. Reach, J. A. Stauffer, J. A. Surace, G. Wilson, E. L. Wright, A. Hoffman, G. Domingo, and M. Cohen. The Infrared Array Camera (IRAC) for the Spitzer Space Telescope. *ApJS*, 154:10–17, September 2004. doi: 10.1086/422843. 59

E. R. Fernandez and J. M. Shull. The Effect of Galactic Properties on the Escape Fraction of Ionizing Photons. *ApJ*, 731:20, April 2011. doi: 10.1088/0004-637X/731/1/20. 97

A. Ferrara and R.-J. Dettmar. Radio-emitting dust in the free electron layer of spiral galaxies: Testing the disk/halo interface. *ApJ*, 427:155–159, May 1994. doi: 10.1086/174128. 15

A. S. Fruchter and R. N. Hook. Drizzle: A Method for the Linear Reconstruction of Undersampled Images. *PASP*, 114:144–152, February 2002. doi: 10.1086/338393. 24

M. Galametz, S. Madden, F. Galliano, S. Hony, F. Schuller, A. Beelen, G. Bendo, M. Sauvage, A. Lundgren, and N. Billot. Probing the dust properties of galaxies up to submillimetre wavelengths. I. The spectral energy distribution of dwarf galaxies using LABOCA. *A&A*, 508:645–664, December 2009. doi: 10.1051/0004-6361/200912963. 15, 47

M. Galametz, S. C. Madden, F. Galliano, S. Hony, G. J. Bendo, and M. Sauvage. Probing the dust properties of galaxies up to submillimetre wavelengths. II. Dust-to-gas mass ratio trends with metallicity and the submm excess in dwarf galaxies. *A&A*, 532:A56, August 2011. doi: 10.1051/0004-6361/201014904. 15, 47

F. Galliano, S. C. Madden, A. P. Jones, C. D. Wilson, J.-P. Bernard, and F. Le Peintre. ISM properties in low-metallicity environments. II. The dust spectral energy distribution of NGC 1569. *A&A*, 407:159–176, August 2003. doi: 10.1051/0004-6361:20030814. 15

F. Galliano, S. C. Madden, A. P. Jones, C. D. Wilson, and J.-P. Bernard. ISM properties in low-metallicity environments. III. The spectral energy distributions of II Zw 40, He 2-10 and NGC 1140. *A&A*, 434:867–885, May 2005. doi: 10.1051/0004-6361:20042369. 15

F. Galliano, E. Dwek, and P. Chanial. Stellar Evolutionary Effects on the Abundances of Polycyclic Aromatic Hydrocarbons and Supernova-Condensed Dust in Galaxies. *ApJ*, 672: 214–243, January 2008. doi: 10.1086/523621. 14

F. Galliano, S. Hony, J.-P. Bernard, C. Bot, S. C. Madden, J. Roman-Duval, M. Galametz, A. Li, M. Meixner, C. W. Engelbracht, V. Lebouteiller, K. Misselt, E. Montiel, P. Panuzzo, W. T. Reach, and R. Skibba. Non-standard grain properties, dark gas reservoir, and extended submillimeter excess, probed by Herschel in the Large Magellanic Cloud. *A&A*, 536:A88, December 2011. doi: 10.1051/0004-6361/201117952. 89

K. D. Gordon, C. W. Engelbracht, G. H. Rieke, K. A. Misselt, J.-D. T. Smith, and R. C. Kennicutt, Jr. The Behavior of the Aromatic Features in M101 H II Regions: Evidence for Dust Processing. *ApJ*, 682:336–354, July 2008. doi: 10.1086/589567. 96

P. Gratier, J. Braine, N. J. Rodriguez-Fernandez, F. P. Israel, K. F. Schuster, N. Brouillet, and E. Gardan. The molecular interstellar medium of the Local Group dwarf NGC 6822. The molecular ISM of NGC 6822. *A&A*, 512:A68, March 2010. doi: 10.1051/0004-6361/200911722. 89

E. K. Grebel. Star Formation Histories of Nearby Dwarf Galaxies. *Astrophysics and Space Science Supplement*, 277:231–239, 2001. doi: 10.1023/A:1012742903265. 13

J. P. Grimes, T. Heckman, A. Aloisi, D. Calzetti, C. Leitherer, C. L. Martin, G. Meurer, K. Sembach, and D. Strickland. Observations of Starburst Galaxies With Far-Ultraviolet Spectrographic Explorer: Galactic Feedback in the Local Universe. *ApJS*, 181:272–320, March 2009. doi: 10.1088/0067-0049/181/1/272. 97

M. Grossi, L. K. Hunt, S. Madden, C. Vlahakis, D. J. Bomans, M. Baes, G. J. Bendo, S. Bianchi, A. Boselli, M. Clemens, E. Corbelli, L. Cortese, A. Dariush, J. I. Davies, I. de Looze, S. di Serego Alighieri, D. Fadda, J. Fritz, D. A. Garcia-Appadoo, G. Gavazzi, C. Giovanardi, T. M. Hughes, A. P. Jones, D. Pierini, M. Pohlen, S. Sabatini, M. W. L. Smith, J. Verstappen, E. M. Xilouris, and S. Zibetti. The Herschel Virgo Cluster Survey. V.

Star-forming dwarf galaxies - dust in metal-poor environments. *A&A*, 518:L52, July 2010. doi: 10.1051/0004-6361/201014653. 15

B. Groves, M. A. Dopita, R. S. Sutherland, L. J. Kewley, J. Fischera, C. Leitherer, B. Brandl, and W. van Breugel. Modeling the Pan-Spectral Energy Distribution of Starburst Galaxies. IV. The Controlling Parameters of the Starburst SED. *ApJS*, 176:438–456, June 2008. doi: 10.1086/528711. iii, vii, 17, 48, 52, 53, 71, 76, 95, 96, 110

T. M. Heckman. Starbursts: Lessons for the Origin and Evolution of Galaxies and the Intergalactic Medium. In C. E. Woodward, J. M. Shull, and H. A. Thronson, Jr., editors, *Origins*, volume 148 of *Astronomical Society of the Pacific Conference Series*, page 127, 1998. 14

G. Helou, H. Roussel, P. Appleton, D. Frayer, S. Stolovy, L. Storrie-Lombardi, R. Hurt, P. Lowrance, D. Makovoz, F. Masci, J. Surace, K. D. Gordon, A. Alonso-Herrero, C. W. Engelbracht, K. Misselt, G. Rieke, M. Rieke, S. P. Willner, M. Pahre, M. L. N. Ashby, G. G. Fazio, and H. A. Smith. The Anatomy of Star Formation in NGC 300. *ApJS*, 154: 253–258, September 2004. doi: 10.1086/422640. 59

D. J. Hollenbach and A. G. G. M. Tielens. Photodissociation regions in the interstellar medium of galaxies. *Reviews of Modern Physics*, 71:173–230, January 1999. doi: 10.1103/RevModPhys.71.173. 3

D. Hunter. Star Formation in Irregular Galaxies: A Review of Several Key Questions. *PASP*, 109:937–950, September 1997. doi: 10.1086/133965. 18

D. A. Hunter and B. G. Elmegreen. Broadband Imaging of a Large Sample of Irregular Galaxies. *ApJS*, 162:49–79, January 2006. doi: 10.1086/498096. 98

D. A. Hunter, E. M. Wilcots, H. van Woerden, J. S. Gallagher, and S. Kohle. The Nature of the Extended H i Gas around NGC 4449: The Dr. Jekyll/Mr. Hyde of Irregular Galaxies. *ApJ*, 495:L47, March 1998. doi: 10.1086/311213. 18

J. B. Irwin. Astronomy. (Book Reviews: Nebulae and Interstellar Matter). *Science*, 162: 554–555, November 1968. 27

F. P. Israel. H_2 and its relation to CO in the LMC and other magellanic irregular galaxies. *A&A*, 328:471–482, December 1997. 88

F. P. Israel, W. F. Wall, D. Raban, W. T. Reach, C. Bot, J. B. R. Oonk, N. Ysard, and J. P. Bernard. submillimeter to centimeter excess emission from the Magellanic Clouds. I. Global spectral energy distribution. *A&A*, 519:A67, September 2010. doi: 10.1051/0004-6361/201014073. 15

T. H. Jarrett, T. Chester, R. Cutri, S. E. Schneider, and J. P. Huchra. The 2MASS Large Galaxy Atlas. *AJ*, 125:525–554, February 2003. doi: 10.1086/345794. 82

I. D. Karachentsev, V. E. Karachentseva, W. K. Huchtmeier, and D. I. Makarov. A Catalog of Neighboring Galaxies. *AJ*, 127:2031–2068, April 2004. doi: 10.1086/382905. 16

A. A. Kepley, E. G. Zweibel, E. M. Wilcots, K. E. Johnson, and T. Robishaw. The Magnetic Field of the Irregular Galaxy NGC 4214. *ApJ*, 736:139, August 2011. doi: 10.1088/0004-637X/736/2/139. 62

H. A. Kobulnicky and E. D. Skillman. Elemental Abundance Variations and Chemical Enrichment from Massive Stars in Starbursts. I. NGC 4214. *ApJ*, 471:211, November 1996. doi: 10.1086/177964. 16, 17, 62, 76

A. Laor and B. T. Draine. Spectroscopic constraints on the properties of dust in active galactic nuclei. *ApJ*, 402:441–468, January 1993. doi: 10.1086/172149. 52

J. C. Lee, R. C. Kennicutt, Jr., S. J. J. G. Funes, S. Sakai, and S. Akiyama. Dwarf Galaxy Starburst Statistics in the Local Volume. *ApJ*, 692:1305, February 2009. doi: 10.1088/0004-637X/692/2/1305. 58

C. Leitherer, H. C. Ferguson, T. M. Heckman, and J. D. Lowenthal. The Lyman Continuum in Starburst Galaxies Observed with the Hopkins Ultraviolet Telescope. *ApJ*, 454:L19, November 1995. doi: 10.1086/309760. 97

C. Leitherer, W. D. Vacca, P. S. Conti, A. V. Filippenko, C. Robert, and W. L. W. Sargent. Hubble Space Telescope Ultraviolet Imaging and Spectroscopy of the Bright Starburst in the Wolf-Rayet Galaxy NGC 4214. *ApJ*, 465:717, July 1996. doi: 10.1086/177456. 76

J. Lequeux. *The Interstellar Medium*. 2005. doi: 10.1007/b137959. 2

J. Lequeux, M. Peimbert, J. F. Rayo, A. Serrano, and S. Torres-Peimbert. Chemical composition and evolution of irregular and blue compact galaxies. *A&A*, 80:155–166, December 1979. 16, 18, 76

A. K. Leroy, A. Bolatto, K. Gordon, K. Sandstrom, P. Gratier, E. Rosolowsky, C. W. Engelbracht, N. Mizuno, E. Corbelli, Y. Fukui, and A. Kawamura. The CO-to-H_2 Conversion Factor from Infrared Dust Emission across the Local Group. *ApJ*, 737:12, August 2011. doi: 10.1088/0004-637X/737/1/12. 88

A. Li and B. T. Draine. Infrared Emission from Interstellar Dust. II. The Diffuse Interstellar Medium. *ApJ*, 554:778–802, June 2001. doi: 10.1086/323147. 8, 52

C. F. Lillie and A. N. Witt. Ultraviolet photometry from the orbiting astronomical observatory. XXV - Diffuse galactic light in the 1500-4200 A region and the scattering properties of interstellar dust grains. *ApJ*, 208:64–74, August 1976. doi: 10.1086/154582. 8, 9

R. R. Lindner, A. J. Baker, A. Omont, A. Beelen, F. N. Owen, F. Bertoldi, H. Dole, N. Fiolet, A. I. Harris, R. J. Ivison, C. J. Lonsdale, D. Lutz, and M. Polletta. A Deep 1.2 mm Map of the Lockman Hole North Field. *ApJ*, 737:83, August 2011. doi: 10.1088/0004-637X/737/2/83. 60

U. Lisenfeld, F. P. Israel, J. M. Stil, and A. Sievers. (Sub)millimetre emission from ¡ASTROBJ¿NGC 1569¡/ASTROBJ¿: An abundance of very small grains. *A&A*, 382:860–871, February 2002. doi: 10.1051/0004-6361:20011782. 15

J. W. MacKenty, J. Maíz-Apellániz, C. E. Pickens, C. A. Norman, and N. R. Walborn. Hubble Space Telescope/WFPC2 and VLA Observations of the Ionized Gas in the Dwarf Starburst Galaxy NGC 4214. *AJ*, 120:3007–3026, December 2000. doi: 10.1086/316841. 16, 17, 61, 62, 76

J. M. MacLachlan, L. D. Matthews, K. Wood, and J. S. Gallagher. The Stability of Low Surface Brightness Disks Based on Multi-wavelength Modeling. *ApJ*, 741:6, November 2011. doi: 10.1088/0004-637X/741/1/6. 47

J. Maíz-Apellániz. Bidimensional Spectroscopy of Nearby Starbursts. *PASP*, 112:1138–1139, August 2000. doi: 10.1086/316607. 61

J. Maíz-Apellániz. CHORIZOS: A χ^2 Code for Parameterized Modeling and Characterization of Photometry and Spectrophotometry. *PASP*, 116:859–875, September 2004. doi: 10.1086/424021. 30

J. Maíz-Apellániz, J. M. Mas-Hesse, C. Munoz-Tunon, J. M. Vilchez, and H. O. Castaneda. Bidimensional spectroscopy of NGC 4214: evolutionary state and interstellar extinction. *A&A*, 329:409–430, January 1998. 16, 76

J. Maíz-Apellániz, C. Muñoz-Tuñón, G. Tenorio-Tagle, and J. M. Mas-Hesse. Kinematical analysis of the ionized gas in the nuclear region of NGC 4214. *A&A*, 343:64–80, March 1999. 98

J. Maíz-Apellániz, L. Cieza, and J. W. MacKenty. Tip of the Red Giant Branch Distances to NGC 4214, UGC 685, and UGC 5456. *AJ*, 123:1307–1315, March 2002. doi: 10.1086/338853. 16

C. L. Martin. The Impact of Star Formation on the Interstellar Medium. I. The Excitation of Diffuse, Warm Ionized Gas in Dwarf Galaxies. *ApJ*, 491:561, December 1997. doi: 10.1086/304978. 16, 18, 76

C. L. Martin. The Impact of Star Formation on the Interstellar Medium in Dwarf Galaxies. II. The Formation of Galactic Winds. *ApJ*, 506:222–252, October 1998. doi: 10.1086/306219. 97

J. S. Mathis. Nebular dust and extinction in ionized nebulae. I - The Balmer decrement. *ApJ*, 267:119–125, April 1983. doi: 10.1086/160849. 8, 9

V. J. McIntyre. Neutral and ionised hydrogen in NGC 4214. *PASA*, 15:157–58, April 1998. 16

J. P. M. Melisse and F. P. Israel. Global properties of dwarf galaxies II. Colours and luminosities. *A&A*, 285:51–68, May 1994. 15

C. Meny, V. Gromov, N. Boudet, J.-P. Bernard, D. Paradis, and C. Nayral. Far-infrared to millimeter astrophysical dust emission. I. A model based on physical properties of amorphous solids. *A&A*, 468:171–188, June 2007. doi: 10.1051/0004-6361:20065771. 15

A. Misiriotis, C. C. Popescu, R. Tuffs, and N. D. Kylafis. Modeling the spectral energy distribution of galaxies. II. Disk opacity and star formation in 5 edge-on spirals. *A&A*, 372:775–783, June 2001. doi: 10.1051/0004-6361:20010568. 47

D. H. Morgan, K. Nandy, and G. I. Thompson. The ultraviolet galactic background from TD-I satellite observations. *MNRAS*, 177:531–544, December 1976. 8, 9

G. Natale, R. J. Tuffs, C. K. Xu, C. C. Popescu, J. Fischera, U. Lisenfeld, N. Lu, P. Appleton, M. Dopita, P.-A. Duc, Y. Gao, W. Reach, J. Sulentic, and M. Yun. Dust Emission and Star Formation in Stephan's Quintet. *ApJ*, 725:955–984, December 2010. doi: 10.1088/0004-637X/725/1/955. 47

M. S. Oey, G. R. Meurer, S. Yelda, E. J. Furst, S. M. Caballero-Nieves, D. J. Hanish, E. M. Levesque, D. A. Thilker, G. L. Walth, J. Bland-Hawthorn, M. A. Dopita, H. C. Ferguson, T. M. Heckman, M. T. Doyle, M. J. Drinkwater, K. C. Freeman, R. C. Kennicutt, Jr., V. A. Kilborn, P. M. Knezek, B. Koribalski, M. Meyer, M. E. Putman, E. V. Ryan-Weber, R. C. Smith, L. Staveley-Smith, R. L. Webster, J. Werk, and M. A. Zwaan. The Survey for Ionization in Neutral Gas Galaxies. III. Diffuse, Warm Ionized Medium and Escape of Ionizing Radiation. *ApJ*, 661:801–814, June 2007. doi: 10.1086/517867. 97

D. E. Osterbrock. Book-Review - Astrophysics of Gaseous Nebulae and Active Galactic Nuclei. *S&T*, 78:491, November 1989. 5

Planck Collaboration. Planck Early Release Compact Source Catalogue (Planck, 2011). *VizieR Online Data Catalog*, 8088:0, 2011. 72

Planck Collaboration, P. A. R. Ade, N. Aghanim, M. Arnaud, M. Ashdown, J. Aumont,

C. Baccigalupi, A. Balbi, A. J. Banday, R. B. Barreiro, J. G. Bartlett, E. Battaner, K. Benabed, A. Benoît, J.-P. Bernard, M. Bersanelli, R. Bhatia, J. J. Bock, A. Bonaldi, J. R. Bond, J. Borrill, C. Bot, F. R. Bouchet, F. Boulanger, M. Bucher, C. Burigana, P. Cabella, J.-F. Cardoso, A. Catalano, L. Cayón, A. Challinor, A. Chamballu, L.-Y. Chiang, C. Chiang, P. R. Christensen, D. L. Clements, S. Colombi, F. Couchot, A. Coulais, B. P. Crill, F. Cuttaia, L. Danese, R. D. Davies, R. J. Davis, P. de Bernardis, G. de Gasperis, A. de Rosa, G. de Zotti, J. Delabrouille, J.-M. Delouis, F.-X. Désert, C. Dickinson, K. Dobashi, S. Donzelli, O. Doré, U. Dörl, M. Douspis, X. Dupac, G. Efstathiou, T. A. Enßlin, F. Finelli, O. Forni, M. Frailis, E. Franceschi, Y. Fukui, S. Galeotta, K. Ganga, M. Giard, G. Giardino, Y. Giraud-Héraud, J. González-Nuevo, K. M. Górski, S. Gratton, A. Gregorio, A. Gruppuso, D. Harrison, G. Helou, S. Henrot-Versillé, D. Herranz, S. R. Hildebrandt, E. Hivon, M. Hobson, W. A. Holmes, W. Hovest, R. J. Hoyland, K. M. Huffenberger, A. H. Jaffe, W. C. Jones, M. Juvela, A. Kawamura, E. Keihänen, R. Keskitalo, T. S. Kisner, R. Kneissl, L. Knox, H. Kurki-Suonio, G. Lagache, A. Lähteenmäki, J.-M. Lamarre, A. Lasenby, R. J. Laureijs, C. R. Lawrence, S. Leach, R. Leonardi, C. Leroy, M. Linden-Vørnle, M. López-Caniego, P. M. Lubin, J. F. Macías-Pérez, C. J. MacTavish, S. Madden, B. Maffei, N. Mandolesi, R. Mann, M. Maris, E. Martínez-González, S. Masi, S. Matarrese, F. Matthai, P. Mazzotta, P. R. Meinhold, A. Melchiorri, L. Mendes, A. Mennella, M.-A. Miville-Deschênes, A. Moneti, L. Montier, G. Morgante, D. Mortlock, D. Munshi, A. Murphy, P. Naselsky, F. Nati, P. Natoli, C. B. Netterfield, H. U. Nørgaard-Nielsen, F. Noviello, D. Novikov, I. Novikov, T. Onishi, S. Osborne, F. Pajot, R. Paladini, D. Paradis, F. Pasian, G. Patanchon, O. Perdereau, L. Perotto, F. Perrotta, F. Piacentini, M. Piat, S. Plaszczynski, E. Pointecouteau, G. Polenta, N. Ponthieu, T. Poutanen, G. Prézeau, S. Prunet, J.-L. Puget, W. T. Reach, R. Rebolo, M. Reinecke, C. Renault, S. Ricciardi, T. Riller, I. Ristorcelli, G. Rocha, C. Rosset, M. Rowan-Robinson, J. A. Rubiño-Martín, B. Rusholme, M. Sandri, G. Savini, D. Scott, M. D. Seiffert, G. F. Smoot, J.-L. Starck, F. Stivoli, V. Stolyarov, R. Sudiwala, J.-F. Sygnet, J. A. Tauber, L. Terenzi, L. Toffolatti, M. Tomasi, J.-P. Torre, M. Tristram, J. Tuovinen, G. Umana, L. Valenziano, J. Varis, P. Vielva, F. Villa, N. Vittorio, L. A. Wade, B. D. Wandelt, A. Wilkinson, N. Ysard, D. Yvon, A. Zacchei, and A. Zonca. Planck early results. XVII. Origin of the submillimetre excess dust emission in the Magellanic Clouds. *A&A*, 536:A17, December 2011a. doi: 10.1051/0004-6361/201116473. 15, 106, 107

Planck Collaboration, P. A. R. Ade, N. Aghanim, M. Arnaud, M. Ashdown, J. Aumont, C. Baccigalupi, A. Balbi, A. J. Banday, R. B. Barreiro, and et al. Planck early results. VII. The Early Release Compact Source Catalogue. *A&A*, 536:A7, December 2011b. doi: 10.1051/0004-6361/201116474. 60

C. C. Popescu, A. Misiriotis, N. D. Kylafis, R. J. Tuffs, and J. Fischera. Modelling the spectral energy distribution of galaxies. I. Radiation fields and grain heating in the edge-on spiral NGC 891. *A&A*, 362:138–150, October 2000. 47

C. C. Popescu, R. J. Tuffs, H. J. Völk, D. Pierini, and B. F. Madore. Cold Dust in Late-Type Virgo Cluster Galaxies. *ApJ*, 567:221–236, March 2002. doi: 10.1086/338383. 15, 99

C. C. Popescu, R. J. Tuffs, N. D. Kylafis, and B. F. Madore. Far Infrared mapping of NGC 891. *A&A*, 414:45–52, January 2004. doi: 10.1051/0004-6361:20031581. 47

C. C. Popescu, R. J. Tuffs, M. A. Dopita, J. Fischera, N. D. Kylafis, and B. F. Madore. Modelling the spectral energy distribution of galaxies. V. The dust and PAH emission SEDs of disk galaxies. *A&A*, 527:A109, March 2011. doi: 10.1051/0004-6361/201015217. iii, vii, 47, 48, 49, 50, 51, 52, 71, 79, 80, 84, 85, 86, 87, 88, 91, 93, 94, 96, 98, 99, 101, 110

W. T. Reach, E. Dwek, D. J. Fixsen, T. Hewagama, J. C. Mather, R. A. Shafer, A. J. Banday, C. L. Bennett, E. S. Cheng, R. E. Eplee, Jr., D. Leisawitz, P. M. Lubin, S. M. Read, L. P. Rosen, F. G. D. Shuman, G. F. Smoot, T. J. Sodroski, and E. L. Wright. Far-Infrared Spectral Observations of the Galaxy by COBE. *ApJ*, 451:188, September 1995. doi: 10.1086/176210. 15

W. T. Reach, S. T. Megeath, M. Cohen, J. Hora, S. Carey, J. Surace, S. P. Willner, P. Barmby, G. Wilson, W. Glaccum, P. Lowrance, M. Marengo, and G. G. Fazio. Absolute Calibration of the Infrared Array Camera on the Spitzer Space Telescope. *PASP*, 117:978–990, September 2005. doi: 10.1086/432670. 59

A. E. Reines, K. E. Johnson, and W. M. Goss. Emerging Massive Star Clusters Revealed: High-Resolution Imaging of NGC 4449 from the Radio to the Ultraviolet. *AJ*, 135:2222–2239, June 2008. doi: 10.1088/0004-6256/135/6/2222. 18, 76, 78, 89

G. H. Rieke, E. T. Young, C. W. Engelbracht, D. M. Kelly, F. J. Low, E. E. Haller, J. W. Beeman, K. D. Gordon, J. A. Stansberry, K. A. Misselt, J. Cadien, J. E. Morrison, G. Rivlis, W. B. Latter, A. Noriega-Crespo, D. L. Padgett, K. R. Stapelfeldt, D. C. Hines, E. Egami, J. Muzerolle, A. Alonso-Herrero, M. Blaylock, H. Dole, J. L. Hinz, E. Le Floc'h, C. Papovich, P. G. Pérez-González, P. S. Smith, K. Y. L. Su, L. Bennett, D. T. Frayer, D. Henderson, N. Lu, F. Masci, M. Pesenson, L. Rebull, J. Rho, J. Keene, S. Stolovy, S. Wachter, W. Wheaton, M. W. Werner, and P. L. Richards. The Multiband Imaging Photometer for Spitzer (MIPS). *ApJS*, 154:25–29, September 2004. doi: 10.1086/422717. 59

H. Roussel. Scanamorphos: a map-making software for Herschel and similar scanning bolometer arrays. *ArXiv e-prints*, May 2012. 60

K. M. Sandstrom, A. D. Bolatto, B. T. Draine, C. Bot, and S. Stanimirović. The Spitzer Survey of the Small Magellanic Cloud (S^3MC): Insights into the Life Cycle of Polycyclic

Aromatic Hydrocarbons. *ApJ*, 715:701–723, June 2010. doi: 10.1088/0004-637X/715/2/701. 96

E. F. Schlafly and D. P. Finkbeiner. Measuring Reddening with Sloan Digital Sky Survey Stellar Spectra and Recalibrating SFD. *ApJ*, 737:103, August 2011. doi: 10.1088/0004-637X/737/2/103. 25

D. J. Schlegel, D. P. Finkbeiner, and M. Davis. Maps of Dust Infrared Emission for Use in Estimation of Reddening and Cosmic Microwave Background Radiation Foregrounds. *ApJ*, 500:525, June 1998. doi: 10.1086/305772. 25

A. Schruba, A. K. Leroy, F. Walter, F. Bigiel, E. Brinks, W. J. G. de Blok, C. Kramer, E. Rosolowsky, K. Sandstrom, K. Schuster, A. Usero, A. Weiss, and H. Wiesemeyer. Low CO Luminosities in Dwarf Galaxies. *AJ*, 143:138, June 2012. doi: 10.1088/0004-6256/143/6/138. 16

B. Siana, H. I. Teplitz, J. Colbert, H. C. Ferguson, M. Dickinson, T. M. Brown, C. J. Conselice, D. F. de Mello, J. P. Gardner, M. Giavalisco, and F. Menanteau. New Constraints on the Lyman Continuum Escape Fraction at z˜1.3. *ApJ*, 668:62–73, October 2007. doi: 10.1086/521185. 97

R. Siebenmorgen and E. Krügel. Dust in starburst nuclei and ULIRGs. SED models for observers. *A&A*, 461:445–453, January 2007. doi: 10.1051/0004-6361:20065700. 47

L. Silva, G. L. Granato, A. Bressan, and L. Danese. Modeling the Effects of Dust on Galactic Spectral Energy Distributions from the Ultraviolet to the Millimeter Band. *ApJ*, 509:103–117, December 1998. doi: 10.1086/306476. 47

B. M. Swinyard, P. Ade, J.-P. Baluteau, H. Aussel, M. J. Barlow, G. J. Bendo, D. Benielli, J. Bock, D. Brisbin, A. Conley, L. Conversi, A. Dowell, D. Dowell, M. Ferlet, T. Fulton, J. Glenn, A. Glauser, D. Griffin, M. Griffin, S. Guest, P. Imhof, K. Isaak, S. Jones, K. King, S. Leeks, L. Levenson, T. L. Lim, N. Lu, G. Makiwa, D. Naylor, H. Nguyen, S. Oliver, P. Panuzzo, A. Papageorgiou, C. Pearson, M. Pohlen, E. Polehampton, D. Pouliquen, D. Rigopoulou, S. Ronayette, H. Roussel, A. Rykala, G. Savini, B. Schulz, A. Schwartz, D. Shupe, B. Sibthorpe, S. Sidher, A. J. Smith, L. Spencer, M. Trichas, H. Triou, I. Valtchanov, R. Wesson, A. Woodcraft, C. K. Xu, M. Zemcov, and L. Zhang. In-flight calibration of the Herschel-SPIRE instrument. *A&A*, 518:L4, July 2010. doi: 10.1051/0004-6361/201014605. 59

D. L. Talent. A Spectrophotometric Study of H II Regions in Chemically Young Galaxies. In *Bulletin of the American Astronomical Society*, volume 12 of *Bulletin of the American Astronomical Society*, page 866, September 1980. 16, 18, 76

C. Theis and S. Kohle. Multi-method-modeling of interacting galaxies. I. A unique scenario for NGC 4449? *A&A*, 370:365–383, May 2001. doi: 10.1051/0004-6361:20010198. 18

H. A. Thronson, Jr., D. A. Hunter, C. M. Telesco, D. A. Harper, and R. Decher. Star formation in the Magellanic irregular galaxy NGC 4449. *ApJ*, 317:180–189, June 1987. doi: 10.1086/165266. 18

R. J. Tuffs, C. C. Popescu, H. J. Völk, N. D. Kylafis, and M. A. Dopita. Modelling the spectral energy distribution of galaxies. III. Attenuation of stellar light in spiral galaxies. *A&A*, 419:821–835, June 2004. doi: 10.1051/0004-6361:20035689. 87

L. Úbeda, J. Maíz-Apellániz, and J. W. MacKenty. The Young Stellar Population of NGC 4214 as Observed with the Hubble Space Telescope. II. Results. *AJ*, 133:932–951, March 2007. doi: 10.1086/509503. ii, vi, 17, 30, 76, 78, 79

F. Walter and E. Brinks. Holes and Shells in the Interstellar Medium of the Nearby Dwarf Galaxy IC 2574. *AJ*, 118:273–301, July 1999. doi: 10.1086/300906. 16

F. Walter, C. L. Taylor, S. Hüttemeister, N. Scoville, and V. McIntyre. The Interaction between the Interstellar Medium and Star Formation in the Dwarf Starburst Galaxy NGC 4214. *AJ*, 121:727–739, February 2001. doi: 10.1086/318775. 16, 72, 88

F. Walter, E. Brinks, W. J. G. de Blok, F. Bigiel, R. C. Kennicutt, Jr., M. D. Thornley, and A. Leroy. THINGS: The H I Nearby Galaxy Survey. *AJ*, 136:2563, December 2008. doi: 10.1088/0004-6256/136/6/2563. 16, 78, 79, 87, 88, 94

J. C. Weingartner and B. T. Draine. Dust Grain-Size Distributions and Extinction in the Milky Way, Large Magellanic Cloud, and Small Magellanic Cloud. *ApJ*, 548:296–309, February 2001. doi: 10.1086/318651. 48, 52, 101

B. F. Williams, J. J. Dalcanton, K. M. Gilbert, A. C. Seth, D. R. Weisz, E. D. Skillman, and A. E. Dolphin. The ACS Nearby Galaxy Survey Treasury. VII. The NGC 4214 Starburst and the Effects of Star Formation History on Dwarf Morphology. *ApJ*, 735:22, July 2011. doi: 10.1088/0004-637X/735/1/22. 16

J. H. Wise and R. Cen. Ionizing Photon Escape Fractions From High-Redshift Dwarf Galaxies. *ApJ*, 693:984–999, March 2009. doi: 10.1088/0004-637X/693/1/984. 97

E. M. Xilouris, Y. I. Byun, N. D. Kylafis, E. V. Paleologou, and J. Papamastorakis. Are spiral galaxies optically thin or thick? *A&A*, 344:868–878, April 1999. 50, 98

J. Zastrow, M. S. Oey, S. Veilleux, M. McDonald, and C. L. Martin. An Ionization Cone in the Dwarf Starburst Galaxy NGC 5253. *ApJ*, 741:L17, November 2011. doi: 10.1088/2041-8205/741/1/L17. 97, 98